Scalable fabrication of bio-inspired, 3D micro/nanofluidic devices

Submitted in partial fulfillment of the requirements
of the degree of Doctor of Philosophy from Indian Institute of Technology, Bombay, India and Monash University, Australia

by

Prasoon Kumar

Supervisors:
Prof. Prasanna S. Gandhi (IIT Bombay)
Prof. Mainak Majumder (Monash University)

The course of study for this award was developed jointly by Monash University, Australia and the Indian Institute of Technology, Bombay and was given academic recognition by each of them. The program was administrated by The IITB-Monash Research Academy

(2018)

Approval Sheet

The thesis entitled "*Scalable fabrication of bio-inspired 3D micro/nanofluidic devices*" by *Prasoon Kumar* is approved for the degree of **Doctor of Philosophy**

Date: 2-04-2018
Place: IIT Bombay, Powai

Declaration

I declare that this written submission represents my ideas in my own words and where others ideas or words have been included; I have adequately cited and referenced the original sources. I also declare that I have adhered to all principles of academic honesty and integrity and have not misrepresented or fabricated or falsified any idea/data/fact/source in my submission. I understand that any violation of the above will be cause for disciplinary action by the Institute and can also evoke penal action from the sources which have thus not been properly cited or from whom proper permission has not been taken when needed.

Notice 1

Under the Copyright Act 1968, this thesis must be used only under the normal conditions of scholarly fair dealing. In particular no results or conclusions should be extracted from it, nor should it be copied or closely paraphrased in whole or in part without the written consent of the author. Proper written acknowledgement should be made for any assistance obtained from this thesis.

Notice 2

I certify that I have made all reasonable efforts to secure copyright permissions for third party content included in this thesis and have not knowingly added copyright content to my work without the owner's permission.

Prasoon Kumar

[redacted]

[redacted]

Date: 2nd April, 2018

Indian Institute of Technology-Bombay, India
Certificate of Course Work

This is to certify that Mr. Prasoon Kumar [redacted] was admitted to the candidacy of the Ph. D. Degree on 14/7/2011, after successfully completing all the courses required for the Ph. D. program. The details of the course work done are given below.

Sl.No	Course No.	Course name	Credits
1	CL601	Advanced Transport Phenomena	6
2	MM 453	Engineering polymers and composites of materials	6
3	MES 801	Seminar	4
3	HS 699	Communication and Presentation Skills	N
4	ME 645	MEMS-Design, Fabrication and Characterization	Audit
5	CH 807	Organic Synthesis	Audit

I.I.T. Bombay Dy. Registrar (Academic)
Dated: 2nd April, 2018

ACKNOWLEDGMENTS

It would not have been possible to finish this thesis successfully without the help and continuous guidance of many individuals. So, I would like to express my deep gratitude towards them.

First and foremost, I would like to express my deep and sincere gratitude to my advisors: Prof. Prasanna S Gandhi, Department of Mechanical Engineering, IIT Bombay and Ass/Prof. Mainak Majumder, Department of Mechanical and Aerospace Engineering, Monash University, Melbourne, Australia. They allowed me to work on a problem which dwelt at an interface of materials science and mechanical and chemical engineering. The project involved experimental and computational skills and knowledge which were challenging as well as exciting enough to keep me get going during my difficult period. Although the arena of the project was quite different from my previous background, my supervisors filled me with enthusiasm and belief that I could accomplish it. Their enthusiastic and integral views on research and commitment towards research with distant vision have made a deep impression on me. I owe them credit for allowing me to work and think independently, and also supporting me in tough times when I needed the most.

I wish to express my warm thanks and sincere gratitude to the former CEO of IITB-Monash Research Academy, Prof. Mohan Krishnamoorthy for an initial grant for the purchase of electrospinning unit, a key facility for my project. I would also like to thank the present CEO, Prof. Murli Sastry for his consistent support, encouragement and mentorship during the last phase of my Ph.D. tenure. I extend my gratitude towards Prof. Adrian Neild and Prof. Rohit Srivastava for their input and suggestions in the project. I would like to thank the non-teaching staffs of IITB-Monash Research Academy for extending their support and advice during my entire period of candidature. Further, I would like to extend my sincere regards to Center for Excellence in Nanoelectronics (CEN), Sophisticated Analytical Instrumentation Facility (SAIF) and Department of Metallurgical Engineering and Material Science (MEMS), IIT Bombay, for helping with analytical and imaging facilities for my thesis. I express my sincere thanks to IITB-Monash Research Academy for providing adequate financial support during my tenure of Ph.D.

I would like to acknowledge all current and past lab members from Suman Mashruwala Advance Microengineering lab; Dr. Kiran Bhole, Rupesh Bopade, Deepak karnath, Dr. Prashant, Tanveer, Vishal, Abhijeet, Sheetal, Naresh, Nihal, Ajit, Sunil, Bhargav and others for sharing those precious moments with me and allowing me to be part of theirs. Along with these people, I would also like to acknowledge lab members from Nano-Scale Engineering Lab; Dr. Phillip Sheath, Dr. Derrek Lobo, Dr. Dhanraj Shinde, Dr. Parama Banerjee-Chakraborty, Samuel Martin, Tanesh Gamot, Abozar Akbari, Mahdokht E. Shaibani for being on my side for any help and support.

Besides this, I would like separately express my sincere thanks and regards to some of the people without whom the journey through throughout my tenure would have been much tougher. These people are Prashant Agarwal, Tanveer-Ul-Islam, Prateek Jain, Sam Martin, Dr. Dhanraj Shinde who were always there with any help and support in labs throughout my Ph.D. tenure. I express my regards for my friends specially Kaushik, Dr. Atif, Varun, Dr. Rajesh, Shirisha, Amit, Girish and others for sharing their precious moment while discussing life, nature, philosophy and country. Their support and help during ups and downs during this period is highly appreciated.

I would like to thank my family, in-laws and my friends for being the main source of my emotional strength and helping me when I needed them the most. I would always be indebted to them for everything they have done for me and for supporting me to become what I am today. I would like to thank Late Dr. Anupam Pal who was very pivotal in shaping my scientific career so far and been a source of inspiration as a scientist and great teacher. Finally, I would like to thank almighty for all his blessings showered upon me.

Warm thanks and regards,

Prasoon Kumar

Dedicated to

Parents : Mrs Bimla(Maa) and Mr Surya Nath Pandey (Papa),

Mrs. Shilpa (Wife) and Miss Avneesha (Daughter)

& My Brothers: Mr Ashish and Rishav

This humble work is a sign of my love for you

ABSTRACT

The diffusion of small molecules through polymeric micro/nanosystems finds application in numerous fields such as tissue engineering, biomedical devices, membrane-separation technologies, food-packaging industries and in the removal of contaminants, solvents and such others. The performance of such devices depends on the microstructure of the polymers and the design of the micro/nanosystems that employ the polymers. The design of devices at multiple length scales that are inspired from natural systems has been proven in the manufacture of highly efficient microsystems. However, the scalable fabrication of such micro/nanosystems (with limited costs in instrumentation and operation, and minimal requirement of expertise and time) should be possible before these micro/nanosystems can be used at full throttle in the applications mentioned above.

Therefore, in the current work, we have thoroughly studied the secondary lamella of fish gills at different length scales by using computational and theoretical analysis, in order to determine the structural parameters that are responsible for their excellent gas-/solute-exchange capabilities. Our findings suggested the evolutionary conservation of a few structural factors and parametric ratios in fish gills, which is responsible for the efficient gas/solute exchange capability in every fish. Inspired by the design of secondary lamella, we have fabricated bio- inspired multiscale 3D micro/nanochannel networks in thin polymeric matrices by solvent etching of sacrificial structures that are formed by a combination of two scalable microtechnologies: electrospinning and the controlled, lifted Hele-Shaw method. The fabrication methodology presented here is a lithographyless, ultrafast, scalable process for the generating of multiscale fractal morphologies in polymeric materials. After conducting structural and dye flow characterization of the above mentioned multiscale, 3D micro/nanofluidic devices, preliminary results of their mass-transfer capabilities showed that these multiscale, 3D micro/nanofluidic devices were better in comparison to simple 3D micro/nanofluidic devices. Further, our experimental and theoretical investigation suggested that the geometry of the intermediate channel network (reservoir) plays a vital role in interfacing with a random network of nanochannels for enhanced volumetric fluid flow through them. Further, the densities and the tortuosity of the nanochannel networks also play

a vital role in the volumetric fluid flow and mass-transfer capabilities of 3D micro/nanofluidic devices.

Although capillary-driven flow studies were carried out by using the 3D micro/nanofluidic devices that are mentioned above, a passive fluid pump connected to such 3D micro/nanofluidic devices is desirable in order to achieve a better rate of fluid flow. This may result in extending the applications of 3D micro/nanofluidic devices in areas such as µ-TAS, cooling of microelectronic circuits and advance drug delivery. Therefore, we have developed a passive micropump that was inspired by leaves of plants that can pump fluid at a rate comparable with that which is reported in previous literature. In this study, the manufacturing of micropumps also represents a simple, scalable and inexpensive process in which spin-coating technology is integrated with a controlled, lifted Hele-Shaw cell. The micropumps were able to emulate the structural features of leaves and the pump fluid by a coupled phenomenon of capillary action, absorption and evaporation. Further, a theoretical model was developed to describe the micropumping phenomenon. The model elucidates the role of different structural and ambient factors such as designs that are inspired from leaves, the temperature of the ambience, the density of the vascular network, the permeability of a porous substrate and such others for volumetric pumping of fluid and sustaining of the pressure head. The results predicted by the theoretical model corroborated well with the experimental findings. Eventually, the design, fabrication and characterization of the leaf-inspired micropump were successfully carried out.

In summary, in order to exploit bio-inspired micro/nanofluidic devices for mass-transfer operations, the work focused on the design and fabrication of these devices through scalable micro/nanotechnologies; this was done in order to ensure enhanced fluid flow and to study factors that affect the flow of fluid through such devices. Thus, the work will enable the development of 3D micro/nanofluidic at a large scale for applications in biomedical and chemical industry, which demand the transfer of heat and mass.

Table of Contents

Table of Figures

List of Tables

1. Chapter 1 Introduction

1.1. Introduction

The separation of volatile organic compounds (VOC), gases, solutes and organic solvents is one of the important unit operations that are routinely carried out in chemical industries. Processes such as distillation, evaporation, extraction, absorption and adsorption have been employed since decades to accomplish nearly all unit operations[1]. However, the advancements in membrane-based technologies for gas, liquid and solute separation have gradually replaced traditional processes in the number of unit operations. These membrane-based technologies offer the separation of gas, liquid and solute at a relatively low cost of capital investment and operations. Moreover, they require minimal energy usage, offer ease of operation and maintenance, and have potential for improvement through continual research and development. Therefore, since the past 30 years, membrane-based separation methods have dominated the majority of separation processes such as microfiltration, ultrafiltration, reverse osmosis, nanofiltration and electrodialysis, and are accepted throughout the industry with a high degree of confidence[2-4]. However, the scope of membranes has been rather limited in the addressing of the separation processes at a micro/nanoscale, even though the separation process in micro/nanoscale devices has diverse applications in various fields such as chemical/bioanalytical, as lab-on chips, organ-on-chip devices, tissue-engineered products, artificial organs, advanced drug delivery, separation and purification of chemicals, desalination, carbon dioxide sequestration and such others[5, 6]. This is primarily due to the limited understanding of fluid flow and mass-transfer operations at a reduced length scale and the inability to fabricate complex devices with a hierarchical structure that has a feature size that ranges from a millimetre to a nanometre. Further, the integration of micro/nanofluidic devices with functional polymeric membranes for different unit operations also exists as a manufacturing challenge[6]. Therefore, the design and development of multiscale micro/nanofluidic devices with integrated polymeric membranes cannot be realised unless the issues that are mentioned above have been resolved. In the absence of such devices, the complications that are associated with a class of current biomedical devices that deal with separation of chemical/biological species persist. The gravity of the problems can be understood better in the light of healthcare issues that affect the whole world. Therefore, in the forthcoming section, we have discussed two healthcare

problems that are rampant across the globe, and the challenges that are faced by chemical, mechanical and bioengineering scientists and engineers while solving the problem with multiscale micro/nanofluidic devices that have integrated polymeric membranes.

1.2. Motivation

A number of medical problems require the separation of chemical species from blood in order to detoxify the circulating blood. The membranes are commonly employed to achieve the separation of chemical species through devices known as extracorporeal membrane separators. However, the efficiency of the membrane is dependent on the design of the biomedical devices. Two popularly known biomedical devices that achieve detoxification of blood are extracorporeal membrane oxygenators and kidney dialysers. They are used to ameliorate medical conditions that are related to lungs and kidneys, respectively, through the use of hollow fibre membranes. However, problems such as non-portability, high priming volume, low permeation capacity of membranes, short service life, bulky oxygenation source, reduction in efficiency over time, leakage of plasma due to prolonged use, lack of patient compliance still persist[7, 8]. The magnitude of these problems can be gauged by the statistics identified by the World Health Organization (WHO), which reveals that lung diseases (Chronic Obstructive Pulmonary Disease (COPD) and lung cancers) claim about 4.5 million lives per year worldwide[9]. Moreover, the statistics also show that the annual health budget for COPD and lung cancer will see a rise of US$ 2.1 trillion to US$ 4.8 trillion, and US$ 51 billion to US$ 83 billion, respectively, from 2010 to 2030 across the globe. Out of this, half of the budget will be borne by developing countries[10]. Similarly, kidney diseases also have plagued the entire world, out of which about 27 million are in USA alone. In addition, the health budgets that are dedicated to chronic kidney disease have exceeded $48 billion per year across the globe[9]. A solution is either to put these patients on membrane oxygenators/dialyser or to ameliorate the problem by transplanting a functioning kidney or lungs. However, both of the solutions mentioned above have their own drawbacks: the former leads to a compromised lifestyle, threat to life due to device complications during operation, and, sometimes, issues with affordability and unavailability. The latter solution suffers from lack of adequate donors, which creates long wait lists. In the US alone, this leads to the deaths of 13 people every day due to chronic kidney diseases[11] and approx.

400 people every day[12] due to lung-related issues . Thus, there is a huge gap between current medical interventions and lung-/kidney-disease cases across the globe.

Therefore, microfluidic-based devices that have integrated membranes have been explored as artificial lung devices, and the lab-scale results are quite promising[13]. Lithography-based techniques have been used to generate fractal-shaped microchannel networks in polydimethylsiloxane (PDMS) matrices, the open end of which is closed by thin gas-permeating membranes in artificial lung oxygenators. Several researchers have attempted to manoeuvre the dimensions of channel networks, the pattern of the channel net, the thickness and the material of membranes and the assembly of devices in order to increase the oxygen-separating capabilities. Further, their devices demonstrated carbon dioxide and oxygen removal at a flux that is higher than human lungs[14-16]. Although the devices of the researchers performed well for a short period of time, there were problems of clotting, leakage due to mechanical assembly on prolonged use, biocompatibility issues and fabrication scalability, thus demonstrating enough scope for improvement in the design of oxygenators and in the solving of scale-up issues. Moreover, the devices used vascular channels that were fabricated by soft lithography, which inherently produce rectangular cross-sectioned channels in comparison to the circular cross-sectioned blood vessels that are found in living beings. This creates an issue of fluid-flow resistance in the microchannels. Moreover, a substantial part of single functional unit of above mentioned devices, which is the membrane that separates two microfluidic devices that have networks of channels, does not participate in gas diffusion due to limitations in the design. In addition, the fabrication method lacked scale-up technologies that would facilitate its being exploited at a commercial scale. Similarly, the devices that are based on hollow fibre membranes cannot be transplanted into the human body in order replace other functions of the kidney. Therefore, recently, microtechnologies that are related to silicon enabled the fabrication of nanoporous silicon-based dialysers[17]. They demonstrated the filtration of blood with a substantial removal of toxic elements such as urea, salts, toxic chemicals and such others. However, the problem of biocompatibility, short service life and high cost remain unaddressed queries. Moreover, the fabrication methodologies still remain unscalable and expensive. The current technologies are useful for lab-scale demonstration but are hardly suitable for the scaling up for commercial production of the devices[18]. Despite these efforts, PDMS-based membrane

oxygenators or silicon-based kidney dialysers are still unable to reach the stage of clinical trials.

The biomedical devices that are mentioned above, such as extracorporeal membrane oxygenators and kidney dialysers, need to mimic the functions of separation at the microscopic length scale, as is observed in natural systems. In a quest to achieve this objective, the design of the human lung and kidney was imitated in the designing of these devices. However, the process of manufacturing efficient micro/nanofluidic-based biomedical devices, which overcomes the limitations of the devices mentioned above, continues. Moreover, these solutions should not only improve a patient's life but should also percolate to the larger section of society that remains aloof from the continued improvement in the biomedical devices Since the underlying principle of dialysis and oxygenation is diffusion, the basic design, fabrication and characterization of micro/nanofluidic devices that serve the above functions would indeed be similar.

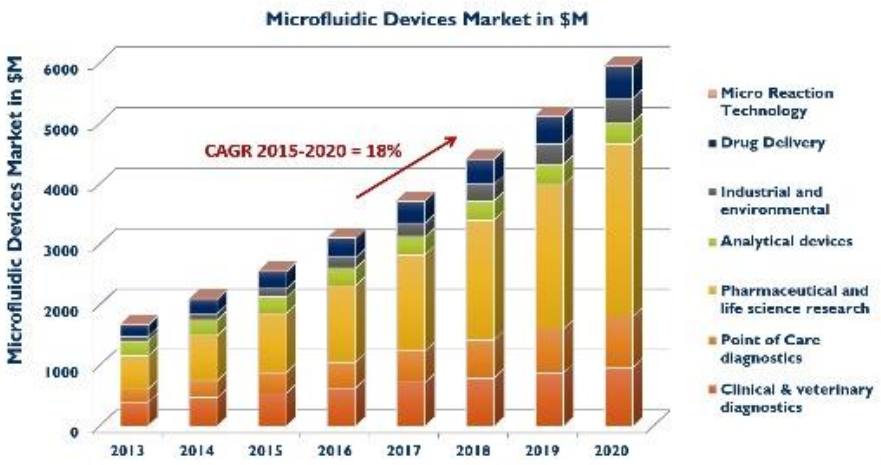

Figure 1.1 Graph, showing the growth of the microfluidic device market over years with respect to several application fields[19]

Further, multiscale, micro/nanofluidic devices that have reduced channel dimensions are also desirable in chemical analysis, biomolecule separation and diagnostics because it leads to a substantial increase in the surface area and a reduction in chemical volume. According to market research by Yole Development, it is estimated that the market for microfluidic devices is increasing at the compounded annual growth rate (CAGR) of 18 percent, with a current market size of $3500 million[19]. The percentage of microfluidic

devices in the healthcare sector occupies a sizeable portion of the total market share, as shown in Figure 1.1. Thus, the design and fabrication of 3D micro/nanofluidic devices by scalable microtechnologies will positively affect the growth of microfluidics in the healthcare sector. It will also accelerate the growth of lab-on-chip, organ-on-chip, artificial organs, tissue-engineered products and microdevices that are used in separation processes. Several of these devices include micro/nanofluidic devices that are integrated with different types of membranes.

1.3. Organization of thesis

Chapter 2 discusses the role of biomimetics and bio-inspiration in the development of micro/nanofluidic devices for the development of better fluid and mass transport properties. Further, the structure and function of fish gills and leaves of plants have been detailed as potential sources of biomimicry in the developing of advanced 3D micro/nanofluidic devices. Then, a discussion about the conventional and recent micro/nanofabrication technologies is presented along with their merits and demerits in generating bio-inspired, 3D micro/nanofluidic devices. Further, a short description about polymeric membranes, with special detailing about PDMS membranes and their integration with micro/nanofluidic devices is given. Thereafter, an overview of the convection-diffusion phenomena and capillary flow in micro/nanofluidic systems is presented. In addition, from the literature survey, challenges that are associated with the manufacturing of bio-inspired, multiscale, 3D channel network are discussed, culminating in the defining of the problem and building of the hypothesis. Eventually, the chapter ends with the layout of the research aims and the objectives of the thesis.

Chapter 3 investigates a few parametric ratios and morphological features of fish gills, which accounts for their enhanced gas-/solute-exchange capabilities. The investigation is carried out by the analysis of morphometric data of fish, which is available in literature. Thereafter, a 2D modelling and simulation of the convection-diffusion phenomenon through a secondary lamella model is discussed, and the role of parametric ratios has been illustrated. Further, a comparative analysis of theoretical and computational results, which suggest the evolutionary conservation of parametric ratios in fish, is presented. Further, investigation through 2D

modelling and simulation; the role of the thickness of the epithelial barrier and channel density in secondary lamella; and the magnitude and the direction of fluid flow on gas/solute exchange has been discussed.

Chapter 4 deals with the fabrication, structural characterization, and fluid and mass transport through vascularised polymer matrix-based 3D micro/nanofluidic devices. The chapter begins with the theoretical analysis on the geometry of reservoirs that interface with a random network of channels in micro/nanofluidic devices. Thereafter, the design and fabrication of vascularised PDMS matrices through electrospinning and the solvent etching of sacrificial structures (SESS) is presented. In addition, structural characterisation and connectivity of channels is reported through SEM and dye flow experiments, respectively. Further, the role of the geometry of the reservoir that interfaces with the channel network, the density and the tortuosity of the channel network that affects the fluid flow and mass-transfer through experimental methods have been discussed and, eventually, compared with theoretical findings.

Chapter 5 presents the design and fabrication of nature-inspired, 3D, multiscale, vascularised PDMS systems through integration of electrospinning and SESS (discussed in chapter 4) with controlled Saffman–Taylor instability in viscous polymers. Further, the chapter details the morphological characterization of the pattern of vascularisation; connectivity among multiscale channel networks through dye flow experiments; and mass transport behaviour of thin, nature-inspired, multiscale, vascularised PDMS matrices.

Chapter 6 deals with the design and fabrication of leaf-inspired micropump (LIM) by combining processes such as spin coating, micromoulding and controlled Saffman–Taylor instability in Hele-Shaw cells (discussed in chapter 5). Thereafter, the structural characterisation of LIM through imaging and their application as passive micropumps is reported. Further, a theoretical model has been developed to understand the role of the ambient and structural parameters of a LIM in the fluid pumping capacity and in the sustenance of the pressure head before cavitation. Eventually, experimental investigation of the role played by some of the factors that are discussed above, in the pumping capacity of fluid by the LIM has been discussed and compared with the theoretical findings.

Chapter 7 concludes the findings that are related to the knowledge gained by studying fish gills, the manufacturing processes that are developed for design and fabrication of 3D micro/nanofluidic devices, and the development of two types of devices: 1) thin, nature-inspired, multiscale, vascularised polymer matrices for gas/solute separation and 2) LIM for passive pumping of fluid. The chapter presents a comparative analysis between lithography-based techniques and manufacturing process proposed here. The chapter also contains the future scope of biomimicry of fish gills, manufacturing processes and the application of the devices mentioned above.

2. Chapter 2 Literature Survey and Research Aims

2.1. Biomimetics and Bio-inspiration

Within nature, numerous solutions for the improvement of human life are available for a majority of engineering problems that one encounters every day. Nature has experimented and examined these solutions over a period of millions of years through continuous improvement and, subsequently, has arrived at one of the most efficient and accurate solutions for any problem. Hence, the mimicry of nature's design or its functioning methodology in solving engineering problems, which is akin to nature's solutions, is termed as Biomimetics[20]. In recent years, biomimetic approaches to solving engineering problems have increased exponentially, as is shown by the number of research publications (Figure 2.1). One of the earliest known phenomena that have attracted the attention of researchers for centuries in the field of bimimicry is the transport phenomenon in biological systems. The transport of fluid through a vascularised network has intrigued researchers since long due to the least-resistance flow pattern of fluid through such networks and the ability of the fluid to traverse long distances with minimal loss of energy. This knowledge of bifurcating vasculature and their role in blood flow and diffusion through microcapillaries can be a useful source of biomimicry to drive various innovations in the fields of microsystem engineering, tissue engineering, artificial organs and lab-on-chip devices, in which fluid flow and diffusion routinely occurs[21, 22]. Microsystems that handle fluid flow, heat and mass-transfer operations use bifurcating micro-nanochannel networks to increase their efficiency and productivity per unit volume, as reported by previous literatures[23-25]. Therefore, it is natural to borrow knowledge from natural systems in which the design of an organ system and its vasculature network results in enhanced volumetric flow, efficient gas/solute exchange and energy-efficient pumping of fluid. Hence, in this study, we have discussed two such natural systems, which are known for their efficient mass-transfer and pumping of fluid.

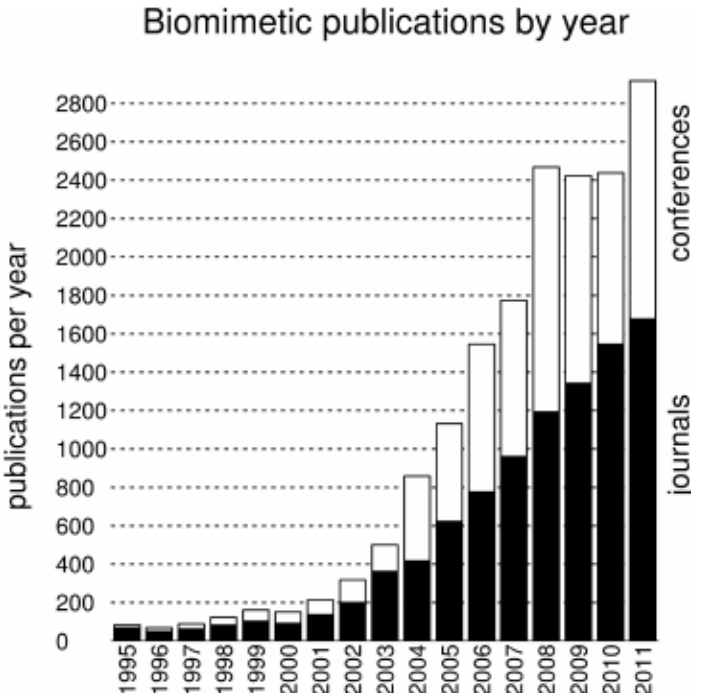

Figure 2.1 Volume of publications per year in an area of biomimetics and bio-inspiration[26]

2.1.1. Fish Gills

One of the most efficient gas-/solute-exchange systems that developed in an early evolutionary stage of living beings was gills in fish. The outstanding functioning of fish gills as an excellent gas exchanger is without any trade-offs. The structure of fish gills supports the transfer of gases and metabolites efficiently from an aquatic surrounding to a fish's body. Moreover, the fish gills are capable of extracting oxygen from the water medium under extreme environments: from brackish sea water to murky lakes in which oxygen partial pressures are abysmally low[27, 28].

The uniqueness of a fish gill lies in its hierarchical multiscale structure and functioning. The fish gills' hierarchical structure is shown in Figure 2.2. The gills of fish comprise a parallel array of thin epithelial matrix that encases complex bifurcating vasculature known as secondary lamella. These secondary lamellae are stacked in parallel over primary lamellae, which are arranged in a rack, such as the structure shown in Figure 2.2. Such an arrangement of functional units of fish gills dramatically increases the surface area-to-volume ratio. The thin epithelium layer in the secondary lamellae provides a shuttle barrier between an aquatic environment and a fish's blood. The blood runs in a vascular

network that is encased in secondary lamella, as shown in Figure 2.2. The primary lamella is attached to a stem from where two primary blood vessels, namely, an efferent artery and a vein run in parallel. They are further subdivided into capillaries and sub-capillaries while entering the secondary lamellae. As fish swim in water, the concentration gradient of gases/solute across an aquatic environment and fish's blood drives an exchange of gas and metabolites through the high surface area that is offered by the thin epithelial barrier of the secondary lamellae. The lamellae execute a majority of functions such as respiration, excretion single headedly, which are carried out by the pulmonary and the renal system in mammals[29]. Thus, exchange of gases/solutes is primarily driven by the convection-diffusion phenomenon, which occurs at the site of each secondary lamella of fish gills[30].

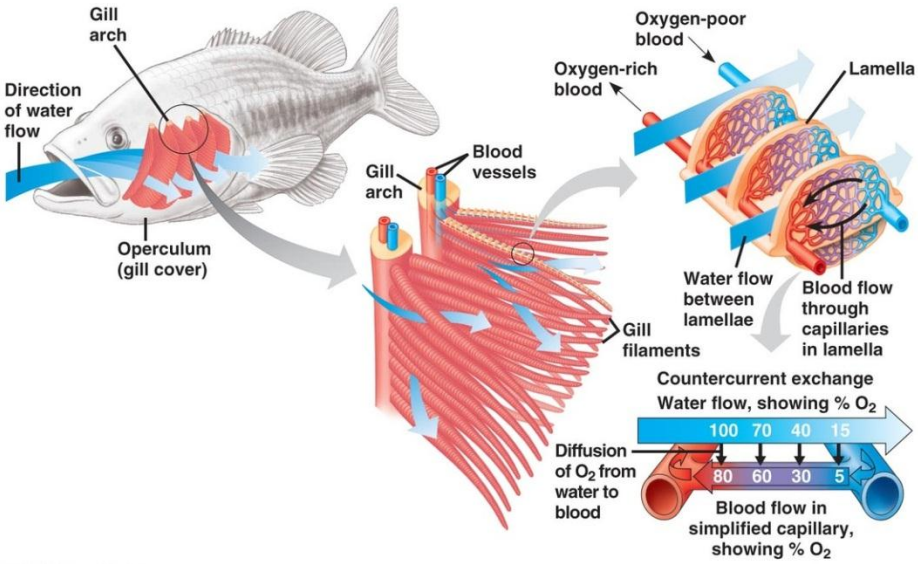

Figure 2.2 Schematic of the multiscale architecture of fish gills, demonstrating exchange of oxygen from ambient water to the body of the fish[31]

The water flows through interlamellar spaces between the secondary lamellae of fish gills. The cross-current flow of water and blood in between the secondary lamellae and the blood capillaries, respectively, and the corresponding concentration gradient of gases and metabolites, which cause a highly efficient diffusion pathway, produces a high mass-transfer ratio. This counter-current flow system always maintains a low concentration of oxygen in the blood as compared to concentration of oxygen in the water that flows between the

secondary lamellae of fish gills. Consequently, this leads to continual diffusion of oxygen into the blood. Figure 2.2 explains the role of the cross-current flow system during the highest possible level of the exchange of gas and metabolites between the aquatic environment and the blood vessels[32]. This clearly illustrates the role of the direction of fluid flow in fish gills in maintaining a sustained concentration gradient and continuous diffusion flux of gases/solutes. The fish swallow water through their mouth and then direct the water so that it flows through the interlamellar space. Meanwhile, they also pump blood through blood capillaries that are encased in secondary lamella with enough velocity to allow for maximum diffusion of gas/solute from the water that flows in the interlamellar spaces. Thus, the fractal design of fish gills and micro/nanocapillaries that are encased in thin secondary lamella support efficient flow of water and blood, respectively.

There have been numerous attempts to understand through experimental and computational methods the reasons behind the excellent gas/solute exchange capabilities of fish gills[30, 33-35]. However, enough understanding has still not been gained to mimic gills in order to develop better gas/solute exchange devices. So, in order to mimic the structure of fish gills, one needs to understand the role of the architecture of fish gills at different length scales in the gas/solute exchange process. Such knowledge will guide the design and fabrication of integrated structures at various length scales to develop devices that exhibit high gas/solute exchange.

2.1.2. Leaves of plants

Leaves have venation networks that are branched or rectilinear and are connected to the branches of the tree by a petiole, as shown in Figure 2.3. They are the most intriguing of planar structures that support the pumping of water in trees to a height of several metres against gravity by using pressure and chemical potential gradient. Water is absorbed in bulk by osmosis in the roots and then it is pumped upwards by the negative pressure that is developed in leaves by the process of transpiration. The water is distributed within the leaves after being pumped by the capillary action of the xylem networks of the trunk. The venation pattern (capillaries and microcapillaries) throughout a leaf facilitates the even distribution of water. Subsequently, water leaves the vascular bundles (veins) and migrates towards the

interstitial spaces of the spongy epithelial cells (Figure 2.3). During the day, due to photosynthesis, the water diffuses from the interstitial spaces of the spongy cells and enters the bean-shaped stomata cell due to the chemical potential gradient. This results in the distension of the stomata cells, which creates a passage for the movement of water from the interstitial spaces of the spongy cells to the outside of the leaf (in the environment).

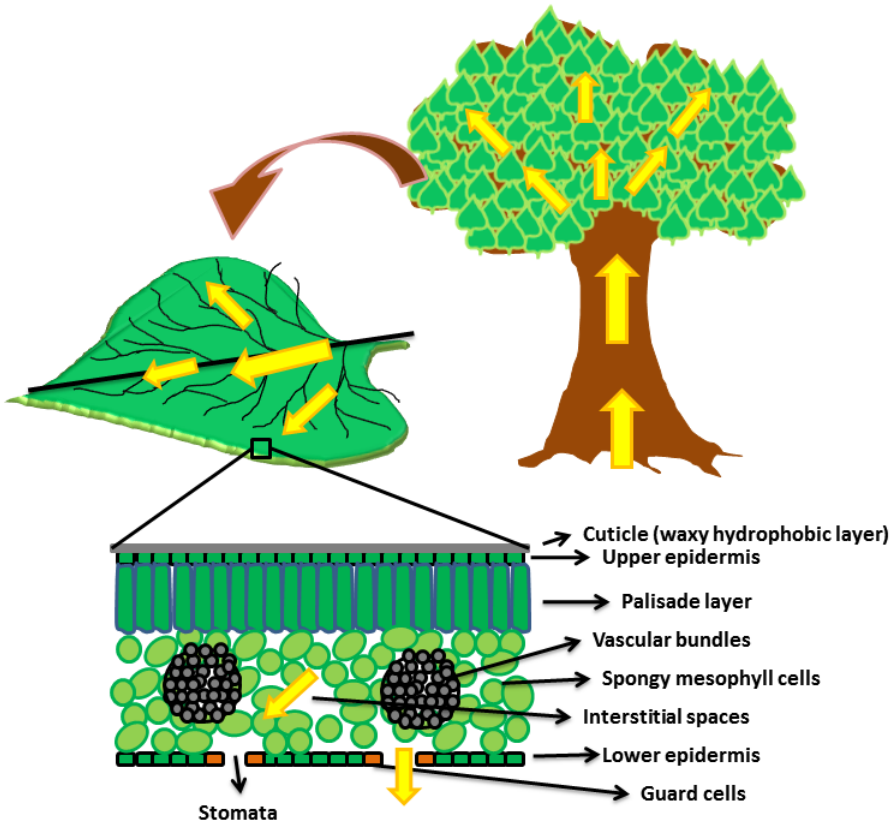

Figure 2.3 Schematic of water transport in trees. The yellow arrow represents the movement of water from the root to the leaf.

The continuous water loss from the leaves through the stomata through the process of diffusion is termed as transpiration. It results in the pumping of water from the roots via trunk. The mechanism that continuously drives water from the roots to the leaves via trunk and branches is termed as the Cohesion-Tension (CT) mechanism. The system works through the cohesive forces that exist between water molecules due to hydrogen bonding. This hydrogen bonding allows the water column in the trunks of trees to sustain the tension of

nearly 60MPa. This tension has the capability to pump water to more than 100m in height. The tension of the CT mechanism is generated by transpiration in leaves. The menisci are formed at the water-air interface of the stomata. When water molecules experience solar energy enough to break the hydrogen bonding at the menisci, they separate from the menisci and surface tension in the menisci pull water molecules to replace the lost ones. This force of tension is transmitted all along the water column of the trunk to the roots, where it causes an influx of water from the soil to the roots. This continuous flux of water from the roots to the leaves via the trunk is the water transport pathway in plants, scientifically known as the Soil Plant Atmosphere Continuum (SPAC). This mechanism of fluid pumping is attributed to the structural design of a leaf[36, 37].

The transpiration-assisted pumping of fluid in leaves is attributed to the multiscale structural design of the leaves, which includes 1) the venation system, which can deliver fluid efficiently throughout the leaf with a one-point entry of fluid 2) venation system should provide structural support to the micro/nanoporous cell and extracellular matrix (ECM) combination 3) the surface that is coated with hydrophobic waxy material, which allows higher transpiration on either its dorsal or ventral surfaces 4) the continuously decreasing pore size from the petiole to stomata, which drives fluid till the spongy cells and 5) the transpiration rate from the leaves surface should match with the capillary flow rate, thereby preventing the phenomenon of embolism through cavitation and supporting sustained pumping of water. Several attempts have been made to design and develop a synthetic tree in order to understand the fundamental science behind the pumping of fluid to several metres in height[38, 39]. Although a fair understanding of the pumping of water several metres high by the leaves of the plant has been gained, the designing and fabricating of devices that can attain such pumping capabilities remains an engineering challenge.

Several attempts have been made by earlier research groups to design and develop microsystems that are inspired from different natural systems such as avian lung[40], human vasculature[14-16] and human kidney[41, 42] in order to solve the problem of gas/solute exchange under convective flow processes. The bio-inspiration has also led to the development of artificial leaves that can pump fluid without the aid of an external source of

energy[43-45]. Above all, researchers have exploited biomimetic principles in order to realise the microfluidic systems that are mentioned above, solving engineering problems. Therefore, these studies prove that the bio-inspiration and biomimetic approach is a suitable and excellent method to address many engineering problems that deal with the transport phenomenon. The approach of biomimicry and bio-inspiration to develop patentable microsystems has witnessed rapid growth in the past decades, as shown in Figure 2.4. Thus, the adoption of methods of bio-inspiration, biomimicry and biomimetics appears to be promising in solving many engineering problems.

We envisage that the biomimicking hierarchical structure of fish gills can potentially lead to the development of a micro/nanofluidic system for gas/solute exchange. Similarly, the development of leaf-inspired micropumps can achieve the pumping of water in a manner that is comparable to the way natural trees pump water. The architectural design of these systems at various length scales is possible with continuous growth in material science and micro/nanofabrication technologies. The micro/nanofabrication technologies that are suitable for a particular system may not be acceptable as a generalised technique for fabrication of other microdevices. Further, the development of materials in order to overcome the problem of heat and mass-transfer have already been practised through the biomimetic approach[22]. Therefore, there is a need for continuous invention and/or innovation in the field of micro/nanofabrication technologies. They are needed to push the boundaries of the technologies in order to accommodate the level of complexity that has been understood through biomimicry in the designing of the device and in the material required. Contemporary growth of micro-nanomanufacturing technologies and biomimetic science is, therefore, vital for sustained and rapid growth of bio-inspired micro-nanosystems.

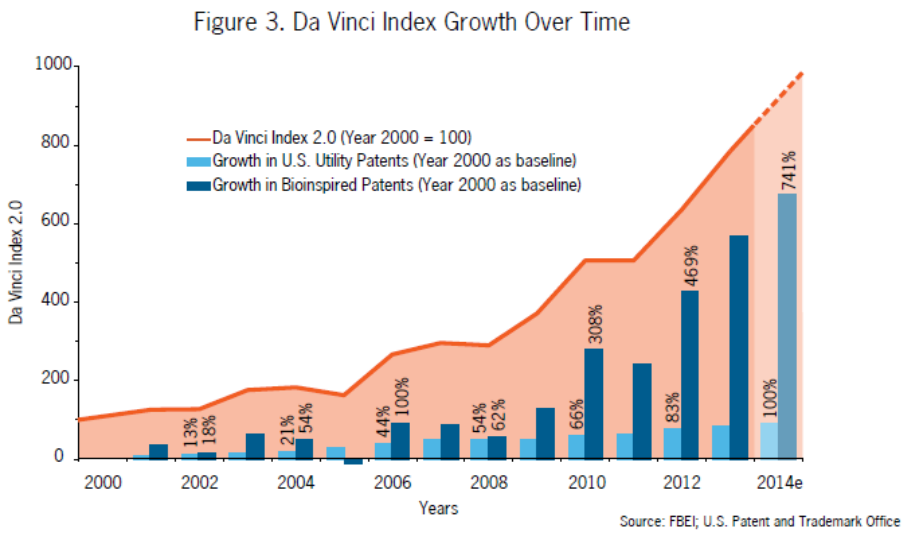

Figure 2.4 Graph showing the growth of bio-inspired and utility patents in the US over the last decade[46]

2.2. Micro/-nanomanufacturing

Micro/nanomanufacturing refers to the concept of a 'miniaturised factory' in which a manufacturing unit is established for large-scale production of micro/nanomachines and micro/nano-devices. The most significant features of these micro/nano-devices have morphological features that range from nanometres to micrometres. Such micro/nanodevices are manufactured by using different metallic, polymeric and composite materials that have dimensions that range from zero dimension to three dimensions 0-D to 3-D. Micro/nanomanufacturing results in an enhanced production capacity within a reduced space, with minimal use of energy and resources. This is possible due to a reduction size of the tools in the equipment to a microscale, which in turn reduces the mass of the equipment; increases tool speed; and reduces energy consumptions, preliminary and overhead costs, and material requirements, thereby leading to a small manufacturing cycle[47]. However, the micro/nanomanufacturing processes need to be robust enough at this scale, so that the slightest variation in the manufacturing process, which is caused by the material or the characteristics of the cutting tool, thermal variations in the machine, vibration and any number of minute changes, should not impact the ability to produce features of this type at a production scale. Generally, these micro/nanomanufacturing processes can be classified into

subtractive, additive, forming, joining and hybrid processes (shown in Table 2.1) according to the way in which the components/products are to be made.

Table 2.1 The different types of micro/nanomanufacturing processes[47]

S. No	**Manufacturing Processes**
Subtractive Processes	Micro-mechanical cutting (milling, turning, grinding, polishing and others), micro EDM, micro ECM, laser beam machining, electron beam machining, photo-chemical machining etc.
Additive Processes	Surface coating (CVD, PVD), direct writing (ink jet, laser guided), micro-casting, micro-injection moulding, sintering, photo-electroforming, chemical deposition, polymer deposition, stereolithography etc.
Deforming Processes	Micro-forming, stamping, extrusion, forging, bending, deep drawing, incremental forming, super plastic forming, hydro-forming, hot-embossing, micro/nano-printing etc.
Joining Processes	Micro-mechanical assembly, laser-welding, resistance, laser, vacuum soldering, bonding, gluing, etc.
Hybrid Processes	Micro-Laser-ECM, LIGA and LIGA combined with laser machining, micro EDM and laser assembly, shape deposition and laser machining, Efab, laser-assisted micro-forming, micro-assembly injection moulding, combined micromachining and casting etc.

The micro/nano-devices and micro/nanomachines that are fabricated by the processes mentioned above have applications in the burgeoning field of microfluidic devices, as also in Micro Electro Mechanical Systems (MEMS) devices. Microfluidics deals with the design, development and working with fluids and gases in channels with cross-section dimensions of less than 100μm. Owing to the reduction in the dimensions of channels, the fluid experiences surface forces and their effects dominate the body forces and bulk properties of the fluid. The physics that govern the behaviour of the fluid is quite different from that which observed at a macro-scale flow. Thus, the fluid flow remains laminar in nature, offering an exciting platform to explore and employ a number of phenomena and applications. However, certain interesting transport phenomena have been observed when one of the characteristic dimensions of the channels is further reduced below 100 nm[48]. Such flows are termed as nanofluidic flows. In the field of nanofluidics, nanochannels are primarily represented by nanoporous matrix/nanopores, nanotubes and nanoslits[49]. These flows under such

dimensions are suitable for the single cell, biomolecule, nanoparticle manipulations; they also support the study of phenomena at a molecular length scale. These altered flow behaviours offer unique opportunities to exploit these systems for different engineering and medical applications.

One of the earliest known microfluidic devices dates back to 1970, when researchers at Stanford University conceptualised and fabricated a miniaturised gas chromatography (GC) unit[50]. This work opened a gateway for the mushrooming of miniaturised devices, which find applications in molecular analysis, biodefence, biochemical analysis, microelectronics, clinical diagnostics, and drug screening and development. Apart from the miniaturisation, these micro/nanofluidic devices have numerous advantages such as decreased cost of manufacture, use, and disposal; rapid analysis; reduced consumption of reagents and analytes; reduced production of potentially harmful by-products; increased separation efficiency; decreased weight and volume; and increased portability. However, the real outburst of micro/nanofluidic devices occurred after the birth of the field of genomics[51]. Further, the demand for accurate manipulation of biochemical analysis with minimal reagents gave additional impetus to the accelerated growth of micro/nano fluidic technologies[52]. To cope-up with increasing demand, the direct translation of silicon- and glass-based microtechnologies for the manipulation of chemical, bio-analytes, gases and others started gaining momentum. However, the limitations of using glass and silicon as working materials in chemical and biological applications triggered the search for materials that could be processed by microtechnologies that were borrowed from the silicon industry and, at the same time, would be capable of handling chemical and biological entities [51].

The introduction of polymer materials provided an excellent platform that amalgamated well with traditional micro/nanofabrication processes, while being suitable for chemical and biological applications at the same time. The optical, mechanical, electrical, chemical and biological advantages that are offered by polymers have placed them as a good choice of material for design and fabrication of micro/nanodevices. Although multiple fabrication processes are listed in table 1, the primary process of fabrication of micro/nanofluidic devices in polymers has been lithography-based techniques. These

techniques are thick resist lithography, soft lithography, micro-stereolithography, electron beam lithography, focused ion beam lithography, nano-imprint lithography, sphere lithography, interference lithography and others. These techniques have enabled the fabrication of morphological features in silicon/metals/polymers within a finite range of dimensions. These morphological features can act as negative mould in the developing of channel patterns in polymers by the process of casting/micromoulding. However, these processes are hardly suitable for the fabrication of multiscale, 3D morphologies in microdevices, which are commonly observed in nature. Further, the challenges of substrate compliance for the integration of different lithographic techniques confine their potential applications. Nevertheless, the versatility of lithography-based techniques has positioned them as one of the mainstream manufacturing processes for micro/nanofluidic devices, at least at a lab scale. Therefore, various modifications in lithography techniques in conjugation with other microtechnologies have been explored to generate micro/nanomorphologies on polymeric substrates. For instance, membrane-assisted microtransfer moulding (MA-uTM) has been proposed to create complex 3D microstructures that have a high aspect ratio. The method overcomes many topological constraints of soft lithography, creating the possibility of a large-scale production of true 3D microstructure[53]. However, due to complex fabrication processes, limited choice of materials, restriction in the dimensions of the features that are obtained, such processes still need improvement. A relatively simple yet elegant method of fabrication for the generation of a nanochannel array that is free of lithography on polystyrene substrate was proposed by Bi-Yi Xu et al. and K L Lai et al.. They exploited the cracking process on the surface of a polystyrene (PS) Petri-dish, which was composed of uniaxial macromolecular chains. The ambient conditions allowed the generation of equal-spaced parallel nanochannels with control over the channel depth, from 20 nm to 200 nm; the channel length spanned tens of millimetres. Further, nanochannel array on PS has been successfully replicated in PDMS through micromoulding[54]. K L Lai et al. utilised solvent-vapour-assisted imprinting lithography (SVAIL) to generate nanopatterns (<100nm) on PS/PMMA thin film[55]. Although these processes demonstrated an easy, cost-effective, fast method of micro/nanomorphologies, they were on a planner 2D substrate. Moreover, the control over the channel dimensions and their pattern remains an issue, which needs to be attended to before using the methods mentioned above in large-scale fabrication

methodologies. The quest for 3D micro-/nanochannels-based devices, which are demanded by complex applications such as tissue engineering, self-healing, cooling of materials and such others, can be achieved by stacking 2D layers that have micro/nanochannels[56]. Therefore, Guo You Huang et al. fabricated microfluidic 3D fluidic devices for tissue engineering by stacking 2D microchannels that had porous cell-laden agarose hydrogels that were formed by photo patterning poly (2-hydroxyethyl methacrylate)[57]. In spite of these developments in soft lithography, the challenges of generating monolithic 3D devices with reproducible micro/nanochannels still persist. It has led to a technology shift from soft planner lithography to stereolithography. Microstereolithography has led to the fabrication of micro/nanodevices with photo polymerisable polymers[58]. The successful fabrication of microgears, microtubes and micro convex cone structures, which have 3D complex shapes with a wide variety of functional materials that have high aspect ratios with microstereolithogarphy (MSL), has been reported[59]. H. Selvaraj et al. have demonstrated the use of the femtosecond laser in microstereolithography for the rapid curing of PDMS in order to obtain microspatial resolution within a micro-timescale, which generates 2D/3D microstructures that have a dimension of 15–20μm[60]. Due to the problems such as unavailability of photopolymerisable polymers for fluidic applications, optical resolution over the minimum feature size, vulnerability to vibration and operational expertise, the utility of MSL has been limited in the field of micro/nanofluidics. Although these technologies were able to fabricate micro/nanofluidic devices in a polymeric substrate that had one or other features such as three-dimensionality, multiscale morphologies, and ease of fabrication, scalability and cost effectiveness, these technologies are still unable to fabricate micro/nanomorphologies in a polymer that has all of the features described above.

Recently, the combinations of micro/nanotechnologies such as electro spinning with soft lithography have demonstrated the generation of channels with the desired micro/nanodimensions. Researchers have fabricated circular micro/nanochannel networks in a PDMS substrate by the removal of electrospun nanofibrous polymer fibres that are moulded through soft lithography. They further showed the formation of a robust channel with the desired dimensions and fluid flow through it without leakage or blockage as problems of nanochannels[61]. Later, Leon M. Bellan et al. 2008 demonstrated that the

sacrificial removal of electrospun polyethylene oxide nanofibres in polydimethylsiloxane (PDMS) generated a random network of nanocapillaries that resemble microcapillary networks in living beings[62]. Thus, electrospinning is emerging as a promising technology for the generation of a random or patterned fibre network (with dimensions spanning microns to nanometres), which can be used as a sacrificial element in polymer matrices to generate a micro/nanochannel network. The process enables the manoeuvrability of the dimensions of the channels, scalability in terms of size and production capability, requires much less expertise in operation and is able to generate monolithic, 3D micro/nanofluidic devices that are desirable in many applications. This method of fabrication of 3D channel networks in polymer matrices appears to be promising for further exploration. However, advancement in the fabrication of 3D micro/nanofluidics must be complemented with growth in the field of membrane technologies to lay a platform for the development of micro/nanofluidics for separation applications.

2.3. Micro/nanosystem integrated with membranes

The membrane separates the two homogenous media as a selective barrier. Under the influence of chemical or pressure potential, molecules such as solutes, gases and biomolecules pass from one media to another. The amount of molecules that get separated across the membrane depend on the driving potential, the thickness of the membrane and the nature of the membranes. The nature and the classification of membranes are based on the processes they are used for, as shown in the Table 2.2. One of the most common polymeric membranes that have been employed quite often for separation of small molecules such as gases/solutes in the fluidic device has been the polydimethy siloxane (PDMS)[63]. Moreover, PDMS is also one of the most suitable materials for the fabrication of micro/nanofluidic devices. Thus, PDMS can be a common material that allows easy integration of the field of micro/nanofluidics and membrane technology.

Table 2.2 Classification of membranes on the basis of their nature and application area[5, 64]

S. No	Processes	Through component	Interception components	Mechanism of separation	Examples of polymer used as membranes
1	Ultrafiltration	Small molecule Solution	Macromolecular solute with 1-2nm	Screening	cellulose acetate, polyvinylidene fluoride, polyacrylonitrile, polypropylene, polysulfone, polyethersulfone
2	Microfiltration	Solution, Gas	Particles with 0.02-10μm	Screening	cellulose acetate, polyvinylidene fluoride, polyacrylonitrile, polypropylene, polysulfone, polyethersulfone
3	Nanofiltration	Solvent, Low-valence small Solutes	Solute greater than1nm	Donna solution-diffusion Effect	cellulose acetate or ployamide materials
4	Reverse Osmosis	Solvent, Interception Component by electrodialysis	Small molecule solute with 0.1-1nm	Preferential adsorption, Capillary flow, Dissolution – diffusion	cellulose acetate or ployamide materials
5	Dialysis	Small solutes	Interception for Greater than 0.02μm	Screening, Hindered, diffusion in microporous, membrane	polyacrylonitrile, polysulphone, polyaryethersulphone, polyamide and polymethylmethacrylate, cellulose triacetate

6	Gas separation	Gas, Soluble component in membranes	Larger component	Pressure difference, Concentration Difference	polyamide or cellulose acetate, or from ceramic materials, PDMS

The separation mechanism of the gases through PDMS is based on sorption-desorption followed by diffusion. Bell and Gerner et al., in 1989, studied the separation mechanism and demonstrated that in a rubbery polymer membrane such as PDMS, the permeability is determined by the solubility behaviour of polymer to a large extent. The permeating behaviour of organic compound such as alcohols, acetone and water were measured in the PDMS membrane[65]. Nijhuis and Mulder et al., in 1991, formulated a resistance-in-series model to describe the pervaporation performance of elastomeric membranes during the removal of volatile organic components from water. The mathematical model describes the organic component flux as a function of the feed concentration, the permeability of the organic component in the membrane, the membrane thickness and the liquid boundary layer mass-transfer coefficient. Authors experimentally showed that the importance of the hydrodynamic boundary layer resistance is rate-determining in a mass-transfer operation in the case of a highly permeable polymer such as PDMS. The effect becomes more dominant with a decrease in the thickness of the membrane of the PDMS[66]. In an another article, Bhattacharya and Hwang et al. in 1997 formulated a generalised equation the related the concentration polarisation that occurs in the boundary layer to the modified Peclet number and demonstrated its applicability in a majority of membrane-separation processes such as gas separations, reverse osmosis, ultrafiltration, pervaporation, and dissolved-gas permeation in liquid. The factors that determine the extent of polarisation are the membrane permeability, the separation factor (or solute rejection), the membrane thickness, the boundary layer mass-transfer coefficient and Henry's law coefficient[67]. Zang et al., in 2009, showed that the cross-linking density and surface properties of PDMS membranes can be manipulated by using different cross-linking reagents to influence the pervaporation performance of ethanol/water mixtures significantly. Such modification due to the cross-linker and its concentration affects the free volume and surface of the membrane, thereby enabling changes in the selective diffusion of certain species. Recently, the PDMS

membrane has been employed in the separation of gases such as oxygen, carbon dioxide, nitrogen, and ammonia from a gas mixture or that which is dissolved in water. The separation of any gas from a gaseous mixture depends upon the interaction of gases with the PDMS and their solubility in the PDMS[68]. Thus, the PDMS membrane can be a potential membrane for separation of small molecules such as solutes, organic compounds, gases, solvents and others.

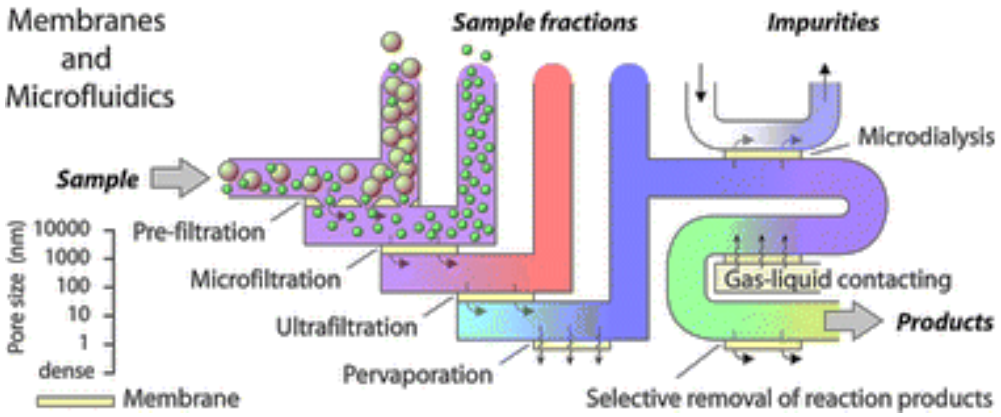

Figure 2.5 Schematic showing the integration of microfluidics and membrane technology in various unit operations[6]

These PDMS membranes need to be integrated in microfluidic devices to carry out unit operations such as separation, purification, pre-treatment, reaction and others at a microscopic scale for various chemical and biological applications, as shown in Figure 2.5. This marriage of the two emerging fields, microfluidic technology and membrane technology, will grant scientists and engineers new tools to revolutionise the field of chemical and biological engineering[6]. These devices have a wide range of applications in different areas such as gas separation, pervaporation, desalination and waste water treatment. They also find application in fuel cell membrane[69], tissue engineering[70] and other biomedical applications such as dialysis and oxygenation[71]. In spite of such applications, such devices are still restricted to the lab scale. The major hurdle to be overcome in the integration of membranes in micro/nanofluidic devices is the challenge of scalability in manufacturing. The simple type of membrane and microfluidic network integration is the direct clamping or gluing of the commercially available membranes between two

microfluidic network chips. Membrane integration with microdevices can also be achieved during the MSL process[6]. The disadvantages that are associated with this method are weak bonding, leakage and such others. The shortcomings of the above method facilitated the need to explore alternate methods of membrane integration into a fluidic chip. The researchers have moved to in situ fabrication of the membranes of the desired dimension while the fluidic devices are being operated. For instance, Moorthy and Beebe prepared a porous membrane in a microfluidic network by emulsion photo polymerisation[72]. Hisamoto et al. utilised an interfacial polycondensation reaction for design and synthesis of chemically functional polymer membranes[73]. Thereafter, the fabrication of the membrane during the fabrication of the fluidic device was practised by borrowing the technology directly from the silicon industry. Further, advancement in nanotechnology has allowed a high degree of tailorability in the fabrication of a porous material. It resulted in the formation of micro/nanoporous silicon, zeolite or polymeric membranes that are connected to the microdevice during the fabrication of the device itself. The major obstacles were the costly processes and the expert levels of techniques that were required for the generation of the membrane with fluidic chips, making it less popular among resource-deficient labs or organisations. However, method of fabrication of a porous membrane during fluidic device manufacturing appears to be better method because it creates an integrated device with a fluidic channel and a membrane, a monolithic device. Therefore, a suitable, cost-effective method for the fabrication of a membrane during microfluidic device manufacturing needs to be explored.

2.4. Transport phenomenon

2.4.1. Convection-diffusion phenomenon

The convection-diffusion phenomenon is one of the most ubiquitous phenomena that are prevalent in nature. It is a phenomenon that is responsible for entry and exit of oxygen and carbon dioxide, respectively, in or from a living body; the supply of oxygen and nutrients to the tissue; and the removal of waste carbon dioxide from the tissues by the blood vessels. Moreover, such phenomena are also the corner stone of various engineering devices such as the cooling circuit in microelectronics, desalination of water through membranes, diagnostic

devices and many others. Due to their importance in a number of applications, they have been extensively researched.

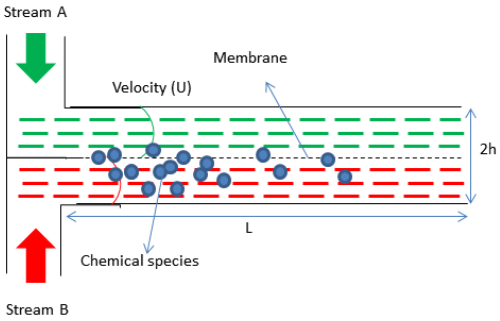

Figure 2.6 Schematic showing convection-diffusion in a microchannel partitioned by a permeating membrane

Whenever there is transport of dissolved species (solute/gases) in a fluid that flows through a duct, the presence of the concentration gradient, either in the direction of the flow or perpendicular to the direction of flow will drive the diffusion of species till the equilibrium of concentration is attained. However, the presence of bulk fluid motion and convection, will also contribute to the flux of chemical species in the direction of the fluid flow. Therefore, the coupled phenomena of diffusion and convection can be represented by the equation,

$$N_i = -D_i \nabla C_i + U C_i \tag{2.1}$$

$$\frac{\partial c_i}{\partial t} + \nabla \cdot N_i = R_i \tag{2.2}$$

Although such phenomena exist at every length scale, they exhibit interesting behaviour at a micro/nanoscale. The microchannels allow flow with a small Reynolds number, leading to flow in a Stokes regime. The fluid flows in microchannels are laminar in nature, as shown in Figure 2.6. The two streams of fluid (red and green) enter the channel with the same velocity, thereby creating a virtual boundary between two steams, represented by a dashed line (Figure 2.6). At a steady state, the velocity fields that lead the streamlines do not cross each other in a laminar flow. The mass transport occurs tangential to the velocity field, preventing mass-transfer between the adjacent fluid layers. Thus, mass-transfer that is normal in the velocity field occurs only by the process of diffusion in the microchannels. There are two competing phenomena, convection and diffusion, during the fluid motion, as

shown in Figure 2.6. The dominance of one phenomenon over the other can be predicted during the flow by a dimensionless number, Peclet Number. The Peclet number is defined as the ratio of the contribution of mass transport by convection to mass transport by diffusion.

$$Pe = \frac{N_{conv}}{N_{diff}} = \frac{|u|C_i}{D\nabla C_i} = \frac{LU}{D} \tag{2.3}$$

where L is a characteristic length scale, U is the velocity magnitude and D is a characteristic diffusion coefficient of the chemical species. The Peclet number for mass transport is analogous to the Reynolds number for momentum transport. If the value of the Peclet number is greater than one for a system, the effect of convection exceeds that of the diffusion in mass flux. Such cases arise in a system that has channel dimensions that are greater than a micrometre. Since the Peclet number is proportional to the size of the system, it can be observed that at a smaller length scale, diffusion phenomena dominate convection in a mass flux. Moreover, the Peclet number for the transport that is normal in the fluid flow is zero because diffusion is the only phenomenon that is responsible for the mass transport that is normal in the flow field. Thus, in a microchannel, the time scale for the fluid to traverse a length of channel is given by L/U. The diffusion length, L_{diff}, which is normal to the direction of flow in a channel, can be given by

$$L_{diff} = 2\sqrt{Dt} = 2\sqrt{D\frac{L}{U}} \tag{2.4}$$

Considering that there will be a high degree of mixing when the diffusion length scale exceeds the channel width, h, we can state that the mixing is effective where

$$\frac{L_{diff}}{h} \gg 1 \tag{2.5}$$

That is, a large value of the following dimensionless number will ensure a high degree of mixing

$$\theta_{mix} = \sqrt{\frac{DL}{Uh^2}} \tag{2.6}$$

Thus, the degree of mixing can be increased by narrowing the channel dimension, increasing the length of the channel and decreasing the flow velocity through channels.

These factors can be easily tailored in micro/nanofluidic devices to achieve a high degree of mixing. However, if the two streams in Figure 2.6 are separated by a permeating membrane, then instead of mixing, separation of chemical species from one stream to another can be achieved. Such a phenomenon is prevalent in the gills of fishes, which shall be discussed in the chapters to follow.

2.4.2. Capillary flow:

Capillary flow is an ability of fluid to flow in a narrow channel without the aid of any external power source. The flow is driven by the interaction between the surface tension of the fluid that is in contact with a microstructure of the substrate that has a narrow channel. The chemical properties of the substrates and the dimensions of the channel interact with a small volume of fluid to initiate the spontaneous movement of fluid by minimising the Gibbs free energy at the interface of air, solid substrate and the fluid. The guiding capillary pressure (P) is strongly dependent on the diameter (2R) of the channel and is given by the expression,

$$P = \frac{2\sigma \cos\theta}{R} \tag{2.7}$$

However, the direction and magnitude of the capillary pressure is dependent on the cosine of angle (Θ) that is formed by the contact line. The sign of the cosine of the angle determines the hydrophilicity or hydrophobicity of the channel in the substrate. The magnitude of the angle is strongly dependent on the surface morphologies of the inner wall of the channel and the chemical nature of the substrate. The roughness introduced by micro/nanomorphologies on the substrate will increase the hydrophobicity of hydrophobic substrate and decrease the hydrophobicity of hydrophilic materials. Thus, depending on the hydrophobic nature, a positive or negative pressure gradient is developed, which drives the fluid in the channels. Further, the magnitude of the capillary pressure is also dependent on the diameter of the channel and the surface tension of the fluid, as shown in equation 2.7. Therefore, a reduction in the channel diameter leads to an increase in the capillary pressure, which drives the flow through the channels. The capillary force is responsible for a number of real-life phenomena such as rise of fluid to several metres in tress, wicking through a bundle of fabrics and porous materials, percolation of water in soil and such others. The capillary force is sometimes able to drive fluid against gravity.

The capillary fluid flow in a horizontal microchannel that has a circular cross-section which is connected to a reservoir is shown in the figure. When a fluid encounters narrow channels, it forms a contact angle depending on the hydrophobic/hydrophilic interaction with the substrate material. Thereafter, the contact angle creates a positive pressure, which drives the fluid through the channels. The viscous drag experienced by the flowing fluid is directly related to the length of the liquid column inside the channel. The dynamics of the capillary flow in a horizontal microchannel can be given by the equation below.

The unsteady state equation for a Newtonian viscous uncompressible laminar fluid flow is governed by equation (2.8). The force balance equation for the capillary driven flow in micro/nanochannels is

$$\boldsymbol{F_{inertial} = F_{capillary} - F_{viscous\ drag} - F_{energy\ dissipation\ due\ to\ wall\ friction}}$$

The transient equation that governs the capillary dynamics in micro/nanochannels[74] is given by

$$\frac{d\left(\rho\pi R^2 l\frac{dl}{dt}\right)}{dt} = \frac{2\sigma\pi R^2 cos(\theta)}{R} - \frac{8\pi\eta l dl}{dt} - \frac{f\rho\pi R^2}{2}\left(\frac{dl}{dt}\right)^2 \quad (2.8)$$

Where R is the radius of the micro/nanochannels, ρ is the density of the fluid, σ is the surface tension of the fluid, θ is the static angle which the fluid-free surface makes with the capillary wall, η is the dynamic viscosity of the fluid, f is the constant of energy dissipation, l is the wetting distance that is moved by the fluid in the micro/nanochannels, and $\frac{dl}{dt}$ is the velocity of the capillary flow. The capillary force at the meniscus is given by the Young–Laplace equation, 2σcos (θ)/R; the viscous force in fully developed flow is given 8πη⌊v; and the friction force by $fv^2/2$.

$$\frac{d\left(l\frac{dl}{dt}\right)}{dt} = \frac{2\sigma cos(\theta)}{R\rho} - \frac{8\eta l}{\rho R^2}\frac{dl}{dt} - \frac{f}{2}\left(\frac{dl}{dt}\right)^2 \quad (2.9)$$

If the frictional force is ignored, the differential equation given in the equation (2.10) can be solved analytically. The relation between the distances traversed by the capillary in the

micro/nanochannels in the given period of time can be established by solving equation (2.10).

$$\frac{d\left(l\frac{dl}{dt}\right)}{dt} = \frac{2\sigma cos(\theta)}{R\rho} - \frac{8\eta l}{\rho R^2}\frac{dl}{dt} \tag{2.10}$$

The equation above was solved to determine the dependence of the length that was traversed by the fluid by capillary action in the micro/nanochannels. The capillary dynamics depends on the various factors such as contact angle, dimension of the micro/nanochannels, and viscosity of the fluid that flows through the micro/nanochannnels.

$$l^2 = \frac{2At}{C} - \frac{2A}{C^2}[1 - e^{-Ct}] \tag{2.11}$$

Where,

$A = \frac{2\sigma \cos\theta}{R\rho}$ and $C = \frac{8\eta}{\rho R^2}$

The capillary length, *l*, is dependent on time, *t*, as well as on the constants, *A* and *C*. The capillary length increases linearly with time in the beginning and, thereafter, the rate of increase in the capillary length is retarded due to domination of the viscous force, which scales as the length of the liquid column in the micro/nanochannels. Further, the capillary length is strongly dependent on the viscosity of the fluid as well on the diameter of the micro/nanochannels.

When there is vertical movement of the water column in capillaries as observed in trees, the forces of gravity dominate the viscous forces, and in equation (2.8), the viscous force is replaced by the force of gravity.

$$\frac{d\left(l\frac{dl}{dt}\right)}{dt} = \frac{2\sigma cos(\theta)}{R\rho} - lg \tag{2.12}$$

On solving the equation (2.12), we get the capillary length in the vertical capillaries.

$$l = \frac{2\sigma \cos\theta}{\rho R^2}t - \frac{g}{6}t^2 \tag{2.13}$$

Here, the capillary length is dependent strongly on the radius of the capillary tube but it decreases with the second power of time of rise of fluid.

2.5. Problem definition

The major problems that exist in realising the true potential of 3D micro/nanofluidic devices are the manufacturing processes and the materials that are employed in intended applications. Although researchers have attempted to address biomedical/chemical problems by using micro/nanofluidic devices, the inherent limitation of the material and the manufacturing process is the current road block for scale-up of production and applications. Therefore, manufacturing by tradition lithography, which is borrowed from the silicon industry, needs to be replaced by advanced, scalable and fast micromanufacturing processes by using polymer materials, which can overcome the limitation of small molecule diffusion and is useful in biomedical and chemical industries. Recently, vascularised polymers have attracted the attention of researchers for being one of the most coveted material systems in modern applications such as tissue engineering, advanced drug delivery, self-healing and cooling material, artificial organs, and cell culture under complex microenvironments. The method of vascularisation dates back to 2008–2009, when sacrificial materials were impregnated in host materials and later etched away by thermal or chemical treatments to pave the way for vascularization[75, 76]. The patterns of vascularisation that were targeted by researchers were either simple three-dimensional arrays of channels or a random network of channels. The prominent features of these vascularised polymers are that they can overcome the diffusional limitations during an application and that they are also amenable to scale-up fabrication. Although researchers have succeeded in developing a scalable manufacturing process to develop a material that can overcome diffusional limitation, the work is still in its infancy. These vascularised polymers that are reported in literature have channel dimensions either in 10s of microns, which support pressurised flow through a tubular conduit; or in nanometres, which only favour capillary fluid flow. Further, the vascularised polymers were majorly produced in substrate materials, which either supported tissue engineering application or just demonstrated the applicability of the process in producing vascularisation in materials. Thus, the pattern of vascularisation, which plays a pivotal role in the fluid flow behaviour and nature of materials in mass transport operation, has been hardly explored by previous researchers. Hence, there is a need of multiscale channel network mimicking of natural vascular systems in polymer matrices, which can enable high volumetric flow

through nanochannel networks, thereby utilising the large surface area promoted by nanovasculature. In addition, factors that affect the fluid flow and mass-transfer in vascularised polymers need to be understood before they are used in intended applications. Thus, the designing and fabricating of a vascularised polymer that not only allows a high volumetric flow but also enhanced mass-transfer capabilities is desirable. Thus, 3D micro/nanofluidic devices that are fabricated on the foundation of vascularised polymer matrices for membrane oxygenators, kidney dialyser or any other lab-on-chip/organ-on-chip devices cannot materialise before the issues discussed above are addressed.

We hypothesise that biomimicry of the secondary lamella of fish gills and tree leaves at different length scales will enable us to design and fabricate multiscale, 3D micro/nanofluidic devices for enhanced gas/solute exchange and better, passive fluid pumping devices'.

2.6. Research aims and objectives

1) Computational and theoretical study of the structure of fish gills at a macroscopic and microscopic level to determine the factors that affect their gas/solute exchange performances.

2) Design and fabrication of a novel bio-inspired, multiscale vascularisation pattern in thin polymer matrices through simple, scalable and inexpensive microtechnologies to support fluid flow and mass transport.

3) An experimental and theoretical investigation of the factors that affect the fluid flow and mass transport capabilities in three-dimensional micro/nanofluidic devices that are developed from micro/nanovascularised polymers matrices.

4) Design and fabrication of leaf-inspired micropumps through simple, scalable microtechnologies, and study of the role of different parameters that affect the passive pumping of fluid by the micropump, through experimental and theoretical methods.

3. Chapter 3 Computational Work

3.1. Introduction

The separation of gases, solutes and solvents under convective flow condition is a requirement in a number of applications like artificial kidney dialyser, extra corporeal membrane separators, water filtration, desalination and others[77, 78]. The biomimicry has been used to solve above engineering problems in the recent years by drawing an inspiration from natural systems like avian lung, human lungs, a human kidney, human vasculature etc.[13, 17, 40]. However, the challenges of developing compact, efficient gas/solute exchange devices still persist. To achieve the above objective, the design of a device need to be improved by taking inspiration from a simple, yet elegant, gas/solute separating organ system. One of the primitive known gas/solute separating organ systems in nature is fish gills. Gills can be taken as a model design for the development of better gas/solute exchanger. The major features which distinguish gills from other natural systems are their ability to extract oxygen from water even at a very low partial pressure, having the highest ventilation volume among all species, having design leading to continuous efflux of oxygen from ambient to the blood vessels and an overall compactness of the organ system[79]. Therefore, fish gill needs to be thoroughly studied at different length scales to determine the reasons for it to be an excellent gas/solute exchange organ in nature for centuries. The knowledge of fish gills' design generated through above study can lead to the development of microfluidic devices for better gas/solute separation.

The gills from different varieties of fishes have been studied for a long time from their physical, morphological, structural and biochemical point of view[29, 30, 80, 81]. However, the knowledge of fish gill architecture and morphometrics in the light of their gas/solute exchange capabilities still need considerable attention. The basics structures of gills and their role in gas/solute exchange have been well elucidated in a detailed through a series of publications by Hughes et al[32]. Through anatomical studies, they have calculated the dimensions of gills of different fishes at multiple length scales[82]. Further, they have also established the role of above determined morphometric factors like thickness of blood-water barrier, shape, size and arrangement of secondary lamellae, on the gas exchange capacities in different weights of fishes [83, 84]. Their study suggested that surface area of

gills, which is responsible for gas/solute exchange, scales with the weight of fishes. Another prominent finding which they reported was the counter-current flow of blood and water stream in secondary lamella and inter-lamellar space, respectively. Later, a theoretical model was developed by J. Piiper and P. Scheid to study the gas diffusion in different organ systems. Their model suggested that the effect of counter current flow on gas diffusion is better than the cross-current flow and uniform pool system, assuming the same ventilation-perfusion conductance ratio across an epithelial layer. They further substantiated their results through experimental findings in a fish, a bird and a mammal where above three modes of gas exchange operated. In addition, they also commented that the enhanced gas exchange in counter-current flow occurs in a limited range of medium-to-blood conductance ratio (around 1)[85, 86]. Their model beautifully captured the role of counter-current flow on gas diffusion effectiveness, but the role of dimensions of secondary lamella of fish gills on the effectiveness of gas/solute exchange remained elusive, except for an enhanced surface area. Later, studies carried out by K Park et al demonstrated an existence of optimal lamellar distances in fish gills irrespective of their mass for an enhanced gas exchange. Their theory and experiments effectively captured the poor dependence of interlamellar distance on the weight of fishes. Thus, they established the evolutionary conservation of these interlamellar distances in fishes[87].

Apart from macroscopic features, the microscopic properties of density, diameter, and architecture of vascular network also play a vital role in gas/solute diffusion where the actual diffusion process occurs. The role of the density of microvascular networks in a living being on gas (oxygen and carbon dioxide) exchange was studied and reported that it remain nearly constant irrespective of the mass of living being[88]. Additionally, the constant density of vascular channels in mass transport has been independently confirmed through computational methods by Janakiraman V *et al*[25] and Truslow J G *et al*[89]. Although the volume of fluid flow through secondary lamella is dependent on vascularization density and diameter of vascular channels, the mass transfer rate is dependent on the enhanced surface area offered by the increased vascularization density and available concentration gradient in the tissue. However, the vascularization density in a thin secondary lamella matrix will affect its structural integrity. The biomimetic design of secondary lamella structure with high vascularization will lead to increased cost of fabrication and less structural material, making

it hostile for any application. Therefore, it is necessary to characterize the role of vascular density on the mass transfer operation for given thickness of secondary lamella. Similarly, the diameters of vascular channels also play a key role in fluid and mass transfer in secondary lamella.

Although, above studies have identified the role of different morphometric factors on gas/solute exchange, seldom has the study been done, to the best of our knowledge, to study the structural organization of gills and parameterization of these morphometric factors in fishes with reference to gas exchange. Thus, there is a need to study and explore secondary lamella and its functional relationship with gas/solute transport in fishes and translate the knowledge gained above for design and fabrication of bio-inspired secondary lamella. Therefore, in our current work, we have theoretically studied the variation in different morphometric features and parametric ratios of fish gills in different sizes of fishes from data available in the literature. Thereafter, computationally investigation of the convective-diffusion process in a simplified model of secondary lamella at microscopic and the macroscopic level was carried out. The computational study suggested the role of parametric ratios, microscopic properties like the density of vascularization, thickness of the epithelial barrier and flow properties on gas/solute exchange in a fish gills. Further, our analysis suggested that value of these parameterized factors remain nearly conserved in fishes with different body mass and is approximately equal to the value predicted by our modeling simulation work. Thus, the current study enabled the better understanding of fish gills from the perspective of design and development of biomimetics structures for gas/solute exchange.

3.2. Theoretical study of fish gills

3.2.1. Method

The morphometric data of fish gills were mined from Huges et.al[32] is shown in Table 3.1. Thereafter, the dimensions of different features of fish gills were analyzed for their variation with respect to the weight of different fishes and reported as graphs. Further, borrowing of dimensions of fish gills directly for design and fabrication of microfluidic-based gas/solute exchanger may not be possible; therefore, we have defined few dimensional less parameter (parametric ratios) listed below.

Table 3.1 Morphometric features of different fish gills

	Wt of fish (gm)	**Inter-lamellar dist (mm)**	**Avg. PL length (mm)**	**Number of SL/mm**	**Length of SL (mm)**	**Hgt. of SL (mm)**
Trachurus trachurus	12	0.017	2.37	38	0.18	0.07
	40	0.017	4.18	39	0.25	0.1
	125	0.017	6.16	38	0.7	0.2
	135	0.02	6.14	39	0.75	0.15
Clupea harengus	85	0.018	4.46	33	0.6	0.17
Gadus merlangus	51	0.03	3.18	21	0.6	0.2
Onos mustela	20	0.023	2.39	26	0.45	0.15
	80	0.03	4.66	20	0.55	0.27
Crenilabrus melops	65	0.04	2.96	21	0.85	0.3
Salmo trutta sp.	175	0.023	5.44	21	0.7	0.2
Tinca tinca	140	0.025	8	25	0.86	0.1
Chaenocephalus sp.	750	0.053	11.96	12	1.6	0.5
	790	0.057	9.84	12	1.5	0.55
Lophius piscatorius	1550	0.07	13.31	11	1.1	0.4
Plmronectes platessa	86	0.04	5.08	20	0.75	0.2
Zeus faber	300	0.04	4.97	15	1.1	0.11
Trigla gurnardus	18	0.02	1.84	22	0.35	0.06
Cottus bubalis	40	0.04	2.86	16	0.8	0.3
	52	0.04	3	16	0.8	0.25
Callionymus lyra	64	0.05	2.86	15	0.8	0.3
	46	0.03	2.56	16	0.7	0.25
	24	0.047	1.77	17	0.6	0.15

1) Thickness_mem/width_water - the ratio width of epithelium and water channels (H2/H1)

2) Width_bld/width_water - the ratio width of blood and water channels (H3/H1)

3) Blood_parameter - the ratio of the diffusivity and speed in the blood layer (D3xL)/ ($V3xH3^2$)

4) Water_parameter - the ratio of the diffusivity and speed in the water layer (D1xL)/ ($V1xH1^2$).

For the purpose of calculation of these dimensionless parameters for different fishes, following assumptions were made.

1) The diameter of a single microcapillary is considered as the maximum width of blood channel spanning across the width of the secondary lamella.
2) The flow calculations were done assuming the rectangular cross-section of interlamellar space and secondary lamella.
3) The tortuosity and branching of blood channel and its diameter variation along the length are neglected for simplifying the model.
4) The enzymatic reaction based capture of oxygen by hemoglobin in the blood was neglected and only diffusion was considered.

3.2.2. Results and discussion

In order to explore the role of primary and secondary lamellae, we analyzed the variation of the length of primary and secondary lamella with respect to fish's body masses. We observed that length of secondary lamellae and primary lamellae followed a logarithmic relation with fish body weight (Figure 3.1). However, the length dependence of primary lamellae on a fish body mass was more pronounced as compared to secondary lamella. This might be primarily because secondary lamella being a site of solute/gas exchange, its length is guided by diffusion length of solute/gas during a convective flow. Due to evolutionary conservation of the interlamellar distance across different weight of fishes[87], the time scale of diffusion of gases/solutes across the inter-lamellar space should be less than the residence time of water flowing in the interlamellar channel defined by the ratio of the length of the secondary lamella and the velocity of water passing through it. However, the difference between the convective and diffusive time scales should not be too high, leading to an unnecessary increase in the length of the secondary lamella. Thus, the residence time of water during a convective flow should be marginally higher than diffusion time scale.

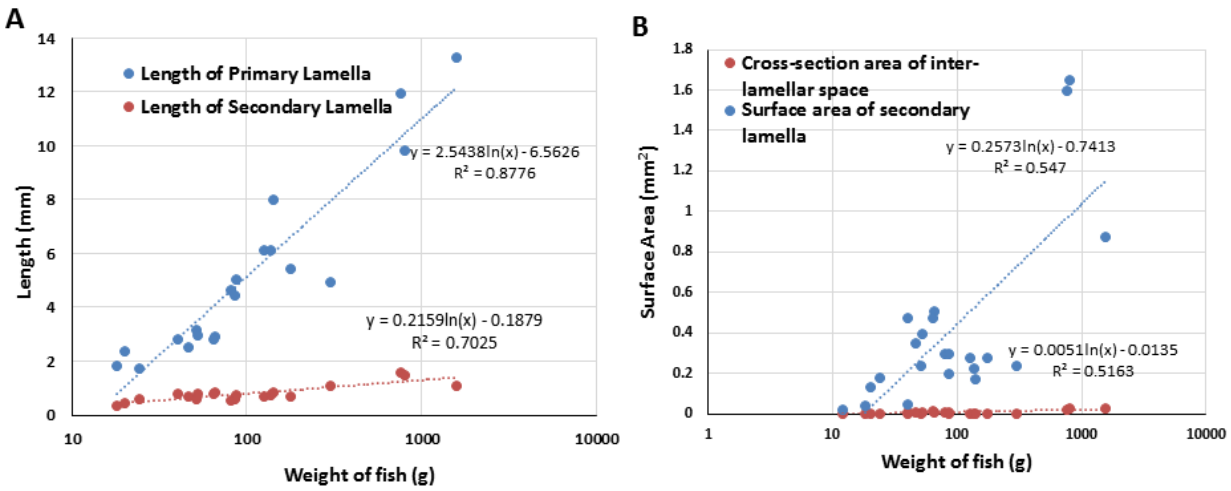

Figure 3.1 Graph showing the variation of A) length of primary and secondary lamella with the weight of fishes on logarithmic scale B) surface area of secondary lamellae and the cross-section area of inter-lamellar space with the weight of fishes on a logarithmic scale.

Moreover, considering the pressure drop across the length is confined by pumping capacity of fishes, the variation in the flow velocity of water in inter-lamellar space will within a narrow range. Therefore, length should be just sufficient enough to enable ratio of residence time to diffusion time scale to be equal or greater than 1. Thus, we observed that the length of secondary lamella showed a weak dependence on the weight of fishes. However, the primary lamella being a structural element, which acts as a rack for parallel stacking of secondary lamellae, demonstrates a strong dependence on the weight of the fishes. This may be to maximize the number of accommodating secondary lamella which is the functional unit of fish gills. The increase in the number of secondary lamellae eventually increases the surface area available for gas/solute exchange. The surface area of fish gills scales linearly with the weight of fishes. Thus, the length of the primary lamella demonstrates strong dependence on the weight of fishes (Figure 3.1A). These factors suggest primary lamellae a vital structure for gas/solute exchange in fishes, although they are only a structural element of fish gills. Moreover, an increase in the mass of fishes is related to their energy requirements which can be fulfilled by a proportionate increase in the surface area of fish gills. Therefore, we observed that both the surface area of gills which participates in mass transfer and volume of fluid flowing through interlamellar spaces which carry the gases/solutes increases with an increase in fish body mass. Therefore, the arrangement of

primary and secondary lamellae may play a vital role in a fish body with different body masses.

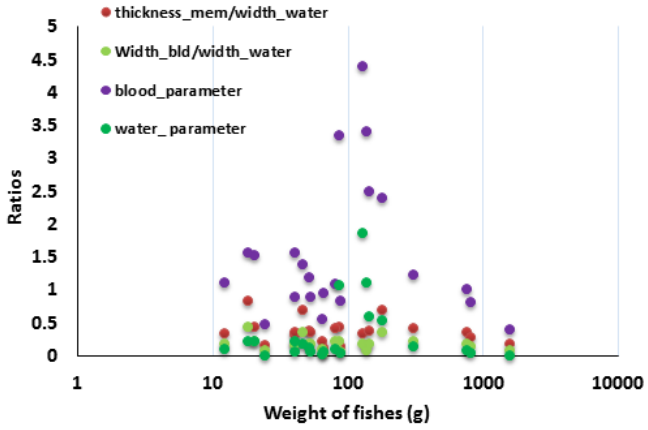

Figure 3.2 Graph showing the variation of different dimensionless quantities (Parametric ratios) with the weight of fishes on a logarithmic scale.

Although the spatial arrangement of primary and secondary lamella defines the architecture of gills and forms a basis for design and fabrication of compact biomimetic fish gill structures, they hardly gave any idea about the different correlated factors affecting the solute/gas exchange process at the site of the secondary lamella. To develop fundamental insights into mass transport phenomena in devices with dimensions spanning multiple scales like fish gills, we have considered a simple device design (Figure 3.3) with nominal dimensions based on an ease of modeling the gas/solute exchange phenomena and fabrication of the device. Further, considering the multiple parameters of fish gills affecting the mass transfer, it is challenging to borrow dimensions from a fish to develop mass transfer device as per our requirement when the above parameter are closely coupled with other parameters. Therefore, having a few dimensionless parameters and knowing their degree of significance in mass transfer will assist in easy and efficient design of user defined size of mass transfer devices. Furthermore, non-dimensional parameters (the parametric ratios) are defined to scale the proposed analysis for biomimicking an actual fish gill. This will generate underatanding the concept of mass transfer in fish gills independent of the size of fishes. Therefore, for gills of 22 different fishes were evaluated from their morphometric properties and compared. All the parametric ratios plotted against the weight of fishes on a logarithmic

scale. It was observed that these parametric ratios remain nearly conserved in all 22 fishes taken for evaluation, although their body mass varied from 12g to 1550g as shown in Figure 3.2. The thickness of the membrane to water channel width ratio should be as small as possible to minimize the diffusion barrier length for solute/gases. The calculated data indeed suggested that this ratio for 22 different fishes lied in the range of 0.135 to 0.848 with an average of 0.372 ± 0.189, much less than 1. Further, the width of blood channel should neither be too less leading to high blood pumping pressure due to an increased blood flow resistance nor too high to leading to the condition of washout without proper oxygenation. Therefore, the ratio of the width of blood channel to water channel lied between 0.071 and 0.449 with the mean of 0.206 ± 0.095 in all 22 fishes.

Further, the blood and water parametric ratio define the oxygenation and deoxygenation of blood and water stream, respectively. During oxygen exchange in gills, the convective flow in blood and water stream and diffusion across the three barriers (blood water and thin epithelial layer) play a vital role. Under steady state condition, the diffusion time scale in the water stream is much greater than diffusion time scale in the blood stream and epithelial layer. Therefore, the time scale of convective flow in blood and water stream are normalized by the time scale of diffusion in the water stream to obtain the blood and water parametric ratios, respectively. The blood parametric ratio existed between 0.535 and 5.778 with mean value 2.11±1.41. The mean value being above 1 indicated that the time of convective flow is greater than the time taken for diffusion of chemical species normal to the direction of flow. Such behavior leads to the complete oxygenation of blood before de-oxygenated blood leaves the blood stream. The kinetics of capture of oxygen by hemoglobin of red blood cells defines the depletion rate oxygen in the blood stream. Further, it has been also established that diffusivity of oxygen in the blood is dependent on the concentration of hemoglobin in the blood. Thus, the delayed time of stay of deoxygenated hemoglobin in the blood stream due to convective flow of blood enables the capture and creation of oxygen deficiency in the bloodstream, thereby maintaining a continuous concentration gradient between the blood and the water stream. Moreover, the factors like variation in concentration of hemoglobin in the blood of different fishes affect the diffusion coefficient of oxygen, changes blood pumping rate of fishes, differences in effective path length of blood stream due to tortuous nature of vasculature affect the blood parametric ratio. Therefore, there is

substantial variation in blood parametric ratios obtained in 22 fishes. Thus, blood parametric ratio will help in defining the critical blood velocity in blood channel which maximizes the time scale of convection in comparison to the time scale of diffusion of oxygen in the water stream. When water parametric ratio was considered, it was found that this parameter in different fishes lies between 0.016 and 1.88 with the mean of 0.323 ± 0.459. This clearly illustrates that the time scale of diffusion exceeds the time scale of convection transport in the water channel. Such behavior is not desirable for fishes because it indicates that certain percentage oxygen from given volume of water flushes out of water stream through convection before complete oxygen diffuses out of water stream and enters the bloodstream. However, fishes tackle this problem by reducing the interlamellar distance through pillar cells. This is the mechanism to reduce the diffusion time scale and maximize the oxygen exchange. Therefore, fishes execute this behavior when the oxygen partial pressure is low in the ambient water. Moreover, the volume of water flowing through inter-lamellar space is much higher than blood flowing through secondary lamella. The amount of oxygen needed for complete oxygenation of blood would be less than the total amount of oxygen flowing through interlamellar space. Despite, the water parametric ratios obtained for 22 fishes being less than 1, its value may be sufficient to oxygenate the blood stream flowing in a counter current direction. Inter- lamellar distances are calculated based on anatomical dissection studies of fishes which might be different when fishes are swimming in water. Further, assumptions of the rectangular cross-section of interlamellar space and constant pressure gradient provided by a buccal activity of fishes were used to calculate the velocity. Therefore, the mean value of water parametric ratio obtained is below 1 which might not be the actual case. The value of water parametric ratio near to 1 is desirable for maximum oxygen exchange in gills.

From the figure, it was observed that the data of different parametric ratios for different fishes showed minimum variation as compared to the weight of fishes. The majority of ratios lie within the window of 1±1. The value of these parametric ratios does not vary much with the weight of fishes indicating their evolutionary conservation in fishes to maximize its efficiency of gas/solute exchange. Further, the architectural design of primary and secondary lamella is also conserved across different fishes to aid in enhancing mass transport. Therefore, the above parametric ratios and arrangement of primary and secondary

lamella can be used as engineering design parameters to develop micro/nanodevices for gas and solute exchange applications. However, these data do not speak about the nature of variation of different parametric ratios with the efficiency of gas/solute exchange. Therefore, we have studied the gas exchange in a secondary lamella during convective–diffusion phenomena to evaluate the nature of these parametric ratios through computational method.

3.3. Computational study

3.3.1. Study the convective- diffusion phenomenon in fish gills

To model and simulate the convection-diffusion phenomenon in secondary lamellae (Figure 3.3A), we have studied the phenomenon on a two-dimensional model of a secondary lamella as shown in Figure 3.3B. We have made certain assumptions while simulating the diffusion phenomenon in secondary lamella. These assumptions are

1) A two-dimensional model of gas exchange in a single secondary lamella is considered
2) Blood channel represents the blood vessel inside the tissue matrix of secondary lamella
3) The gray colored domain between blood channel and water channel represents the thin epithelial matrix, a barrier separating blood and water.
4) Steady state convective-diffusion phenomenon is solved in above model
5) The blood and water flow velocity is assumed to be average velocity rather than a velocity with a parabolic profile and flowing in counter-current direction
6) Diffusion of oxygen is considered from water channel to blood channel by crossing thin epithelial matrix.

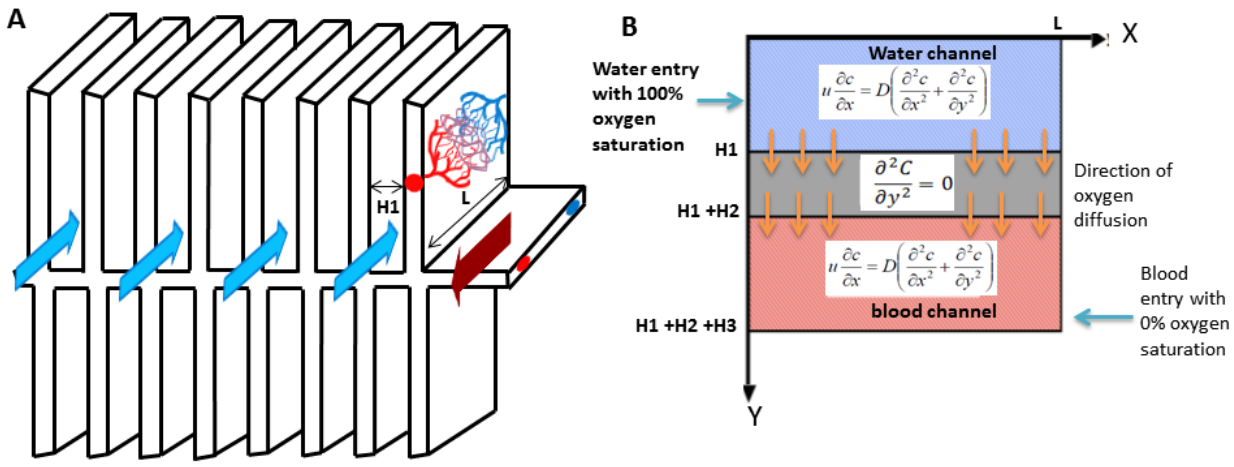

Figure 3.3 A) A schematic of secondary lamellae stacked in parallel on primary lamella. The blue arrow indicates the direction of water and red arrow represents direction of blood B) A 2D model of secondary lamella used in computational simulation

Under above assumptions convective-diffusion phenomenon was modeled in COMSOL Multiphysics 4.3b. The governing equations in each domain are

$$U_w \frac{\partial C}{\partial x} = D_w\left(\frac{\partial^2 C}{\partial x^2} + \frac{\partial^2 C}{\partial y^2}\right)\ldots\ldots \text{(Water domain)} \quad (3.1)$$

$$U_b \frac{\partial C}{\partial x} = D_b\left(\frac{\partial^2 C}{\partial x^2} + \frac{\partial^2 C}{\partial y^2}\right)\ldots\ldots \text{(Blood domain)} \quad (3.2)$$

$$D_e \frac{\partial^2 C}{\partial y^2} = 0\ldots\ldots \text{(Epithelial barrier)} \quad (3.3)$$

$$N = -D\frac{\partial C}{\partial x} + U_x C \quad (3.4)$$

Where, U_w is average velocity in water channel, U_b is average velocity in blood domain, D_w is the diffusion coefficient of oxygen in water, D_b is the diffusion coefficient of oxygen in Blood, D_e is the diffusion coefficient of oxygen in epithelial matrix, C is the concentration of oxygen and N is the flux

Initial conditions : C (x,y) = 0

Boundary condition: inlet at water channel → $C = C_o$

Outlet at water channel → $n.N = 0$

Inlet at blood channel → C = 0

Outlet at Blood channel → n.N = 0

Table 3.2 Parameters used for modelling of convective diffusion phenomenon in secondary lamella

Parameters	**Value**	**Parameters**	**Value**
Width of water channel	35µm	Diffusion coefficient of oxygen in Blood	2.18e-9m^2/sec
Width of blood channel	8.8µm	Diffusion coefficient of oxygen in water	3.4e-9m^2/sec
Thickness of epithelial layer	2.8µm	Diffusion coefficient of oxygen in epithelial layer	1.1e-9m^2/sec
Length of channels	760µm	Density and viscosity of water	1000kg/m^3 0.001kg/ms
Avg. velocity of water	0.014m/s	Density and viscosity of blood	1050kg/m^3 0.0035/kg/ms
Avg. velocity of blood	0.0005m/s	Conc. Of Oxygen in water stream	0.25moles/m^3

Thereafter, considering the initial and boundary condition with the values of parameters in Table 3.2, [32, 90, 91] we have studied the concentration of oxygen at the exit of blood channel by varying the different parametric ratios under steady state condition.

The concentration profile results of oxygen in different layers a) water channel b) thin epithelial layer and c) blood channel was shown in Figure 3.4A. From the concentration profile, it was evident that there always exist a concentration gradient at an entry of blood channel and exit of a water channel, even after infinite time, providing a continuous diffusion of oxygen from water channel to blood channel via a thin epithelial barrier. Further, when oxygen concentration at an exit of blood stream was evaluated against each parametric ratio defined previously, each parameter plays a distinctive role in oxygen concentration flux at the exit of blood channel (Figure 3.4B). It was observed that thickness of epithelial barrier should be as thin as possible as compared to the water channel to maximize the exchange of

gas across the epithelial barrier. Moreover, the width of the blood channel also needs to be small as compared to water channel. The oxygen concentration at the exit of blood channel decreases rapidly with increase in the ratios of the width of the thin epithelial membrane to the width of the water channel and width of the blood channel to the width of the water channel, respectively (Figure 3.4B). However, the width of the blood channel need to be of an optimal size to avoid high pumping pressure to overcome increased blood flow resistance and assist in maximum diffusion of oxygen in the blood stream before oxygenated blood comes out of blood channel.

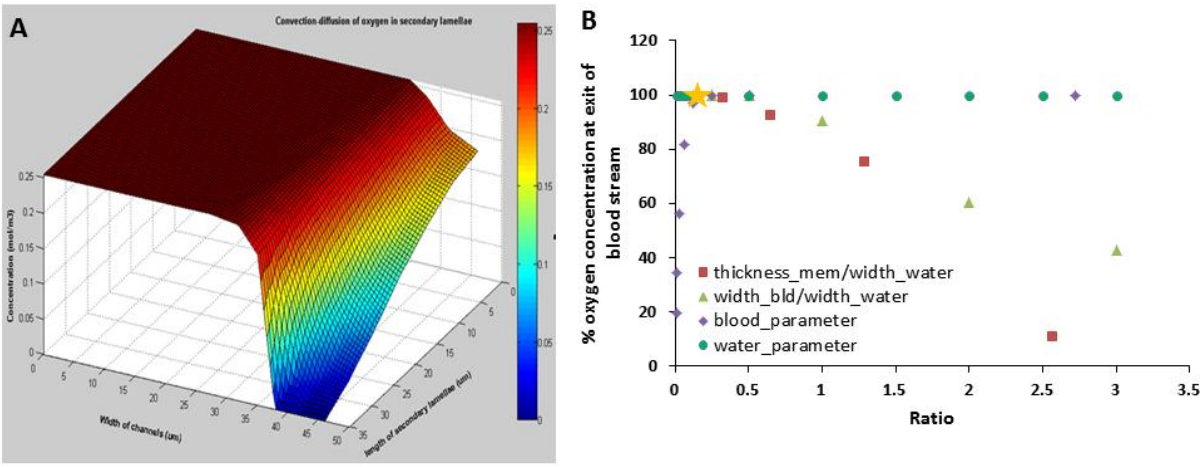

Figure 3.4 A) Graph showing the effect of different dimensionaless parameters (ratios) on % of oxygen concentration at an exit of blood channel a) Concentration profile of oxygen in different in blood and water channels.

Further, the blood parametric ratio suggests that above a critical ratio of 0.32, the effect of the increase in ratio hardly affect the oxygen concentration at the exit of blood channel. Below the critical ratio, the diffusion phenomenon dominates the convection phenomena, leading to falling in concentration gradient driving the diffusion process. This results in low oxygen concentration in the blood stream at the exit of blood channel. However, at a higher ratio, blood saturated with oxygen washes out of secondary lamella, thereby continually maintaining the concentration gradient driving the diffusion process. This suggests that higher ratios are preferable for better gas exchange. The water parametric ratio has a negligible effect on the oxygenation of blood within the range of ratios considered in the study. However, at a much higher ratio, the decrease in concentration of oxygen in blood

clearly indicated the case of washout. It was observed that all the curves pertaining to different parametric ratios intersect at the ratio of 0.32. This ratio marks the optimal ratio of different parameters to enable the maximum exchange of gas from the water stream to the blood stream and is shown as a yellow star in the Figure 3.4B.

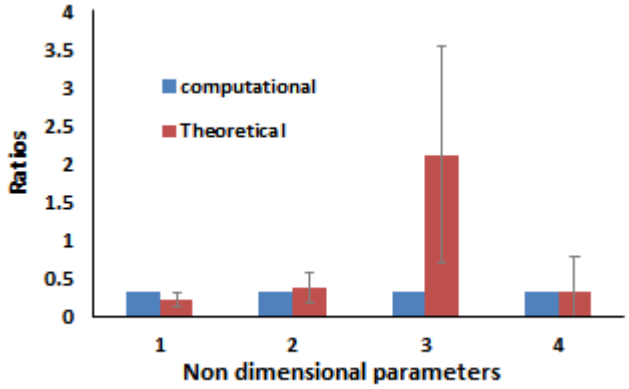

Figure 3.5 Graph showing the comparison of parametric ratios evaluated from computational method and theoretical analysis from data available in literature

On comparison of results obtained from the theoretical and computational model, it was found that overall results show good agreement with each other (Figure 3.5). Although, the three parametric ratios (ratio of thickness of membrane to width of water channel, ratio of width of blood channel to the width of water channel and water parametric ratios) predicted by computational model is in congruence with theoretical results as shown in figure, the blood parametric ratio calculated through computational model demonstrated significant difference from the theoretical results. This might be due to fixed velocity and rectangular cross section straight blood channel assumed in the theoretical analysis for all the fishes. The velocity of blood in the secondary lamella of fish varies with species of fishes, an activity of fishes in water medium in which they thrive. Therefore, fishes manipulate the blood flow velocity in accordance with the width of interlamellar space to maximize the sustained diffusion of oxygen from water to blood of fishes. Further, the vascular channels are tortuous in nature with varying circular cross-section in different fishes.

3.3.2. Study the role of vascularization density and thickness of polymer membrane on mass transfer

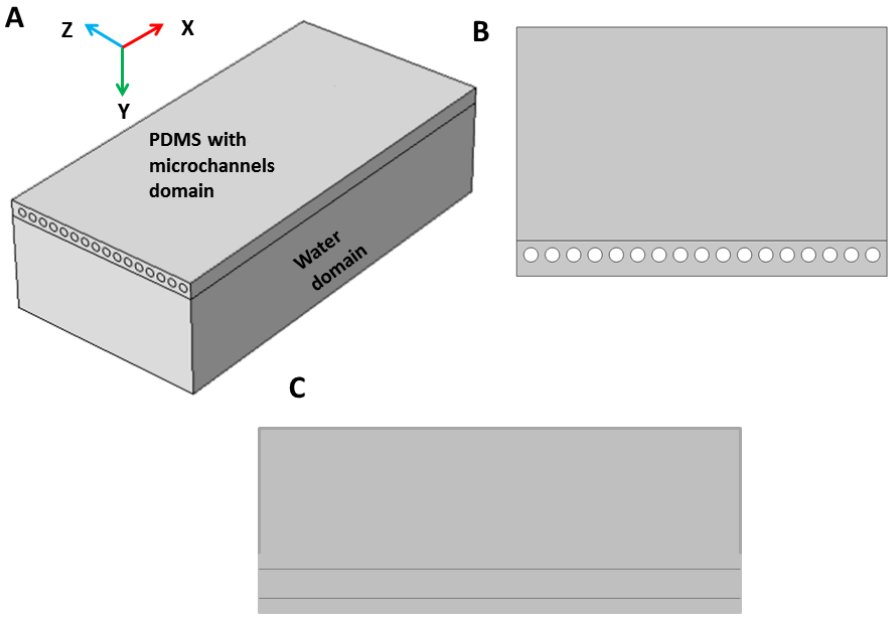

Figure 3.6 A) 3D model of secondary lamella with inter-lamellar space represented by microchannel network in PDMS thin matrix having water domain on one side B) 2D model of secondary lamella by taking a slice of proposed 3D model by YZ plane C) 2D model of secondary lamella by taking a slice of proposed 3D model by XY plane

In secondary lamella of fishes, the water domain is the gap between two secondary lamellae where water flow in a counter-current direction. This arrangement enables the diffusion of oxygen from flowing water to blood vessels and carbon dioxide, ammonia, urea and other solutes from blood vessels to the outside water via an epithelial barrier. Therefore, the model described in the Figure 3.6A is a 3-dimensional model of secondary lamella represented by vascularized network within a thin cuboidal block and inter-lamellar space by a cuboidal block of water domain. While studying the diffusion phenomenon of solute (urea) from secondary lamella to water domain, we have assumed a two-dimensional simplified model as shown in the Figure 3.6B (cross-section of above 3D proposed model in YZ plane). Thereafter, steady state diffusion phenomenon in the two-dimensional model is solved. The model assumes that velocity in Y direction is zero. Further, in the second model, the two-dimensional model is obtained by slicing the proposed 3D model by XY plane (Figure 3.6C). Thus, it enables the study of diffusion of urea normal to the flow direction. During the

convective flow, the urea-laden water and water devoid of urea is present in microchannel and water domain, respectively. Further, using the following equations and boundary conditions, we have modeled and solved the diffusion and advection problem in COMSOL Multiphysics 4.3b.

$$u\nabla C = D\nabla^2 C \tag{3.5}$$

$$N = -D\nabla C + uC \tag{3.6}$$

Initial conditions (ICs) $C(x, y) = 0$

Boundary conditions (BCs) at inlet $C(x, y) = Co$

at outlet $-n.N = 0$

At boundary $C(x, y, z = \infty) = 0$

Where, U_w is average velocity in water channel, U_b is average velocity in blood domain, D_w is the diffusion coefficient of urea in water, D_b is the diffusion coefficient of urea in Blood, D_e is the diffusion coefficient of urea in PDMS matrix, C is the concentration of oxygen and N is the flux. The parameters used for modeling and solving the problem described above are enumerated in a Table 3.3.

Table 3.3 Parameter used for modelling of diffusion phenomenon in secondary lamella model

Parameters	**Value**
Width of water and PDMS channel	52 micron
Height of blood channel	10 micron
Height of PDMS layer	Varied from 0.5 - 20 micron
Diameter of channels	2 micron
Diffusivity of urea in water	1.7e-9m^2/sec
Diffusivity of urea in PDMS	0.3e-9m^2/sec
Velocity of water with urea solute	Varied from (1 -10^5) micron/sec

The concentration profile of urea in water domain is shown in the Figure 3.7A. The concentration of urea reduces while moving away from the microchannels. Therefore, to estimate concentration in the water domain, the average of concentration along the width of water domain at fixed distance from the boundary of PDMS matrix was obtained.

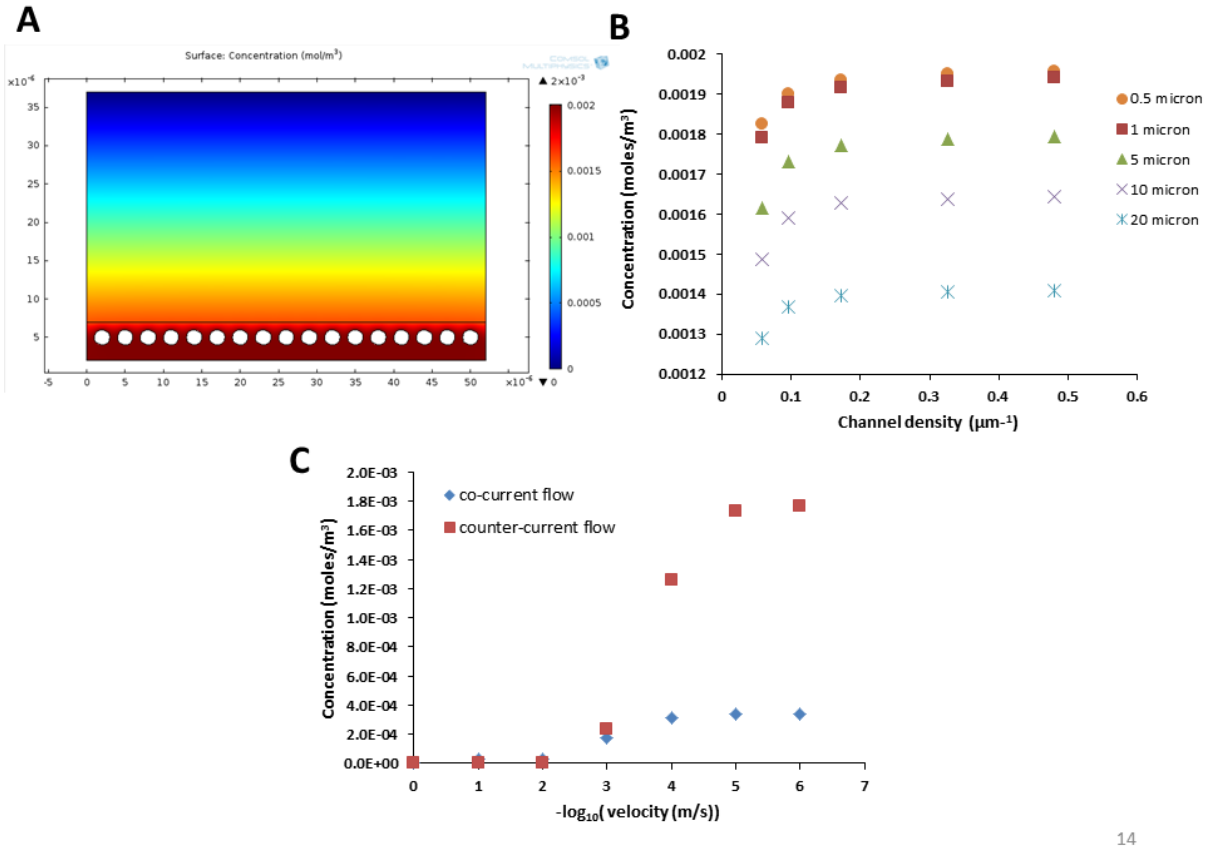

Figure 3.7 A) Concentration profile of urea in water and polymer matrix domain, respectively B) Graph showing the variation of urea concentration in water domain at different channel density and thickness of separating membrane C) Graph showing the variation of urea concentration with flow direction in microchannel and water domain.

Modeling and simulation of steady state urea diffusion through microvascularised PDMS matrix suggested the dependence of urea diffusion on the density of microchannels and thickness of PDMS membrane. The concentration profile of urea in water and microchannel domain is shown in Figure 3.7A. It has been observed that with an increasing density of channels, there is an increase in the diffusion of solute. However, at a higher channel density, the curve plateau indicating at channel density of 0.2 um^{-1}, further increase

in channel density hardly affects the diffusion of solute as shown in Figure 3.7B. Thus there exists an optimal density of vascularization for maximum diffusion without incurring much on the cost of fabrication. Further, diffusion follows an exponential decline with an increase in thickness of diffusion membrane barrier as observed in Figure 3.7B. Our further simulation on the diffusion dependence on the flow of fluid through microchannels showed that diffusion increases with an increase in velocity and thereafter the curve gets plateaued, showing an existence of optimal velocity for maximization of diffusion flux. Further simulation with optimum velocity in the nanochannels and flow in water channel in counter-current and co-current respectively were carried out. It was observed in Figure 3.7C that saturation of water occurs at a lower concentration in co-current flow as compared to counter-current flow at a given flow velocity in the nanochannel. As above study would be difficult to conduct experimentally, therefore, we have computationally studied secondary lamella through 2D models mimicking secondary lamella

3.4. Conclusion

Fish gills are one of the excellent gas/solute exchange structures available in nature. Such performances are attributed to their extraordinary multiscale hierarchical structures. Therefore, bio-mimicking these structures at different length scale to form a gas/solute exchange device require detailed study of their structural properties and how they guide the transport properties in fish gills. Further, there is also a need to formulate few dimensionless parameters which can be used as design parameters for development of gas/solute separation device. Hence, we have established four parametric ratios which affect the convection-diffusion phenomenon in fishes and studied their role in gas exchange through modeling and simulation. It was observed that these parametric ratios tend to have an optimal value around 0.33 for the maximization of gas exchange across secondary lamella. Further, our theoretical analysis on 22 different fishes supported our argument about very limited variability of above parametric ratios with the weight of fishes. Thus, structural design of biomimetic gas/solute exchange devices should incorporate these parametric ratios as a design parameter. Apart from these parametric ratios, the role of the factors like vasculature density in thin secondary lamella, dimensions of the primary and secondary lamella, the surface area of fish gills and interlamellar distance have been studied in detail. These studies can form a backbone for the

biomimetic development of devices for gas/solute exchange. Therefore, we have decided to mimic the functional unit of fish gills- secondary lamella through vascularization of polymers and study the parameters which affect the fluid flow and mass transfer capabilities of these polymer systems.

4. Chapter 4
3D Micro/nanofluidic Devices

4.1. Introduction

The microstructure of secondary lamella of fish gills, described in the previous chapter, play a vital role in gas/solute separation in fishes. A thin secondary lamella can be engineered by the mimicking of the functionality of large aspect ratio blood vessels which efficiently irrigate fish gills, also known as vasculature, by generating a channel network in thin polymer matrices. The channel dimensions in a vascular network falling in the range of micro/nano length scales qualifies these thin vascularised polymer matrices to be used in three-dimensional micro/nanofluidic devices. These three-dimensional micro/nanofluidic architectures in polymers having applications in the fields such as tissue engineering, drug delivery, as a matrix for cell growth and as self- healing structures is growing steadily. This enables the utilisation of the many benefits that arise from enhanced connectivity, larger surface area and better nutrient transport capability, which are rather limited in more established two-dimensional micro/nanofluidic devices[92-95]. However, these applications can be realised when the diffusional limitations of small molecules such as gases, solutes and other are overcome in three-dimensional micro/nanofluidic devices[96].

Synthetic methods of creating vascularised (a network of micro/nanochannels) polymers can be realised by either impregnating host polymers with the sacrificial material and by their removal by thermal and chemical methods[75, 76, 97, 98] or by imposing very high electric discharge through the polymers[38]. A large variety of materials, both host and sacrificial, have been explored by these methods, and they offer advantages such as affordability, scalability and low-cost of equipment. The diameters of channels in these studies were typically larger than 20µm, which facilitated the flow of fluid under pressure-flow conditions without high hydraulic resistances. However, the majority of methods lacked the ability to fabricate 3D, monolithic nanofluidic devices in which the network dimensions can be tailored at ease. Therefore, an alternative method that is convenient and scalable needs to be explored for the design and fabrication of 3D nanofluidic devices.

Therefore, to fabricate 3D nanofluidic networks in polymer matrices, electrospun nanofibre meshes as sacrificial materials have been explored by several researchers. For example, Bellan L M *et al.* fabricated a random nanochannel network in polydimethylsiloxane (PDMS) substrate using sacrificial electrospun polyethylene oxide nanofibres as an inverse

replica[99]. Gaulundi *et al.* explored electrospun polyvinyl alcohol for the fabrication of 3D vascularised polymer matrices. Fluid flow in these vascularised networks can be driven by capillary action. The former work utilized rectangular reservoirs to interface with the vascularised polymer, while in the later work the vascularised polymers were submerged in a liquid to enable capillary filling [100]. Subsequently Bellan *et al.* connected the vascularised polymer matrix with an external tubing to create viable micro/nanofluidic devices[75, 101]. Although these articles have convincingly articulated different methods to drive fluids through vascularised networks, the connection of the vascularised polymer to an external fluidic circuit in order to take advantage of their enhanced surface-to-volume ratio and interconnectivity has been least explored. The methods utilized to address this issue are far from being optimal because a large number of channels that comprise the vasculature will not be in direct contact with the reservoir, thus limiting the interface. As a result, the volumetric flow rate in the vascularised polymer matrix will decrease and will be substantially lower than that which is possible. This is further compounded by the enhanced hydraulic resistance when the dimensions of the channels in the vasculature become smaller. For the applications that are typically envisaged for vascularised matrices, mass transfer and reaction rates play a critical role[102]; these properties will scale directly with the volumetric flow rates. Therefore, there is a need to investigate (from a fundamental and applied point of view) how one can modify the shape and size of the reservoirs to interface efficiently with the vascularised polymers in order to provide a facile connection with the external fluidic port without compromising the compactness of the devices. Further, a theoretical investigation on the effect of density and tortuosity of microchannel network on the capillary wicking has been performed by Jianchao Cai *et al*. They demonstrated that the volumetric flow rate scales linearly with channel density while it varies as the square of the inverse of tortuosity[103]. Although volumetric flow scales linearly with the density of channel network, it has been known that an increase in the density of vascularization does not support a continuous increase in mass transfer capabilities[25, 89]. Such observation of cessation of mass transfer through optimally vascularized polymer matrices is also reported in Chapter 3. Thus, optimal channel density will facilitate mass transfer rate without compromising the mechanical properties of the vascularized polymers or subjecting additional burden on the use of material

during a manufacturing process. Therefore, channel density and tortuosity also need to be investigated for volumetric flow and mass transfer through vascularized polymers.

Therefore, we hypothesize that a reservoir with branch-shaped vessels interfacing with an optimally vascularised polymer will demonstrate enhanced volumetric flow and mass transfer than a rectangular reservoir.

In this chapter, the following research objectives are achieved

1) Theoretical and experimental investigation on the role of the geometry of reservoirs, which interfaces between the external fluidic port and the vascularised polymer matrices.
2) Design, fabrication and structural characterization of thin vascularised polymer matrices by using sacrificial electrospun fibres in host PDMS matrices
3) Volumetric fluid flow and mass transfer rate quantification through vascularised polymer matrices having a different geometry of reservoir which interfaces with vascular network and density and tortuosity of the vascular channel network.

Our study will lead to design and fabrication of more efficient 3D micro/nanofluidic devices that can be used in advanced applications such as organ-on-chips, lab-on-chips, tissue engineering, and cell culture studies in complex environments. We hope to achieve this efficiency by providing a better method for interfacing and connecting with external fluidic circuits and optimizing the channel density and tortuosity.

4.2. Theoretical modeling

In this section, we have theoretically analysed the parameters that govern the geometry of a reservoir that is bounded by a fixed size and shape of a virtual boundary, and its integration with a vascularised polymer matrix in a microdevice. Figure 4.1A shows the reservoirs that are connected to a vascular network, which is represented by grey curves in a device (shown by an orange boundary).

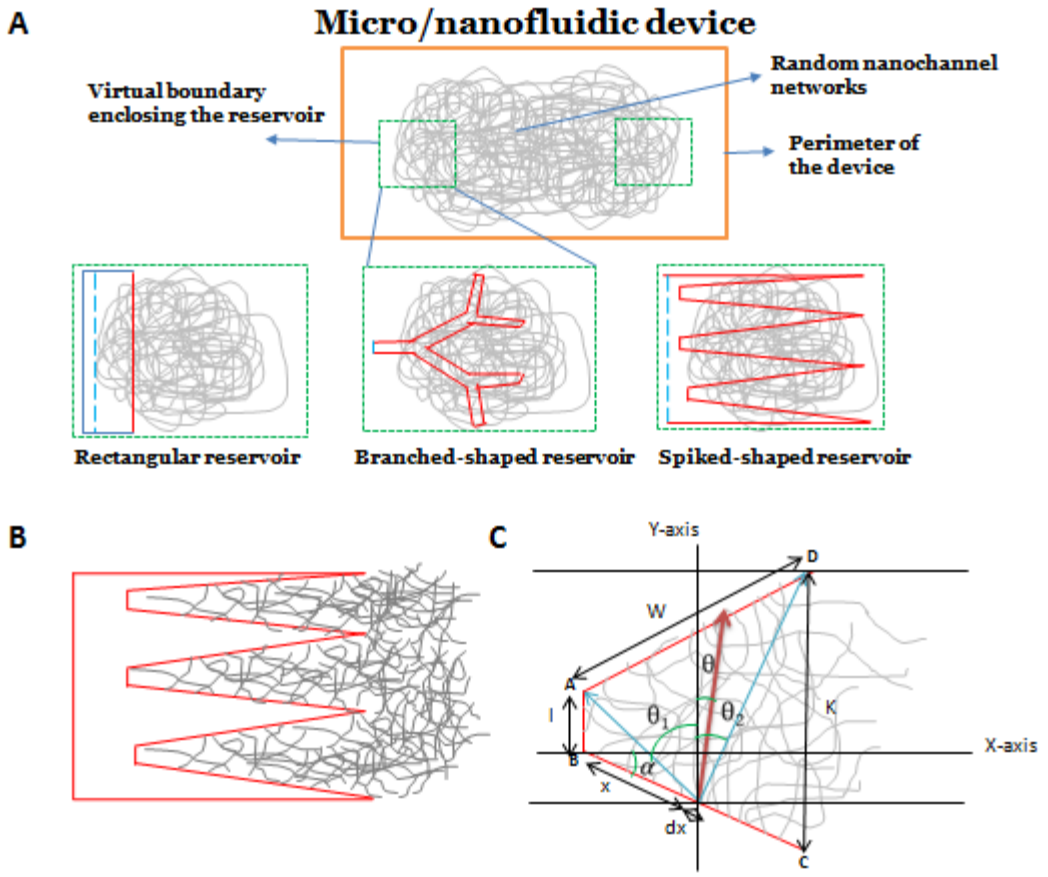

Figure 4.1 A) Schematic of different shapes of a reservoir (red colour) connected to a random network of nanochannels (grey colour) in a device (orange colour). The dashed green colour represent virtual boundary in the micro-device enclosing the reservoirs while dashed blue line represents the length of reservoir's segment initially facing fluid front (not interfacing with nanochannel network) after delivery of fluid in the reservoir. The red segment of reservoir represents nanochannel interfacing length of the reservoir B) Schematic of the spiked-shaped reservoir connected to nano-channel networks C) schematic of the gap between the spikes of a spike-shaped reservoir where the random network of channels (grey colour) connected to reservoir wall (red colour). θ1 and θ_2 are the maximum angle spanned by a fiber originating at the line BC in an element dx and joining the line AD. The W is the non-parallel width and l & K is the two parallel lengths of the trapezoid ABCD respectively. α is the angle subtended side AD or BC makes with the x-axis.

In addition, in Figure 4.1A, the dashed green bounding box represents the virtual boundary of the reservoirs; the red segment of the reservoir inside a virtual boundary

represents the interfacing segment of the reservoirs with a vascular network; and the dashed blue line represents the non-interfacing segment of reservoirs. Figure 4.1B illustrates the connection between the spike-shaped reservoir and the random channels, in which the area between the spikes, as shown in Figure 4.1C, was used to estimate the number of free connections of the vascular network with the reservoir. θ_1 and θ_2 are the maximum angles that are spanned by a channel that originates at a line, BC, in an element, dx, and joins line, AD. W is the nonparallel width, and l and K are the two parallel lengths of the trapezoid ABCD, respectively. Angle α is the angle that sides AD or BC make with the x-axis (Figure 4.1C) The generalised mathematical model[104] was developed with the parameters that are illustrated in Figure 4.1C. The model makes certain assumptions:

1) A high random isotropic network of tortuous channels, in which the probability of finding a channel in a region follows a normal distribution.
2) The channels are long enough to make connections with either end of the reservoir, and their diameter is 1µm, which distributed uniformly throughout the matrix.
3) The length (l) is considered to be very small in comparison to the length (K) in the spike and the branched reservoir for geometry optimisation (Figure 4.1C).
4) Branched geometry is considered as a hierarchical spiked geometry.
5) For the sake of a reasonable comparison, the area of the dashed green bounding box (size of virtual boundary encasing the reservoirs) is kept constant at $100mm^2$ for all types of reservoirs, and the maximum possible size of the rectangular, branched and spiked reservoirs were created within the virtual boundary (dashed green boundary) that has hydraulic diameters of 1mm, 0.8mm, and 4.37mm, respectively.

In addition to the above, if we have a line or curve intersecting the vascular network, then the number of channels intersected per unit length is considered to be N_o. Under these assumptions, in a probabilistic framework, we develop a number of 'free connections' in the channels to the reservoir. By free connections, we mean those connections in which only either ends of a channel are connected to a reservoir. Connections in which both the ends of a channel interface with the same reservoir are not useful from an application perspective and are termed as 'cross-connections' here. These connections do not enhance the fluid transport

from a source to a sink reservoir. Therefore, the number of channels that originate and terminate in the same reservoir is given by

$$N = N_o \int_0^W f(x)dx\,. \tag{4.1}$$

The f(x) is the probability of finding a channel that originates between *x* and *x+dx* on line BC and terminates on line AD (see Figure 4.1C) and has a cord angle between $-\left(\frac{\pi}{2}-\alpha\right)\leq$ $\leq \tan^{-1}\left(\frac{\frac{(W-x)a}{l+K}}{2}-(-xb)\right)$. The cord angle (θ) can range between $\left(\frac{\pi}{2}+\alpha\right)$ and - $\left(\frac{\pi}{2}-\alpha\right)$ for any channel. Therefore, f(x) is given by the following equation:

$$f(x) = \frac{\int_{-(\frac{\pi}{2}-\alpha)}^{\tan^{-1}\left(\frac{\frac{(W-x)a}{l+K}}{2}-(-xb)\right)} p(x)\,d\theta}{\int_{-(\frac{\pi}{2}-\alpha)}^{\frac{\pi}{2}+\alpha} p(x)\,d\theta}\,, \tag{4.2}$$

where w is the width, l and k are the lengths of the two parallel sides of a trapezoid, α is half the angle between the spikes, 'a' is the cosine of the angle (α) and 'b' is the sin of the angle (α), as shown in Figure 4.1C. The probability density function of the random channels is taken to be a constant and is given by the following rectangular function:

$$p(x) = \{0\ for\ x\ \geq W, c\ for\ 0 \leq x \leq W\} \tag{4.3}$$

By solving equation 1 analytically after plugging equation 4.2 and 4.3 in 4.1, we determined the number of cross-connected channels of the trapezoid (ABCD), as shown in Figure 4.1C. Therefore, the number of channels (N) with cross-connections can be given by equation (1). By considering the symmetry of the spikes throughout the reservoir area, the total numbers of cross-connections were estimated. Thus, the number of free connections (N_f) is the difference between the total number of connections and the number of cross-connections and is given by equation (4)

$$N_f = N_o W - N_o \int_0^W f(x)dx\,. \tag{4.4}$$

In addition to the estimation of the number of free connections due to an interfacing of the reservoir and vascular networks, other geometric parameters of the reservoir were also investigated. These parameters have been listed in Table 4.1 and have been defined below.

Further, similar analyses were carried out for rectangular and branched reservoirs by changing the parameters in the mathematical model that is suited to rectangular and branched geometries in MATLAB7.4 to study the parameters listed in Table 4.1.

1. Compactness: ratio of the perimeter of the reservoir (length of the red boundary as shown in Figure 4.1A) to the area of the virtual boundary (dashed green boundary in Figure 4.1A)
2. Enhancement in functional perimeter: ratio of the length of the reservoir that interfaces with vascular networks (length of the red boundary as shown in Figure 4.1A) to its non-interfacing length (length of the dashed blue –boundary in Figure 4.1A.)

Table 4.1 Parameter considered during reservoir geometry consideration.

S.No	Parameter	Formulae	Significance in fluid flow
1	Enhancement in perimeter ratio	Enhancement in perimeter = Length of the reservoir segment that interfaces with vascular networks / Length of reservoir segment that does not interface with vascular networks	Increased functional perimeter due to shape effect
2	The number of free connections of channels with the reservoir	Free connection = total number of times the perimeter of the reservoir crosses vascular network cross-connections	Number of channels that actually contribute fluid flow from the source to the sink reservoir
3	Compactness	Compactness = Perimeter of the reservoir / Area covered by virtual boundary of reservoir	Number of connections with reservoir per unit area

An ideal reservoir, which connects a vascular network within the fixed size of a virtual boundary that encloses reservoirs, should possess: (a) a large number of free connections with a random network of channels, (b) a high degree of compactness and (c) a high ratio of channel interfacing length to non-interfacing length. Based on these criteria, the geometry of the reservoirs, which is mentioned above, was evaluated for its efficiency.

.

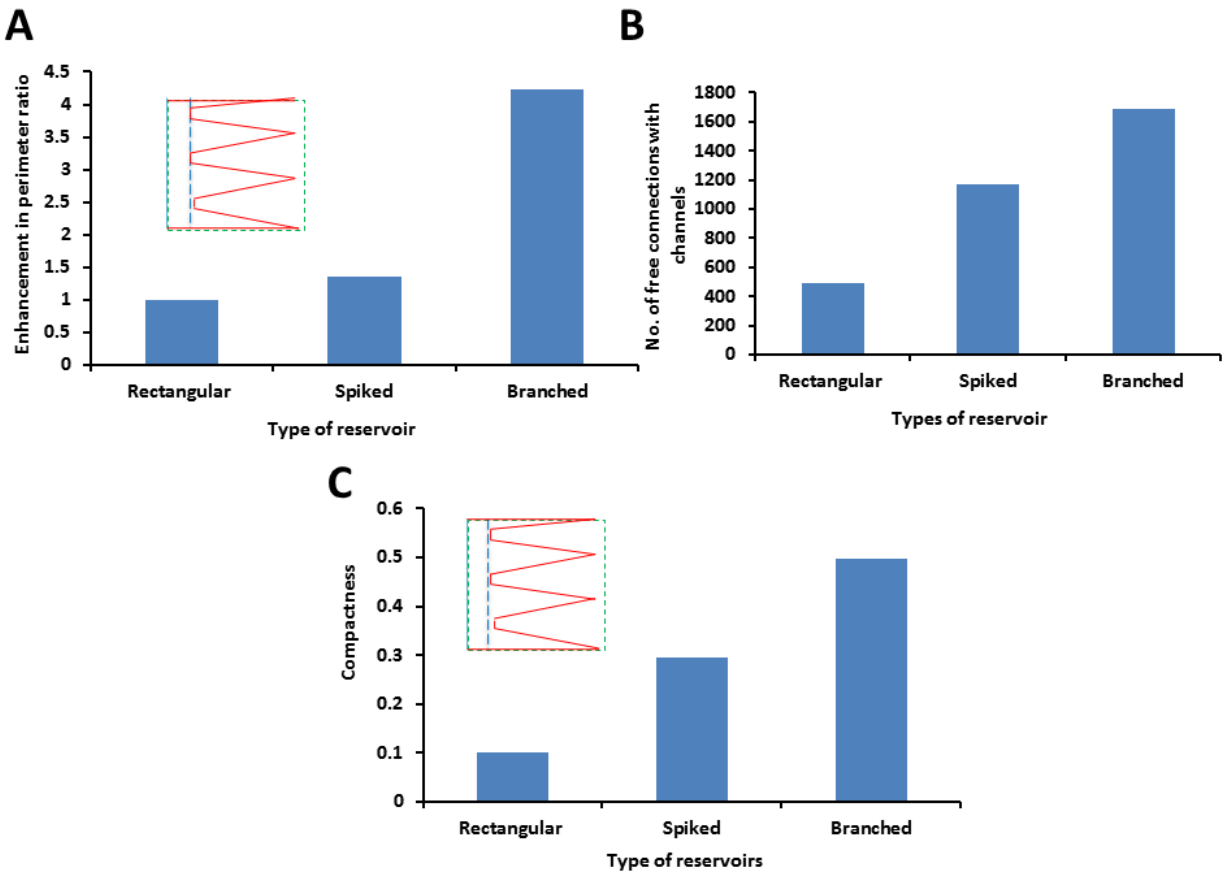

Figure 4.2 Comparison of rectangular, spiked and branched reservoir for A) Enhancement in perimeter ratio - ratio of segment of perimeter interfacing with nanochannel networks (red line) to non-interfacing length segment of reservoir (dashed blue line) B) Number of free connections of nano-channels with the reservoir C) Compactness of the device - ratio of actual perimeter (red line) to the area covered by virtual perimeter of bounding box (dashed green line).

Our analysis of the different shapes of reservoirs that are bounded by a fixed shape and size of virtual boundary and their connection with the vascular networks (Figure 4.1A) suggested that the design of the reservoir is crucial in delivering fluid to a vascularised polymer matrix. Design parameters such as the shape of the reservoirs and their hydraulic diameters were explored in an estimation of volumetric flow through the network of channels. The hydraulic diameters of the reservoirs were quite comparable, resulting in fluid flow resistances in a similar order of magnitude. Moreover, the hydraulic diameters of the

reservoirs were approximately 1000 times larger than the hydraulic diameter of the channels, resulting in a fluid flow rate that was limited by the resistance offered by the vascular networks. Although, the volumetric flow through the network of channels is dependent on the hydraulic diameter of the channels and their degree of connectivity with the reservoirs, under the premise of a fixed diameter of channels, the volumetric flow through them can be increased by an increase in the extent of the interface with the reservoirs. Therefore, the maximum possible sizes of different types of reservoirs were designed with a 100 mm^2 area of a virtual boundary enclosing the reservoirs. Under this condition, the perimeters of the branched, spiked and rectangular reservoirs were 49.67mm, 29.58mm and 10mm, respectively. Thus, when rectangular reservoirs were used to connect the vascular networks, the number of channels accessible directly to the reservoir depended strongly on the density of the channels (number of channels per unit length of the sample) and the length of the reservoir. The density of the channels was taken to be 50/mm, which is data that is taken from the experimental analysis that is explained in the section on results and discussion. Therefore, in order to increase the direct connection of the channels with the rectangular reservoir, the length of the rectangular reservoir needed to be increased. However, it could not be increased beyond a certain limit, considering the size constraint of the virtual boundary that enclosed the reservoir in micro/nanofluidic devices during the analysis. However, when the segment of the rectangular reservoir that interfaces with the vascular network was changed to spike shaped and branch-shaped, it increased the perimeter of the reservoir by 2.96 and 4.96 times**,** which was accessible to the vascular networks in a fixed area of the virtual boundary around the reservoirs. Thus, the ratio of the channel interfacing length of a reservoir to its non-interfacing length is found to be the highest in the case of the branch-shaped reservoir (Figure 4.2A) in comparison to the rectangular and spike-shaped reservoirs. This can be attributed to the peculiar branching geometry of a branch-shaped reservoir. Such geometry enables decrease in the area of the entry of the fluid and the increase in the length of the reservoir's segment that is accessible for interface with the vascular networks for connections This enhancement in the perimeter will lead to an increased connectivity of reservoirs with a random network of channels when compared to the rectangular reservoir and will also reduce the segment of the reservoir's length, which does not participate in channel interfacing.

However, it has been observed that an increase in the perimeter of the reservoir by merely changing the shape is not directly reflected in the number of free connections of the channel with the reservoir. This is primarily due to the angle between the spikes and the branches in the spike-shaped and branch-shaped reservoir, respectively. From the mathematical model it is clear that when the angle between the spikes or the branches in a spike-shaped reservoir or a branch-shaped reservoir is decreased, it leads to a decrease in the free connections and an increase in the perimeter of the reservoir per unit area. Thus, there is a trade-off between the number of free connections and the increased perimeter in a given area due to the decrease in the angle. However, it was observed that at an angle of 45^{o}, the perimeter increase per unit area was optimal, enabling the highest number of free connections. Therefore, the estimation of free connections at an angle of 45^{o} in branch-shaped and spike-shaped reservoirs was carried out in the current work. The number of free connections was the highest in a branched reservoir by virtue of its geometrical shape, as shown in Figure 4.2B, in comparison with the rectangular and spiked reservoirs.

Further, the comparison of the increase in the perimeter of a reservoir per unit area of the virtual boundary of the reservoirs termed as ‘compactness’ (Figure 4.2C), suggested that the branched shape was better than the spike-shaped and rectangular reservoirs. The compactness defines the performance of the device per unit area because an increase in the perimeter per unit area is directly related to the number of connections with a vascularised polymer matrix. Eventually, comparisons of the features mentioned above suggest that the branched reservoir is better in connecting the vascularised polymer matrix in a virtual boundary of a fixed size in a micro/nanofluidic device with an external fluidic port. Further, branched shapes are also one of the most coveted designs of vascular networks for any transport phenomenon [105].

4.3. Micro/nanofabrication methods:

4.3.1. Electrospinning

One of the most facsimile techniques is electrospinning (Figure 4.3) which has the capabilities to produce structures having the morphologies ranging from approx. 100nm to 10s of few microns [106, 107]. The method involves the drawing of polymer solution or melts from a nozzle of a syringe by electric force to produce charged continuous fibers with

diameters in nanometer. The polymer solution is pumped through a nozzle of a needle when a high voltage is applied between ground and needle. As a result, when polymer solution or melt comes out of a needle tip, it forms a round drop due to the surface tension of the fluid. However, the applied field results in a charge development in the drop, eventually causing repulsion between charges. Under the effect of two competing forces, when the electric force exceeds the surface tension force, the drop deforms in a shape of cone popularly known as "Taylor cone". On further increase in electric field strength, fiber is ejected from the tip of the cone towards the negative ground electrode, provided the viscosity of the solution is enough to prevent breaking of drop into nano drops due to increased electrostatic repulsion[108]. The fibers produced are collected on the ground which may be of different shape and sizes. Further, the pattern of the collection of fibers on the ground depend on the geometry of collectors is well reported in the literature[109].

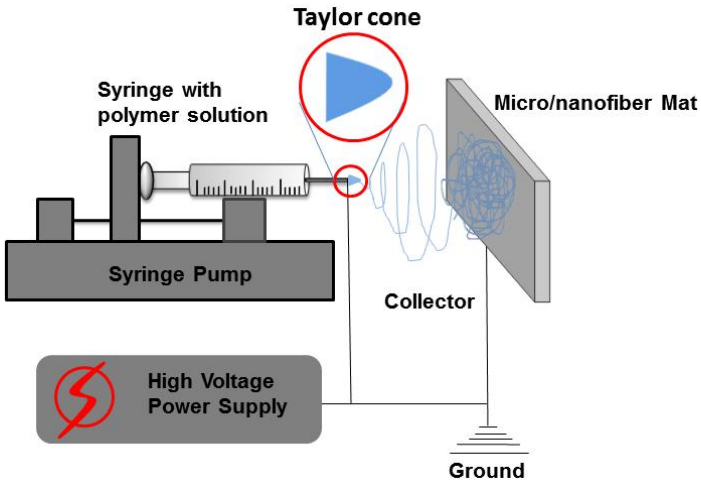

Figure 4.3 Schematic of electrospinning apparatus

The fibers produced by electrospinning has been widely used in research labs/commercial set-up for applications like tissue engineering scaffolding, advanced drug delivery, porous media, textiles, nanosensors[110], however, they have been minimally explored for design and fabrication of micro/nanofluidic devices. The micro/nanofibers produced by electrospinning can either act as a template[111] or used as a sacrificial material for the generation of channels in a polymeric substrate[100]. The combination of electrospinning with soft lithographic variants is capable of generating channels with desired

nano dimensions. There is only handful of literature available which elucidates the potential use of electrospun micro/nanofibers for generating a random network of 3D micro/nanochannels having a circular cross-section, which is otherwise difficult to fabricate by traditional lithography-based techniques.

4.3.2. Solvent etching of sacrificial structures

Etching of sacrificial surface layer of silicon and glass substrates have been routinely used in lithography techniques for fabrication of micro/nanochannels. There are two methods, commonly employed for etching of the substrate; wet and dry etching. The wet etching involves the dissolution of exposed surface of a substrate to their respective solvents, leading the formation of defined narrow openings termed as micro/nanochannels. It should be noted that the resolution of the mask, nature of the solvents and their time of exposure to the substrate determine the dimensional resolution of channels[112]. However, solvent etching phenomenon has been recently explored to etch away sacrificial structures embedded in the bulk of host polymer which is immune to solvent, as opposite to surface layer-by-layer etching in traditional lithography. The solvent etching of embedded structures in polymer matrices is quite slow due to an indirect interaction between the solvent and sacrificial layer.

4.3.3. Spin coating

Spin coating is the process of depositing a uniform thin film coating of polymer or solvent on a substrate (Figure 4.4). A small amount of polymer or solvent solution is placed at the centre of the substrate which is subjected to centrifugal force. Under the influence of centrifugal force supplied by a spin coater and viscous forces within the solution, a uniform thin film is created over the substrate as shown in the figure. This process is routinely used in soft lithography to fabricate a sacrificial layer of SU-8 on silicon[112]. However, the spin coating also has been explored for fabrication of thin membranes of elastomeric polymers[113]. Recently, the spin coating has been also employed to generate free-standing thin membrane to be used for various applications[114].

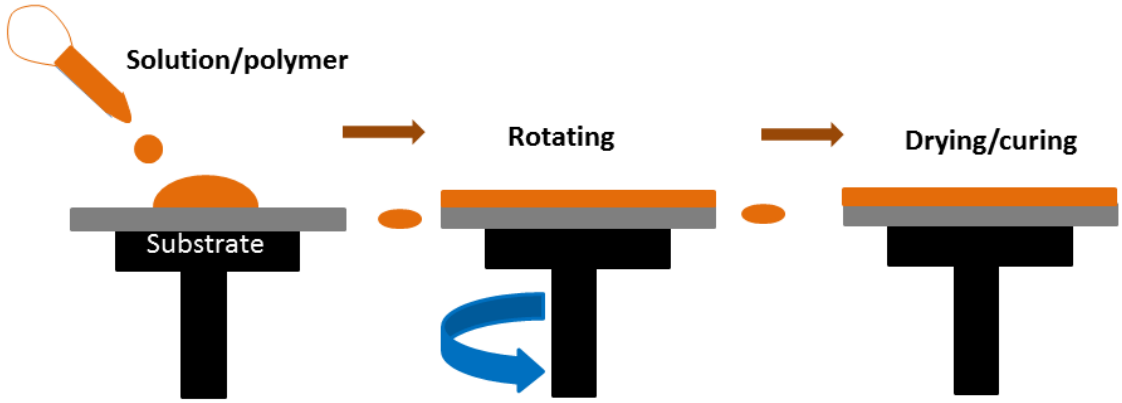

Figure 4.4 Schematic showing the workflow of fabricating thin film of PDMS by spin coating

4.4. Materials and Method

4.4.1. Materials:

Tissue culture polystyrene (Mw 106 kDa; TPP Techno Plastic Products AG, Switzerland); and Solvent grade N, N-dimethylformamide (DMF); and tetrahydrofuran (THF) (Merck Ltd., India) were used to formulate the solution for electrospinning and as etchants. Acetone and ethanol were used as solvents (Merck Ltd., India). Polydimethylsiloxane (PDMS) (Sylgard® 184 silicone *elastomer* kit - *Dow* Corning) was used for fabrication of micro/nanofluidic devices. Disodium Fluorescein (Sigma-Aldrich Pvt. Ltd., India) was used as the dye. Urea was used as a solute in diffusion experiments (Merck KGaA Ltd, Germany).

4.4.2. Methods:

4.4.2.1. Fabrication and characterization of micro/-nanofluidic devices

For 3D micro/nanofluidic device fabrication (Figure 4.5), the sacrificial electrospun micro/nanofibre mesh was transferred onto a glass slide that was coated with a PDMS film. For electrospinning, a 15% w/v polystyrene solution was prepared in THF and DMF in a 3:1 ratio. The process parameters were optimised to generate fibres with diameters of 1µm at a voltage of 10KV, a distance of 12cm between the collector and the spinneret, a solution flow rate of 0.5ml/hr by a syringe pump, a deposition time of 1–2 minutes and a needle gauge of 24G. Thereafter, the sacrificial micro/nanostructures on glass slides were mounted onto

copper stubs and prepared with a gold/platinum coating using a sputter coater for scanning electron microscopy (SEM) (FEI QUANTA 200, FEI, USA), which was operated at 20 kV and 10 kV, respectively, for structural and morphological characterization. The images were taken at different magnifications for a complete morphological analysis. The structural parameters of the samples were analysed by image processing in MATLAB® 2009a. After this, the entire sacrificial structure was embedded in a 1-2mm thin block of PDMS, as shown in Figure 3. For this, glass slide coated with a thin film of PDMS (20-30µm) were used to deposit nanofiber net and thereafter, uncured PDMS was poured from sides, such that PDMS seeps into the fiber net without collapsing the nanofiber net. Then PDMS was cured at 70^{o}C for 6-8 hours to obtain PDMS block having embedded nanofiber net. Further, openings were created in the PDMS block to increase the accessibility of the etchants for the removal of sacrificial structures. These blocks were kept in DMF for several days, until the sacrificial structures were completely etched, leaving behind random vascular (micro/nanochannel) networks in the thin PDMS block. Further, these blocks were sonicated in a DMF solvent in a water bath sonicator at intervals of a certain number of days in order to accelerate the etching of sacrificial structures and to remove debris before using thin, vascularised PDMS block as a device for dye flow and mass transfer experiments.

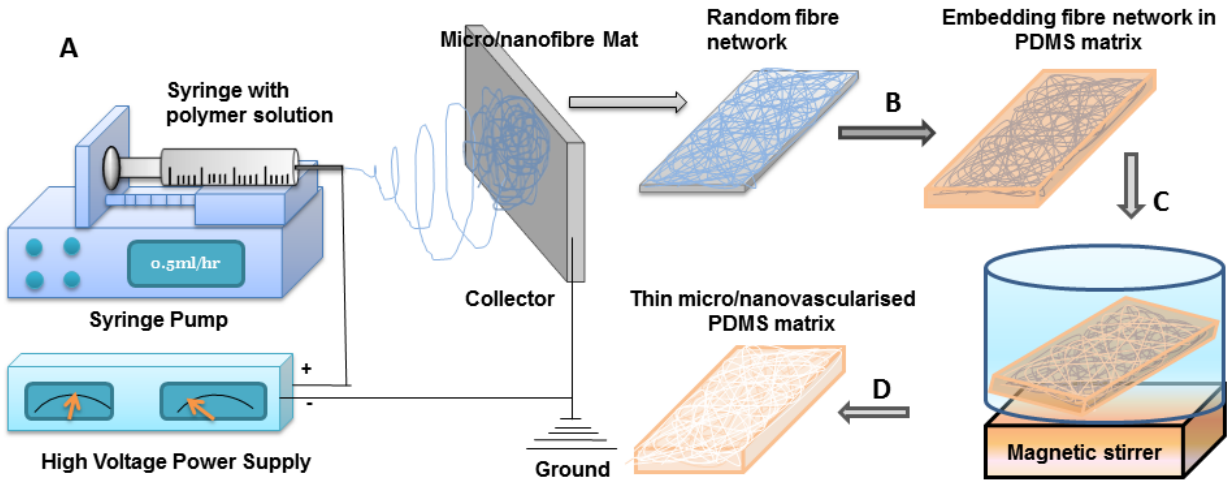

Figure 4.5 showing the schematic of the fabrication process of thin micro/-nanovascularised PDMS matrices. A) Electrospinning generates sacrificial micro/-nanofiber mesh B) The sacrificial micro/-nanofibers are embedded in thin PDMS matrices C) The PDMS matrices

having micro/-nanofibers are subjected to solvent (DMF) etching over magnetic stirrer D) Eventually, etching of fiber results in thin micro/-nanovascularised PDMS matrices[85]

4.4.2.2. Characterization of flow through micro/-nanofluidic devices

To further investigate the fluid flow rate dependence on reservoir's geometry in 3D micro/nanofludic devices, the vascularised polymer matrices that were fabricated were plasma treated (Basic Plasma Cleaner PDC-32G, Harrick Plasma, USA) at 1 mbar for 20–25 seconds and bonded to clean glass slides. Thereafter, the branch-shaped and rectangle-shaped reservoirs were created by punching slots in thin vascularised PDMS matrices, such that the virtual boundary (size of 10 mm × 10mm) enclosing the reservoirs was constant. Then, during dye flow experiments, time-lapse imaging was carried out within a virtual boundary that enclosed the reservoirs in a device. Further, the density of the channels and the interfacing perimeter of the reservoir with the channels were measured from the images of samples. During the experimentation, the area of vascularised polymer matrix under observations for dye-coverage and subsequent imaging were undertaken at a constant distance from the connected reservoirs. Images were acquired during dye flow at regular intervals with an optical microscope (Olympus, MX40, Olympus Corporation, Japan) in order to locate the dye in the channels at a given depth of focus and magnification. The images were further processed by image processing in order to estimate the dye-coverage area in the vascularised polymer matrix in MATLAB®9a. The estimated dye-coverage area was directly related to the volume of fluid flow in the vascularised polymer matrices. Further, vascularized polymers with different channel density and tortuosity of channels were used to study the dye coverage as proposed above. An empirical relation for the area of dye coverage with respect to the density and the tortuosity of channel network was determined from the experimentally recorded data.

4.4.2.3. Study of diffusion of urea across micro/nanofluidic devices

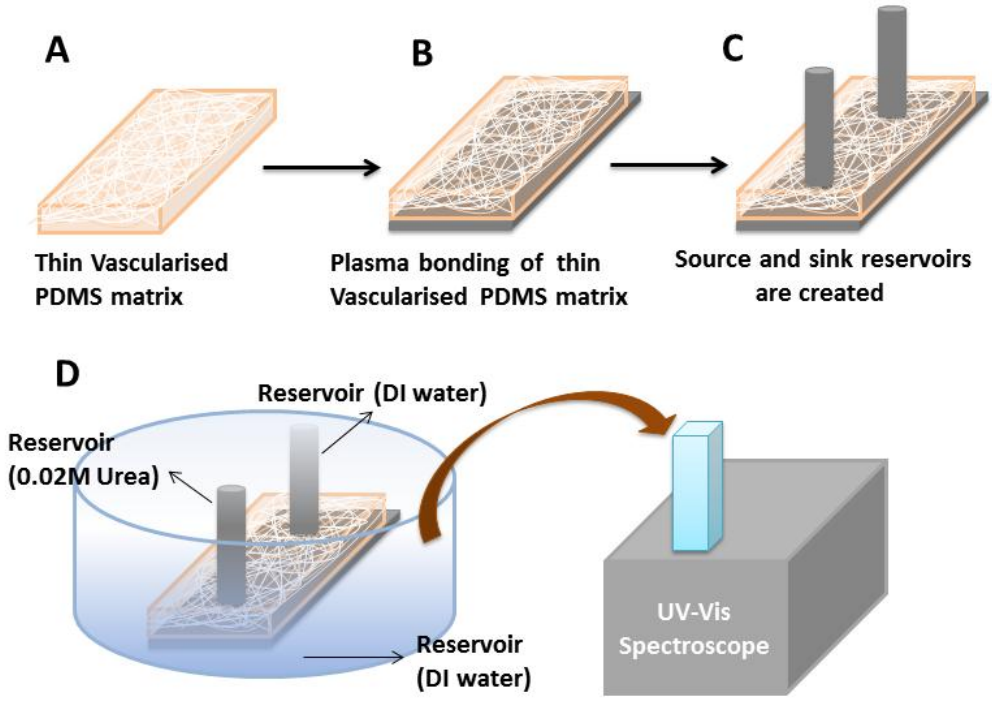

Figure 4.6 showing the schematic of fabrication of 3D micro/nanofluidic device from thin vascularised PDMS matrix and study of diffusion process under static condition. The steps of fabrication are A) a clean thin vascularised PDMS matrix is taken B) it is bonded to clean glass slide by their plasma treatment at 1mbar for 20-25 seconds and heat treated at 70^{o}C for 30 minutes C) two reservoirs (source and sink) are created and sealed with adhesive to form leak-proof bonding.

The vascularised PDMS matrices were used to design set-up for studying diffusion through them (Figure 4.6). Vascularised PDMS matrices having the thickness of 1mm were thoroughly washed in water to remove dirt or debris of polystyrene that formed during an etching process. Thereafter, these matrices and clean glass slides were treated with plasma (Basic Plasma Cleaner PDC-32G, Harrick Plasma, USA) at 1 mbar for 20–25 seconds to expose the functionalities on their surfaces. Further, these plasma-treated matrices and clean glass slides were bonded to each other. These bonded samples were then heated at 70 ^{o}C for 30 minutes to strengthen the bonding between the matrices and the glass slides, and to form a

leak-proof bonding. The two reservoirs were then created into a PDMS matrix that was bonded to a glass slide to form 3D micro/nanofluidic devices. A diffusion study set-up was created, as shown in a Figure 4.6D. Reservoir A was filled with 3ml of a urea solution of 0.02M, and reservoir B was filled with 2ml of deionised (DI) water. Reservoir C was filled with 40ml of DI water. The urea from A moves towards B by the process of diffusion through the network of channels between the reservoirs. Meanwhile, as the urea diffused through the network of channels, it also diffused across the PDMS matrix, which had an area of $1cm^2$, to the reservoir C due to a concentration gradient of urea across the matrix's thickness[85]. At regular intervals of 15 minutes, 2ml of the solution from C was taken and the absorbance peak was measured by UV-Vis spectroscopy (USB4000-UV-VIS Spectrometer, Ocean Optics), as shown in Figure 6A. Next, the absorbance peak was converted to moles of urea by using the calibration curve that had the correlation between the peak height and the concentration of urea[115]. These experiments were repeated for PDMS matrices in which random vascularised networks connected to a branch-shaped reservoir. The flux of urea from the vascularised PDMS matrices, which are mentioned above, with and without branch-shaped intermediate reservoir was estimated and compared. Further, above diffusion study was carried out with vascularized polymer matrices having varying channel density connected to the rectangular reservoir to determine the role of channel density on the mass flux of urea.

4.5. Results and discussion

4.5.1. Structural characterization of micro/nanofluidic devices

The fabrication of a 3D micro/nanofluidic device by using electrospinning is an inexpensive, scalable and convenient method. Since polystyrene is readily available, sacrificial material and PDMS, which are commonly used materials in fluidic devices, were employed. The SEM images of polystyrene micro/nanofibre networks Figure 4.7(A), which were produced by electrospinning, were utilized to obtain diameter distribution and degree of randomness analysis through image processing. A fibre mesh with a global diameter of 1.04±0.32 μm was obtained. Further, the fast Fourier transforms (FFT) analysis of the SEM images of the micro/nanofibre network was carried out to quantify randomness [116]. The angle of spread calculated from the FFT image was more than 150^o—indicating the high level of randomness

in the fibre mesh, which supports our assumption in the theoretical model. The thickness of the nanofiber net were in couple of hundreds of micron (Figure 4.7B) . The SEM images shown in Figure 4.7B illustrate the openings on the surface of the PDMS, which formed because of the etching of micro/nanofibres in a PDMS block.

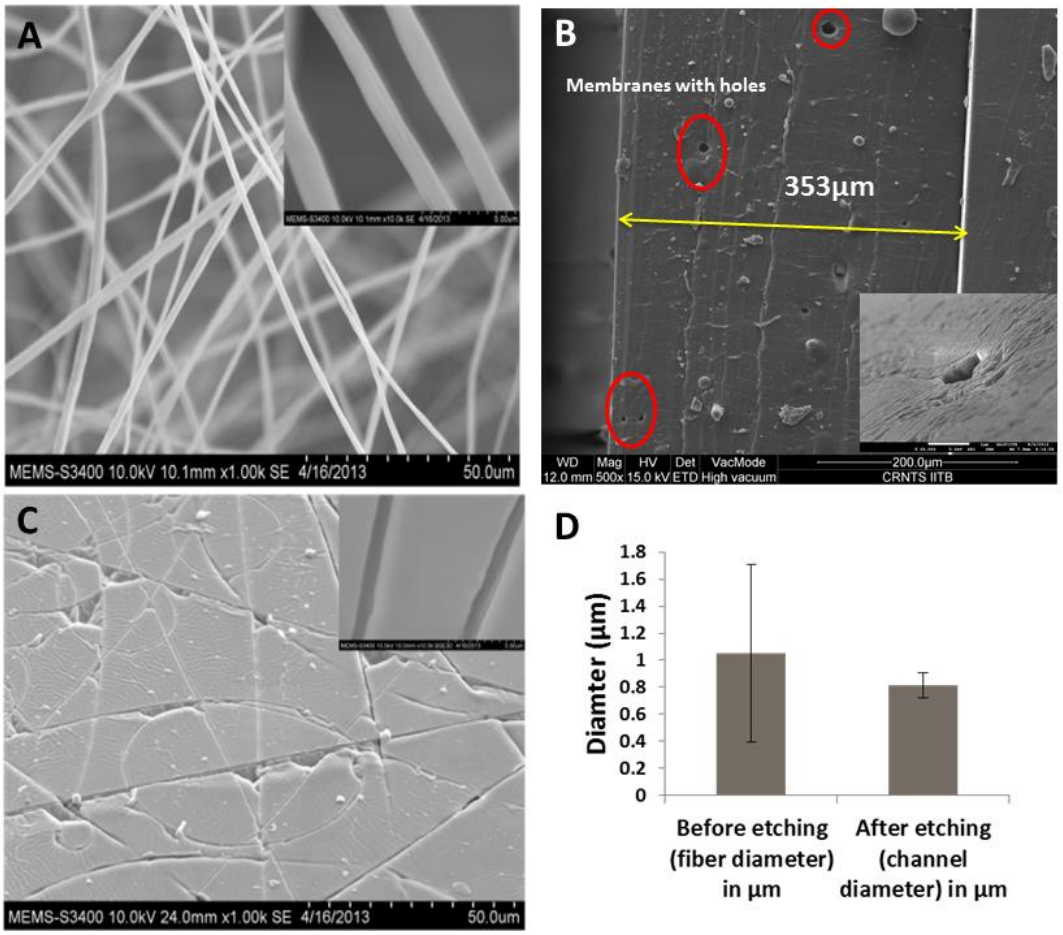

Figure 4.7 Scanning Electron Micrograph of A) electrospun polystyrene nanofibrous matrix B) cross-section of thin vascularised PDMS matrix showing holes C) PDMS matrix with micro/nanovascularisation. D) Graph showing the comparison of nanofiber and nanochannel diameter before and after solvent etching

Although sacrificial fibres were contiguous in nature, the discontinuous openings suggested that a part of the channels are inside the PDMS, forming a continuous vascularised network. The diameter analysis (Figure 4.7D) of the sacrificial fibres and the channels demonstrated that the etching of sacrificial fibres by solvent did not affect the channel dimensions. The connectivity and continuity of channels in vascularised polymer matrices were further

confirmed by capillary dye flow experiments (Figure 4.8C). They indicated the successful etching of the sacrificial structures. Thus, we successfully fabricated a micro/nanofluidic device, which is ready to be interfaced with different shapes of reservoirs that have a fixed area of the virtual boundary for effective connection with external fluidic circuits.

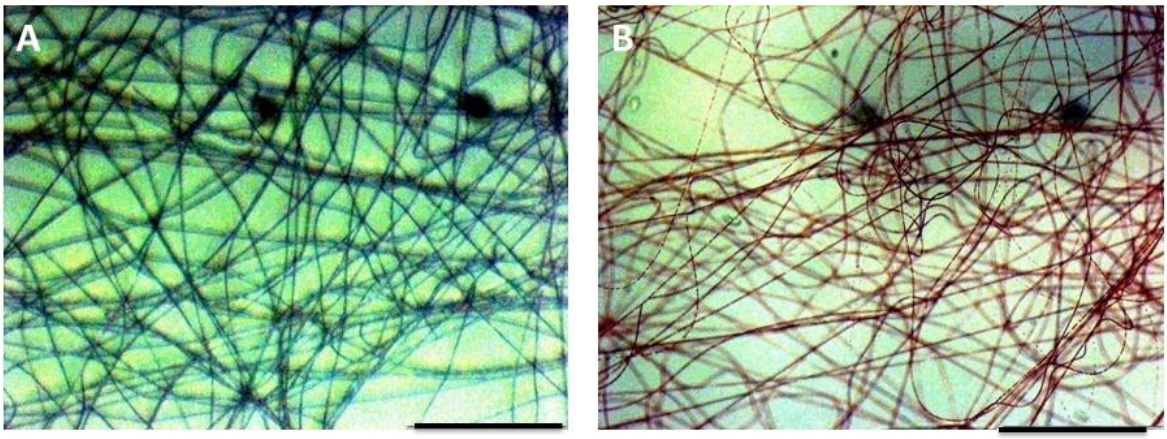

Figure 4.8 Microscope image showing the vascular network in PDMS A) before fluorescein dye flow experiment and B) after fluorescein dye flow experiment

4.5.2. Fluid flow study through micro/nanofluidic devices

Although the volumetric flow rate of a fluid through a vascular network is dependent on a number of factors such as the dimension of the channels, the inner wall morphology of the channels, the tortuosity of channels, the surface tension and the viscosity of the fluid [117, 118], the time-dependent dye flow experiments in microdevices suggested the role of the reservoir's geometry in volumetric flow through vascularised PDMS matrices. The virtual boundary that enclosed the reservoirs were 100mm^2, while the channels that interfaced with the perimeter of the maximum size of branched reservoirs and rectangular reservoirs that were accommodated within the virtual boundary was 26mm and 9mm, respectively. Further, the average density of the channels was 50±7 channels per mm length of samples we observed that vascularised matrices that interfaced with branch-shaped reservoirs demonstrated better volumetric fluid flow, which is represented by an area under the curve at a given time point, in comparison with interfacing with rectangular reservoirs (Figure 4.9A). Thus, we concluded that an enhanced volumetric fluid flow through a vascularised PDMS

matrix can be achieved by better interfacing with a reservoir system that is connected to an external fluidic port. This is because of a branched reservoir, due to its shape factor, offers a greater interfacing length in vascular networks that are within a fixed area and shape of virtual boundary that encloses the reservoirs in a device. Hence, such interfacing results in an increased participation of a large number of channels in a fluid flow at a given time. In contrast, rectangular reservoirs can achieve greater interfacing length by increasing their size only. Therefore, such reservoirs are not suitable when the microdevice is small. The curves in Figure 4.9A represent an average of the fluid flow behaviour through randomly distributed multiple channels, which is orchestrated by dye flow through capillary action and has varying dimensions, tortuosity, and roughness. However, the curve does not show a steep rise in the beginning because the region of volumetric flow measurement in the device was far away from the interface of the channels and the reservoir; therefore, it could not capture the high fluid velocity at the entrance of the channels that are connected to the reservoir.

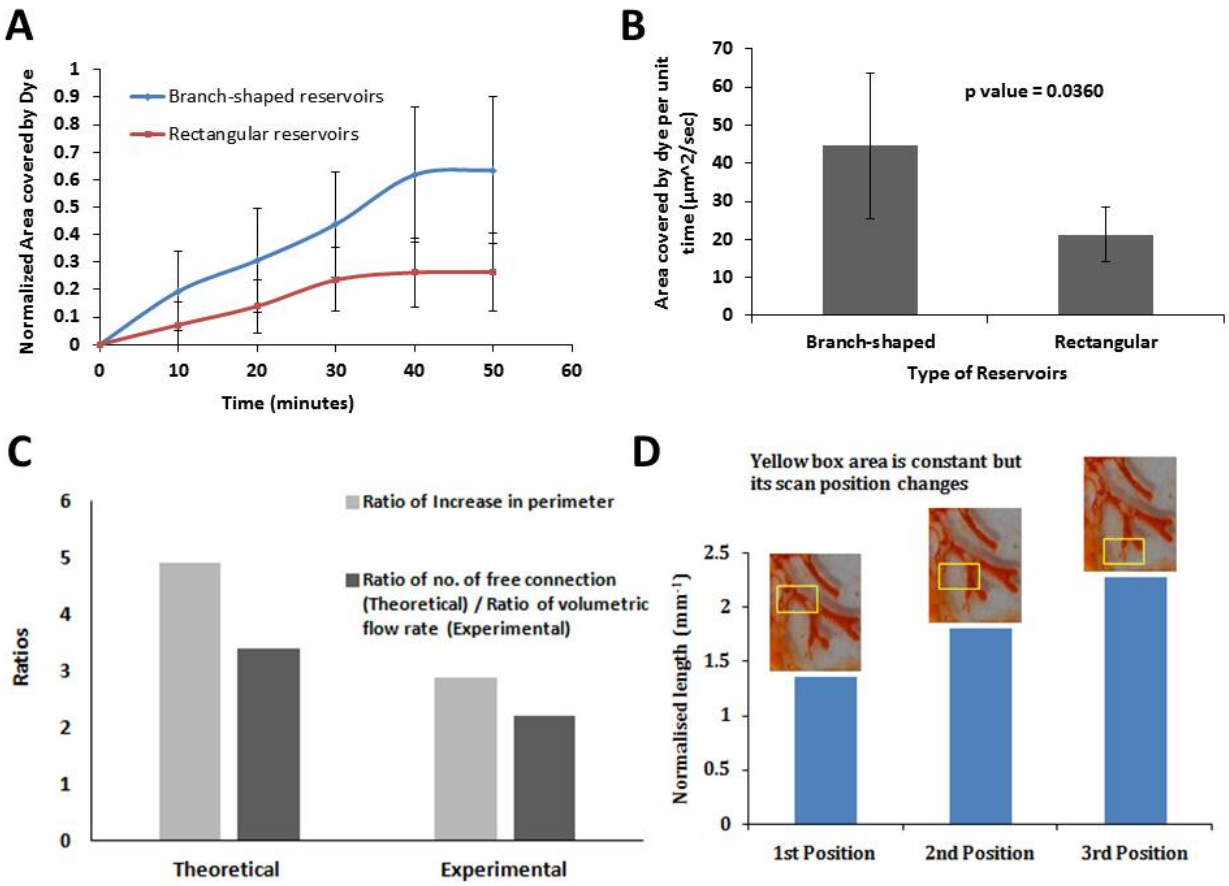

Figure 4.9 Graph showing A) the progress of dye coverage area with respect to time in a nanovascularised polymer matrix when connected to branched and rectangular reservoir in a device of area (10mm × 10mm) B) comparison of area covered by dye per unit time in a nanovascularised polymer matrix connected to branched and rectangular reservoir respectively C) the increase in a perimeter per unit area of a branched reservoir while moving from parent to daughter branches in a branched reservoir D) Comparison of experimental and theoretical results showing the ratio of increase in perimeter of reservoir when shape in changed from rectangular to branch-shaped on increase in the ratio of number of free connections and the ratio of volumetric flow

Further, the slope of the curves in Figure 4.9A was estimated by a straight-line fit for the two reservoirs cases in order to determine the volumetric fluid flow rate. The volumetric fluid flow rate was significantly higher in a vascularised PDMS matrix that was connected to the branched reservoir when compared to the rectangular reservoir (Figure

4.9B). Further, the statistical analysis by paired *t-test* revealed that the probability of obtaining an enhanced volumetric flow rate in a vascularised PDMS matrix that is connected to the branch-shaped reservoir in comparison to the rectangular reservoir in an unbiased four-sample set is 96.4% (p-value 0.036). This is primarily due to the increase in the number of channels that contribute to the volumetric flow rate when connected to a branch-shaped reservoir as opposed to a rectangular reservoir. Moreover, the volumetric flow rate in vascular networks is likely to be affected by flow resistances in these reservoirs, which act as an intermediate between the external fluidic port and the vascular networks. However, due to large differences in the dimensions of the hydraulic diameter of reservoirs (1.33mm) and micro/nanochannels (1.04±0.32μm), the resistance offered to the flow, which is inversely proportional to fourth power of the hydraulic diameter in the reservoir, is negligible when compared to vascular networks. Therefore, in the current study, we have neglected flow resistances in the reservoirs and emphasised on the flow behaviour through a vascular network only, although the shape of the branch-shaped reservoir will have a minimal effect on the flow resistance.

Moreover, when we compared the enhancement in a fluid flow rate that was obtained experimentally with the number of connections between the vascularised PDMS matrix and the reservoir that was obtained from our theoretical analysis, we observed (Figure 4.9C) that the theoretical results suggested that the numbers of free connections with the branch-shaped reservoir were 3.4 times higher than those with the rectangular reservoir when the interfacing perimeter was increased from 10mm to 49.67mm. Meanwhile, the enhancement of fluid flow in the vascularised PDMS matrix during experimentation, when connected to the branch-shaped reservoir, was 2.2 times higher than that in a rectangular reservoir, when the interfacing perimeter was increased from 9mm to 26mm. Thus, the increase in the perimeter of the reservoir leads to increased interfacing with vascular networks, enabling enhanced volumetric flow. Although, our theoretical results are almost consistent with our experimental approach, small differences have arisen from: (a) the low contribution to the flow measurement by all the partially formed channels, due to incomplete solvent etching, connected directly to the reservoir and (b) deviation of the level of randomness in the vascular networks, which is assumed in the theoretical model from the sample that was used in the experiments. Nevertheless, we have considered a two-

dimensional system to demonstrate that the extent of interfacing of the vascularised system with the reservoirs depends on the perimeter of reservoir. In an actual three-dimensional system, however, the degree of interfacing would be dependent on the product of the perimeter of the reservoirs and the diameter of the vascular network. Since the diameter of the vascular network was very small in comparison to the perimeter of the reservoirs, our experimental and theoretical analysis that considers the device to be two dimensional would yield fairly accurate results even if the actual device was three dimensional.

To estimate the extent of the role of shape in an increase in the perimeter of branch-shaped reservoirs per unit area, images of branched reservoirs that were fabricated in PDMS as a replica of a mould created by the Hele-Shaw cell[119] were processed. In the Figure 4.9D, the yellow virtual boundary with the constant area was traversed gradually from parent to daughter branches. The perimeter of branched structure lying inside the yellow boundary at three distinct positions was estimated. We observed an increase in the perimeter of the branched structure that was bounded by yellow due to an increase in the number of fingers or branches lying inside the yellow bounding box, as shown in Figure 5D. Thus, an increase in the branching of branched reservoirs within a fixed virtual boundary will contribute towards enhanced perimeter per unit area (compactness).

The volumetric flow rate through the network of channels is also dependent on an area of observation in a microdevice, the degree of randomness in vascular networks and the vasculature density. Furthermore, there would be enhanced volumetric fluid flow through the vascularised PDMS matrix due to an increase in the channel density and the proximity of the area under observation with respect to the interfacing junction of the vascular network and the reservoirs, as suggested by the theoretical model. It was experimentally contemplated that nanochannel density and level of randomness plays a vital role in the nature of the area coverage curves. The variation in the velocity of area coverage shown in Figure 4.9A is due to the variation of above parameters in vascularized polymers. For an experimental set-up, controlling the nanochannel density, keeping the level of randomness constant and vice-versa is quite challenging. So for the sample set of 5, these parameters (density and tortuosity) were estimated from their respective images through image processing. The process and algorithm for estimation of density and tortuosity are described in Appendix 2. Further, the

regression analysis was carried out to established empirical relations between the area coverage velocity obtained experimentally and above parameters. The empirical relation is shown by the equation

$$V = K \frac{Cd^{0.8128}}{Lr^{1.8477}} \tag{4.5}$$

Where *V* is the velocity of area coverage by the dye, *Cd* is the channel density, *Lr* is the level of randomness and *K* is the constant of proportionality. Furthermore, the obtained empirical relation was used to predict the area coverage velocity in samples with known channel density and tortuosity. The experimental results corroborated well with results obtained in those samples through dye-flow experiments as shown in the Figure 4.10.

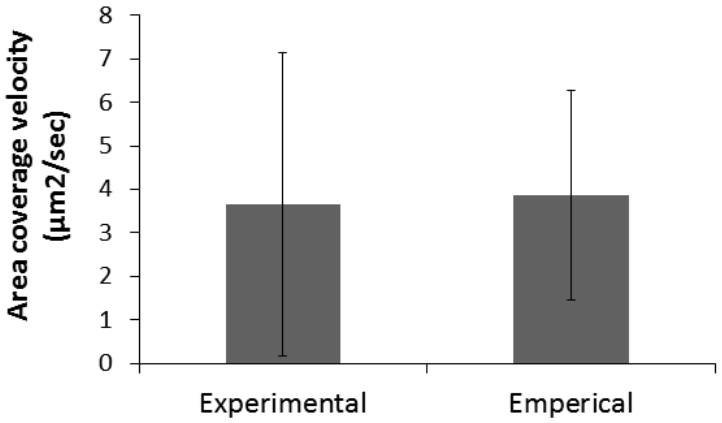

Figure 4.10 Graph showing the comparison of area coverage velocity estimated through experiments and empirical relation

As the distance between measuring area and the reservoir was increased, it decreased the propensity of a direct connection between the reservoir and measuring area and increased the path length of nanochannel between the reservoir and measuring area. This leads to the reduction in the velocity of capillary flow in nanochannel network with an increase in distance between the reservoir and measuring area due to the continuous drop in capillary pressure due to increased path length. The velocity of capillary filling is retarded with the increase in the length of a liquid column in a microchannel[120]. Thus, increasing tortuosity increases the effective length of the microchannel, thereby contributing to the reduction in velocity[121]. Further, the density of vascular network determines the volume of flow

through these matrices. The empirical results were found to be in good agreement with mathematical expression of capillary filling in tortuous channel network[103]

4.5.3. Diffusion study through micro/nanofluidic devices

We have also studied the mass transfer behaviour of micro/nanovascularised PDMS matrices interfaced with different shapes of reservoirs in 3D micro/nanofluidic devices. The diffusion flux of urea across these thin vascularised PDMS matrices interfaced with different reservoir shapes (Figure 4.11A) illustrated the role of reservoirs on the degree of diffusion of solute (urea in this case). It was observed that micro/nanovascularised PDMS matrices demonstrated an increased ability of urea flux (1.7 times) across the matrices due to an increased participation of large number of nanochannels, when the PDMS matrices connected to external reservoir via branched-shaped reservoir as compared to micro/nanovascularised PDMS matrices connected directly to an external rectangular reservoir. It also facilitated maximum utilization of micro/nanochannel networks in the solute exchange process. Therefore, it is apparent that increasing the density of micro/nanochannel network will correspondingly increase the surface area for diffusion. However, as simulation results in chapter 3 suggest the presence of optimal micro/nanochannel density during mass transfer in vascularized polymers.

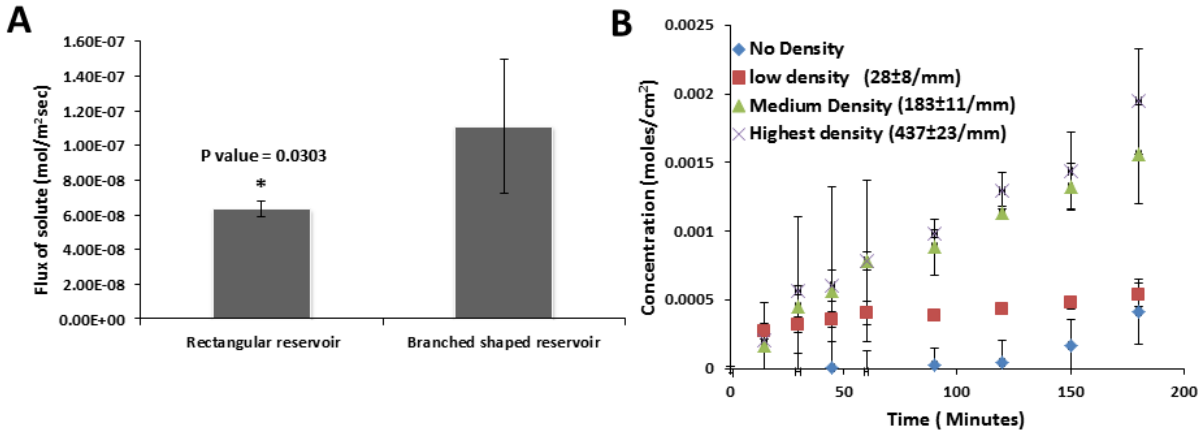

Figure 4.11 Graph showing flux of urea across the vascularised PDMS matrices A) interfaced with rectangular and branch-shaped reservoir, respectively B) having varying channel density

Therefore, the vascularised PDMS matrices fabricated with varied channel density were used for urea diffusion study using the setup described in Figure 4.6. It was observed that the urea diffusion across the PDMS matrices increased with an increase in the density of vascularization as shown in the Figure 4.11B. However, the increase in urea diffusion do not scale linearly with the density of vascularization and tends to demonstrate optimal channel density for maximum urea diffusion through given thickness of vascularized polymers systems. The results experimentally validate the trend of optimal vascularization density predicted by simulations in chapter 3. Although above study just illustrated the ability of 3D micro/nanofluidic devices for urea separation between two fluids, it can be a stepping stone for developing kidney dialyser in near future. Therefore, above design of nanofluidic devices, with an intermediate branch-shaped reservoir to connect to external fluidic circuits, will enable fabrication of high-performance nanofluidic devices - capable of enhancing fluid flow, thereby increasing heat and mass transfer properties. The current design and strategy can be employed for the fabrication of micro/nanofluidic devices where heat and mass transfer operations are of primary concern

4.6. Conclusion and future work

One of the major problems of connecting nanochannel networks in micro/-nanofluidic devices with external fluidic ports involves design and fabrication of intermediate reservoirs which act as a bridge between nanochannel networks and external fluidic ports. Our proposed statistical model suggested that branched shaped reservoir enhances direct connectivity with nano-channel network, increases the compactness of a micro-device and improves functional perimeter as compared to other shapes of reservoirs within a fixed size of the virtual boundary in micro-devices. In addition, we have demonstrated an easy, inexpensive and unsophisticated method for the design and fabrication of 3D micro/-nanofluidic devices in a polymeric substrate mimicking natural vasculature using sacrificial nanofibers formed by electrospinning. Further, interfacing the nanochannel networks with branched shaped reservoir enhances the volumetric flow capability of these fluidic devices. This places these nanofluidic devices as a promising candidate in applications which demand interplay of convection, diffusion, and reactions. For example, enhanced urea diffusion was observed through micro/nanovascularised PDMS matrices connected to branched-shaped reservoirs.

Thus, we have demonstrated reservoir geometry as a crucial design parameter in nanofluidic devices used in separation technologies. Further, investigation on the density and tortuosity of channel network in 3D micro/nanofluidic devices also suggested that volumetric flow follows direct and inverse square relationship with density and tortuosity, respectively. The empirical relation between the volumetric flow in vascularized polymers and density and tortuosity of vascular network obtained corroborated well with the theoretical model proposed in the literature. Thus, our study will enable the design and fabrication of micro-/nanovascularised polymer matrices with tailored structural properties for applications like lab-on-chip technologies, tissue engineering, and heat and gas exchangers.

Further, our attempted to fabricate an integrated, multi-scale, scalable vascularized polymers matrices with scalable micro-manufacturing technologies: electrospinning, 3-D printing, micro-molding and solvent etching of sacrificial structures resulted in a modest success (Appendix 1). Our structural characterization revealed that successful integration of fractal-shaped microchannels generated by micro moulding followed by 3D printing with a random network of micro/nanochannel network created by sacrificial etching of fibers embedded in host polymer system. Further, we demonstrated the flow of dye through the network of the multi-scale channel network. However, the fabrication methodology involved a series of steps which needed meticulous attention and skill to fabricate successful devices with intended multi-scale channel dimensions. Moreover, fractal-shaped channel network created by micro-molding in 3D printed mold has the limitation posed by the resolution of a 3D printer. The time scale of fabrication by 3D printer is relatively large for the fabrication of scaled up devices. The fabrication methodology proposed could not yield bio-inspired, multi-scale vascular polymer matrices but a lab-on-chip device with such morphologies. Thus, there is a need to design and develop a method that can fabricate to emulate multi-scale branching channel network in polymer matrices as observed in nature.

5. Chapter 5 Nature-inspired 3D, Multi-scale-Vascularised Polymer Matrices

5.1. Introduction

Our study suggested that interfacing of a random network of nanochannels with the reservoir of branched geometry is critical for enhancing the volumetric flow rate and mass transfer rate through them. However, the branched geometry of reservoir created through punching the vascularised polymer matrices is not a good scalable manufacturing practice. Moreover, it is not suitable for generating multi-scale, fractal/branched channel network. The fractal-like geometry vascular networks form a backbone of several natural functioning systems; for example, transport through venation system in leaves of trees[122], circulatory network in animals, fish gill, mammalian organ systems[123, 124] and so on. These fluid-flow networks typically display scales starting with few millimeters leading with multiple fractal generations to micrometer size branches further connected to submicron capillaries. These architectures are established to be efficient in being structurally sound and at the same time energy minimizing for heat and mass transport for both biological[125] and synthetic applications[126-128]. Mimicking these micro-scale features would have immense utility in tissue engineering[70, 125, 129], synthetic/artificial organs[130], and several other scientific and engineering investigations.

Nature-inspired, fractal geometry channels spanning multiple dimension scales have so far been fabricated by mainly using lithography techniques including nano-imprint lithography (NIL)[13, 131, 132]. In some cases, these 2D structures were stacked to achieve 3D fluidic networks [13]. Further, multi-scale channels were also obtained by combining different variants of lithography; UV and NIL[132]. In spite of such capabilities, lithography processes are expensive in both running and capital budgets. Apart from cost, substrate compatibility to obtain multi-scale structures, 2D nature of the process, and processing time remain inherent challenges to scale-up. Therefore, a large number of papers is found to demonstrate lithography-less, scalable fabrication of vascular network using sacrificial etching of fibrous structure embedded in host polymers[62, 75, 76, 100, 133, 134]. However, these vascular networks are random in nature and do not have multiple scales in channel dimension. Only lithography fewer attempts were found in the literature to fabricate fractal-geometry, large-area, scalable structures spanning micro and mesoscale and to the best of our

knowledge, no extension of the same to submicron capillaries is found. Electrostatic discharge assisted fabrication[135] a novel use of high electric-discharge (starting from single or multiple seed locations) in dielectric material leading to local polymer evaporation created the desired micro-meso fractal-like geometry networks. This method, however, has limited control over the spread of the discharge in all directions and over connectivity of input and output apart from dimension achieved. The control over the dimensions of the channels remains a challenge due to chaotic nature of fabrication. Other methods[136, 137] used additive manufacturing by use of 3D printing using direct self-assembly of fugitive ink jet[136] and stereolithography (SLA) technology[137]. Both these methods have limits on resolution and scalability. Moreover, time for fabrication by above methods can be prohibitively high for scalable structures. Therefore, we propose in this paper a scalable process for fabrication of multi-scale, fractal microchannels connected efficiently to a random network of sub-micron capillaries. Saffman-Taylor instability well-known to produce viscous fingering along with sacrificial electrospun fiber network is adapted for the same.

Therefore, we combined the electrospun fibers with Hele-Shaw structures to generate sacrificial structures which form the basis of producing vascular networks in a polymer to finally get the proposed structure. Towards the goal, electrospun fibers are laid, under tuned conditions, over this fractal branched polymers and the entire structure is cast in thin PDMS matrix (which allows gas exchange). The structures were characterized for their connectivity and time efficient gas exchange is actually demonstrated. Thus, fabrication of micro/nanovascularised polymer matrix efficiently connected to an external fluidic port via an intermediate fractal-shaped macro-micro structure, pervasive in nature, is demonstrated. Although the intended scope of this work shows the one-way connection to the vascular network similar to a leaf, the process lays the foundation for continuous flow structures like secondary lamella of fish gills. Further by using biocompatible polymer matrices, efficient cell growth systems can be fabricated economically at larger scale.

5.2. Micro/nanofabrication

5.2.1. Hele-Shaw cell:

A rich literature can be found on a variant of Saffman-Taylor instability demonstrated in a lifted Hele-Shaw cell[138] investigating both theoretical and experimental domains of fractal-like fingering process. In a lifted Hele-Shaw cell, a high viscosity fluid is compressed between two plates and the plates are angularly separated to allow low viscosity air fingers to penetrate in an unstable way[139]. It is a device which enables the fabrication of fractal-shaped morphologies with viscous fluid exhibiting yield stress behavior. Figure 5.1 illustrates the working of the Hele-Shaw cell. A drop of a viscous fluid having yield stress properties is sandwiched between two glass slides and thereafter, the upper slide is lifted with its one of the end fixed as shown in Figure 5.1A. When a fluid drop is squeezed between the slides, it forms a thin layer between the plates. However, on lifting the upper slide, air being low viscous fluid perturbs the interface leading to Saffman-tailor instability. This instability progresses with a creation of fractal structure within a fluid film. The viscosity and surface tension of fluid will guide the stable fractal structures. The dimension of the fractal structure is governed by the thickness of the film between the two parallel glass slides, the speed of separation of glass slides, the angle of separation of glass slides and nature of the fluid. Penetrating fingers finally leave fractal geometry network on the cell plates with single point connectivity to the entire network. The phenomena are known to be scalable and depending on fluid properties can produce branched structures with a few micron dimensions at one end to few millimeter at the other over an area with virtually no restrictions

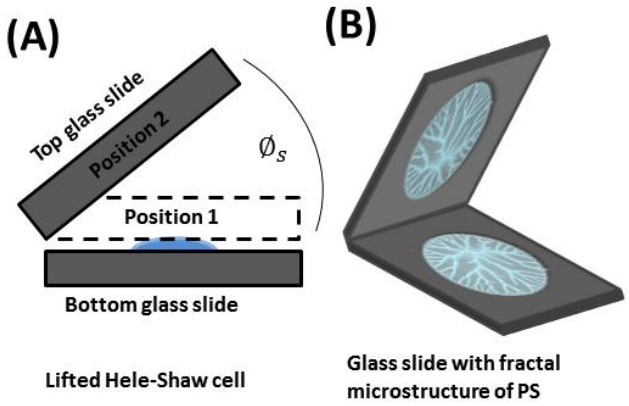

Figure 5.1 showing a) Schematic for fabrication process of fractal-shaped microstructures in polystyrene by controlled lifted Hele-shaw cell. The steps involved are squeezing the drop of PS solution between top and bottom glass slides shown as position 1 and then angular lifting the top slide to position 2 by angle $\emptyset_s$ b) fractal-shaped microstructures of polystyrene on glass slides.

5.3. Materials and methods:

5.3.1. Materials:

Tissue culture polystyrene (Mw 106 kDa; TPP Techno Plastic Products AG, Switzerland) and solvent grade N, N-dimethylformamide (DMF) and tetrahydrofuran (THF) (Merck Ltd., India) were utilized to formulate the solution for electrospinning and as solvent etchants. Acetone and ethanol were used as solvents (Merck Ltd., India) for washing and formulating dye solution. Polydimethylsiloxane (PDMS) (Sylgard® 184 silicone e*lastomer* kit - *Dow* Corning) was used for fabrication of micro/nanofluidic devices. Disodium Fluorescein (Sigma-Aldrich Pvt. Ltd., India) was used as the dye. Urea was used as a solute in diffusion experiments (Merck KGaA Ltd, Germany).

5.3.2. Method:

5.3.2.1. Fabrication of nature-inspired, multi-scale, 3D, channel network in PDMS matrices

The scalable multi-order channels are proposed to be fabricated by combining two technologies: Saffman Taylor instability in Hele-Shaw apparatus (Figure 5.1A & B) and electrospinning (Figure 4.3).

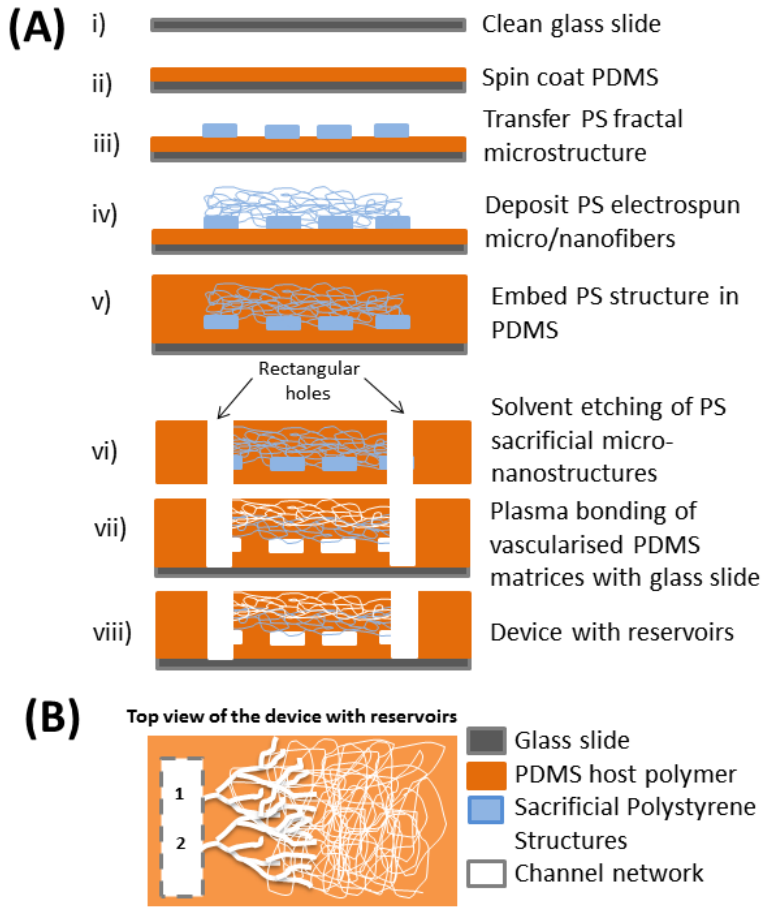

Figure 5.2 The steps of fabrications are i) glass slide is thoroughly cleaned with alcohol ii) PDMS is spin coated on glass slide at 800rpm for 2 minutes iii) solvent treated stable fractal-shaped microstructures formed by Hele-shaw cell is transferred to PDMS-coated glass slide iv) the electrospun micro/nanofibrous mesh is deposited over fractal-shaped microstructure before micro-nanofibers get dried to enable fusion between structures v) the sacrificial structures are embedded in thin PDMS matrices by pouring PDMS over the sacrificial structures and heat curing it vi) DMF is used to etch away the sacrificial element from host

PDMS matrices leaving behind multi-scale channel network thin PDMS matrices vii) plasma bonding of PDMS matrices with clean glass slide viii) the final schematic of multi-scale, nature inspired vascularised PDMS matrices with reservoir for flow and diffusion studies.

The steps in the fabrication process combining these two technologies are demonstrated schematically in Figure 5.2A. PDMS mixture was prepared in a (base and curing agent) 10:1 ratio and spin-coated on a glass slide at 800 rpm using spin coater to yield a thin film of 60µm (Figure 5.2A (ii)). Fractal-like structures formed by using 30% w/v of polystyrene solution in THF in a lifted-Hele Shaw cell (Figure 5.1A & B) by the process in [138] are then transferred on this PDMS (see schematic Figure 5.2 A (iii)). A 5-10 sec dip in DMF is given before transfer to remove the unwanted film formed between fractal fingers. In the next step (iv), wet polystyrene nanofibers were deposited on fractal shaped microstructures. For electrospinning process 15% w/v polystyrene solution in THF and DMF (ratio 3:1)[140] is used with the following process optimized parameters: voltage – 10KV, distance between collector and spinneret – 12cm, flow rate of solution by syringe pump – 0.5ml/hr, deposition time 1–2 minutes, and needle gauge of 24 gauges. In the next step (v), polystyrene multi-scale sacrificial structures were cast in PDMS and cured at 60^{o}C for 2-3 hrs. In the following step, PDMS device was peeled off the glass substrate to generate rectangular troughs ((Figure 5.2A (vi)) and sacrificial etch is performed in DMF solvent with sonication at a regular interval to accelerate the etching. After etching, the PDMS samples were thoroughly rinsed in DMF to remove polystyrene debris formed during the etching process. The samples and clean glass slides were bonded to each other (Figure 5.2A(vii)) after treatment with plasma (Basic Plasma Cleaner PDC-32G, Harrick Plasma, USA) at 1 mbar for 20-25 seconds exposed functionalities on their surfaces. The post-heating the bonded samples at 70^{o} C for 30 minutes strengthen the bonding between the matrices and the glass slides to form a leak proof bonding. Eventually, proposed device was obtained (Figure 5.2A (viii)). Meanwhile, the behavior of the etching rate of sacrificial structures was also estimated by measurement of loss of weight of samples at an interval of 4 days.

5.3.2.2. Characterization of samples

Characterization of the sample using SEM (FEI QUANTA 200, FEI, USA) operated at 20 kV and 10 kV, respectively, were carried out at significant steps of the process outlined in Figure 1d. The required sample preparation was carried out along with gold/platinum coating before imaging in SEM. Image processing toolbox in MATLAB® 2009a is used to extract parameters of interest (diameter of nanofibers, thickness, length and angle between branches of fractal shaped structures and diameter of channels) from images. Moreover, white light interferometry technique (in Polytech MSA 500 system) was used to analyze thickness variations in fractal micro-structures.

5.3.2.3. Characterization of connectivity of channels in samples

The connectivity among the channels of different length scale in a PDMS matrix is illustrated by dye flow experiments. One of the rectangular-shaped troughs in the device shown in Figure 5.2B (viii) was filled with a disodium fluorescein dye solution in ethanol. The dye flows through parent fractal channels and further to the connected nano/microchannel network through first generation branches opening at positions 1 and 2 as shown in Figure 5.2B. This nature inspired arrangement facilitates connection of a large number of nano/microchannels in the network via relatively low resistance fluid path[141]. The images of the devices were obtained after an hour of dye flow experiments at different magnification to illustrate the connectivity between fractal-shaped microchannels and micro/nanochannel networks and continuity in the channels after etching of sacrificial structures.

5.3.2.4. Study of diffusion of urea using the proposed device

The two reservoirs were cut into the device at step (vi) of Figure 5.1A for purpose of this study and a diffusion experiment as shown in Figure 5.3 was setup.

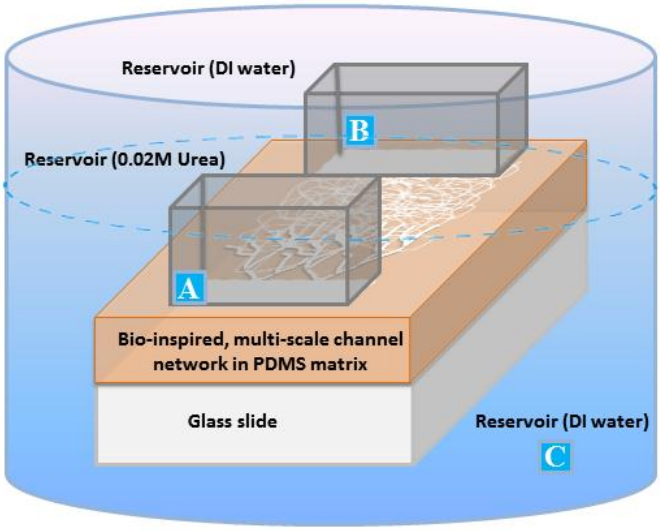

Figure 5.3 Schematic of experimental set-up to study diffusion

The reservoir A was filled with 3ml of 0.02M urea solution and the reservoir B was filled with 2ml of deionized (DI) water. The reservoir C was filled with 40ml of DI water. Urea from A diffuses to B through channel network and also to C through the thickness of urea-permeable PDMS. The concentration of urea is highest in parent branch and successively lower in daughter branches as diffusion occurs faster in the low volume high surface area parts[142]. At regular intervals of 15 minutes; 2ml of solution derived from C assisted in the measurement of absorbance peak by UV-Vis spectroscopy (USB4000-UV-VIS Spectrometer, Ocean Optics). Next, absorbance peak was converted to moles of urea by making use of the calibration curve having the correlation between the peak height and the concentration of urea[143]. The above experiments were repeated for PDMS matrices without any multi-scale vascularization as a control experiment.

5.4. Results and Discussion

5.4.1. Characterization of fractal-shaped microstructures

The process presented in Figure 5.1(A and B) is further characterized with respect to the following parameters[136]: concentration of the solution, the initial thickness of fluid, velocity of separation of plates. The concentration of the solution affects viscosity which plays a major role in triggering Saffman Taylor instability in Hele-Shaw cell. Based on the results of characterization, polystyrene solution 30% w/v in THF was found to give the

viscosity required for the fingering phenomena to take place. A thickness of fluid is found to play an ignorable role in the structure evolution within a range in which the fractal structures were obtained. Note that the initial thickness plays important role in defining a hydraulic diameter of flow channels thus obtained. Considering these aspects, the initial thickness of 10 microns is maintained. The velocity of separation of 100um/s was maintained to avoid multiple branching observed at higher speeds of separation[137] and get a reasonably repeatable fractal pattern. For the chosen parameters mentioned above, a geometrical characterization of the structures was carried out in terms of a number of fractal generations, length and width of the branches and so on. The following power law relationship was observed to be followed by several structures thus obtained:

$$L = L_o N^{-1.54 \pm 0.09} \tag{5.1}$$

$$W = W_o N^{-0.733 \pm 0.11} \tag{5.2}$$

Where, L is the length of a branch at a given generation, L_o is the length of the parent branch, W is the width of the branch at a given generation, W_o is the width of the parent branch and N is the number of generations.

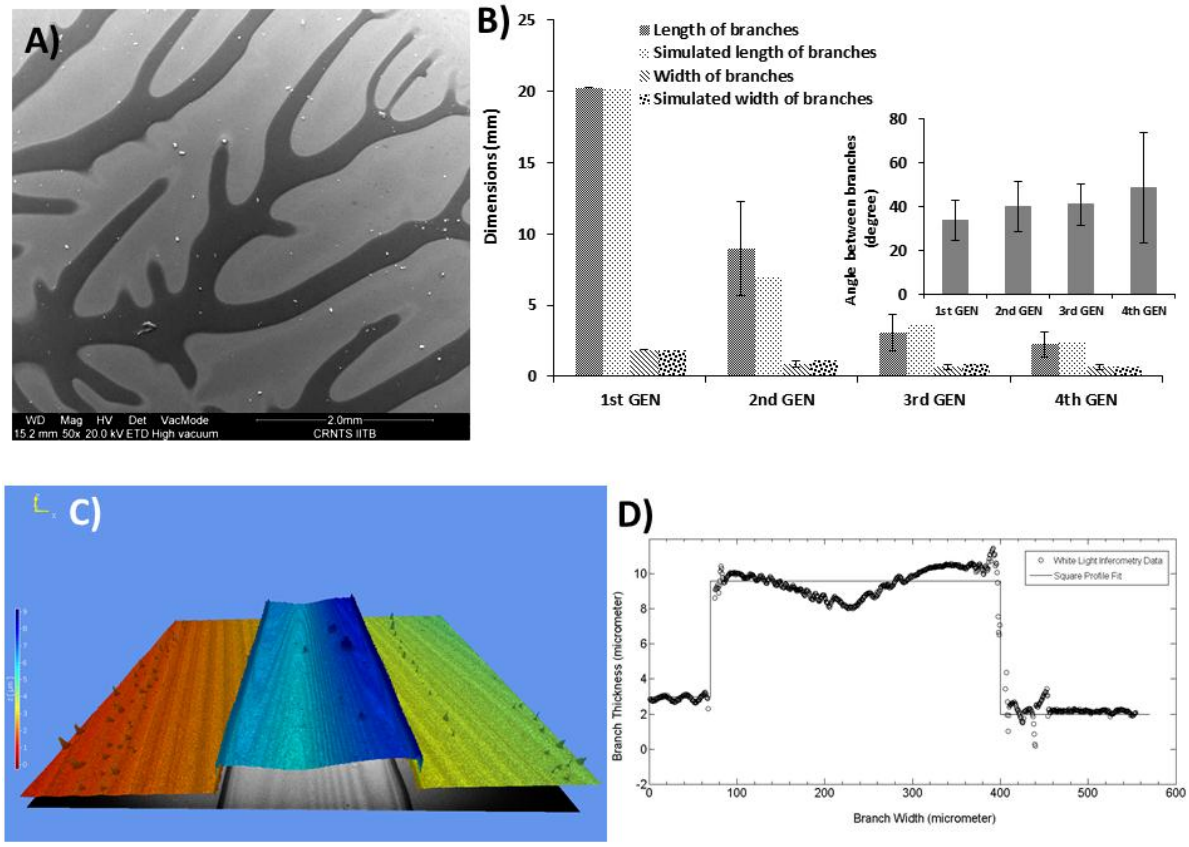

Figure 5.4 A) Scanning electron micrograph of polystyrene fractal-shaped microstructure formed by Hele-Shaw cell B) Graph showing the comparison of variation of length and width of fractal-shaped microstructures with different generations for experimental and simulated data . Graph showing the variation of the angle between the branches of the fractal network with different fractal-generations C) Profilometry image of fractal-shaped microstructure (3rd GEN branch) D) Graph of thickness variation along the width of the fractal-shaped microstructures.

SEM of one of the sets of structures fabricated is shown in Figure 5.4A. Figure 5.4B shows that the experimental variation of length and width of branches in several generations of fractal structure compare well with simulated data from the proposed formulation equation (1) and (2). The average angle between the branches of fractal-shaped geometry was found to vary between 32 to 48 deg. as shown in an inset graph of Figure 5.4B. The angle between the branches lied in the range of angles which allows fluid flow with minimum energy losses. Figure 5.4C and Figure 5.4D present the surface profile of the terminal daughter branch (4th

generation) obtained. Based on profile characterization, average hydraulic diameters of the fractal structures at various points were obtained. Hydraulic diameters were found to gradually vary from 10 microns to few hundred microns. The diameters are lower than those obtained by previous processes (electrostatic discharge, fugitive ink, etc.) reported in the literature[133, 135]. In addition unique feature of the proposed structures thus obtained is gradual variation in the thickness of fractal channels from one end to another which is desirable for lowering resistance to flow while making more area available for connections to nano/microchannel network.

Note that the process of fabrication of fractal-like structures proposed as a part of this paper is scalable in nature. Larger the size of the Hele-Shaw plates and larger the quantity of the liquid solution used, larger will be the overall area and higher will be the number of fractal generations. Moreover, such structures would be spontaneously obtained in a short period of few seconds in an inexpensive setup. These distinct features of this process combined with micro/nanofiber electrospun mesh connectivity make it attractive for several biomimetic applications.

5.4.2. Characterization of electrospun micro/nanofiber mesh

SEM image of a sample polystyrene micro/-nanofibers network deposited on fractal-shaped microstructure (process 1d (iv)) is shown in Figure 5.5A. The graph suggested that diameter of fibers spanned from submicron to micrometer range, with the global average diameter of 1.22±0.34 μm (Figure 5.5B). Further, the random nature of the fibrous mesh was quantified by fast Fourier transforms (FFT) analysis on the SEM images of the micro/-nanofibers network [116]. The angle of spread was calculated from the FFT image was more than 150^{o}—indicating the high level of randomness in the fiber mesh. The randomness, being related to the tortuosity of channel network, will have an impact on the hydraulic resistance and in turn the mass transfer[144].

Researchers[98] have reported earlier (also we confirmed by our initial experiments) that normally the fibers in the electrospun mesh do not fuse with the structure on which they are deposited. To overcome this problem, the following modifications were proposed:

1. The material of fractal structures on which fibers were deposited was same as the fiber material.
2. Solvent chosen for fiber fabrication was common solvent for material used in fractal structure
3. Solvent used in fiber fabrication should have high vapour pressure
4. Parameters (concentration and electrode distance) are adjusted such that the fibers are deposited in 'wet' conditions (meaning without the solvent being fully evaporated from the fibers).

These modifications successfully yielded fused connections between fractal microchannels and electrospun mesh as shown in Figure 5.5C. These fused connections finally enabled, in an inverse pattern, connectivity of fluid networks in the later steps of the process mentioned in Figure 5.2A. Moreover, the inset magnified image (Figure 5.5C) showed the physical integration at the junction of micro/-nanofibers and polystyrene fractal-shaped microstructures. The integration of micro/-nanofibers with fractal-shaped microstructure resulted in a venation pattern analogs to leaves.

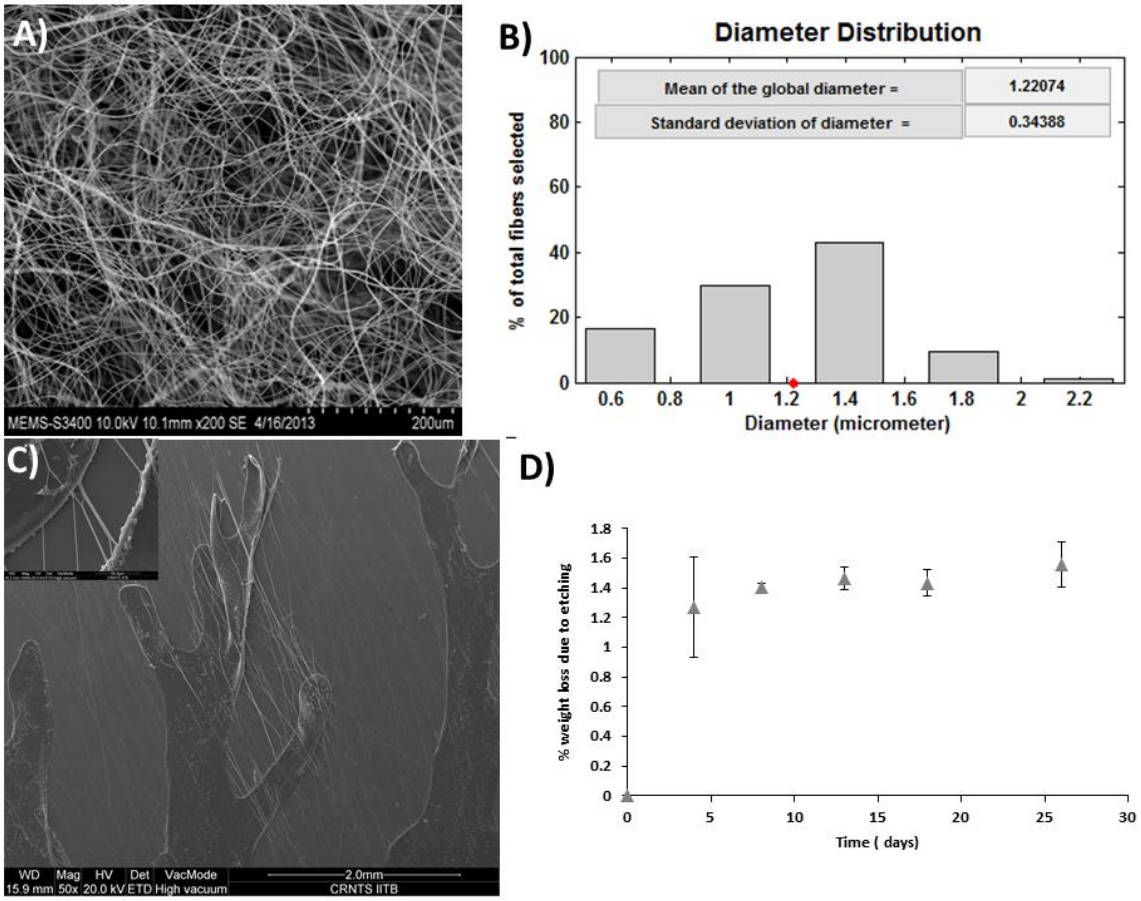

Figure 5.5 A) Scanning electron micrograph of electrospun polystyrene micro/-nanofiber mesh B) Graph showing the diameter distribution of electrospun micro-nanofibers C) SEM of sacrificial integrated polystyrene micro/-nanofibers with polystyrene fractal-shaped microstructures (physical integration of these two microstructure (inset image)) D) Graph showing the variation of % weight loss of polystyrene sacrificial microstructures during solvent etching with time in days.

5.4.3. Characterization of multi-scale channel network in the devices

PDMS was selected as a host material to cast microchannels for several reasons: (a) It is immune, permeable, and swell resistant to solvent DMF used to dissolve sacrificial structures [143] (b) It is permeable to several gasses. This property is required for mass flow applications where the proposed devices would be useful. Percentage reduction in mass of device over time during etching as shown in Figure 3d indicates that the etch rate of sacrificial polystyrene networks in PDMS is low and major etching is achieved in the first

few days. SEM images of a sample obtained after sacrificial etch (Figure 5.2A(vii)) shown in Figure 5.6A-C, illustrate the successful sacrificial etch and connectivity of fractal microchannels to the micro/nanochannel mesh created due to electrospun fibers. Although, sacrificial fibers were continuous in nature, the discontinuous openings suggested that a part of micro/-nanochannels are inside the PDMS, forming a continuous micro/nanochannel network. Further, the diameter analysis (Figure 5.6D) of sacrificial fibers and channels demonstrated that the etching of sacrificial fibers by solvent did not affect the channel dimensions.

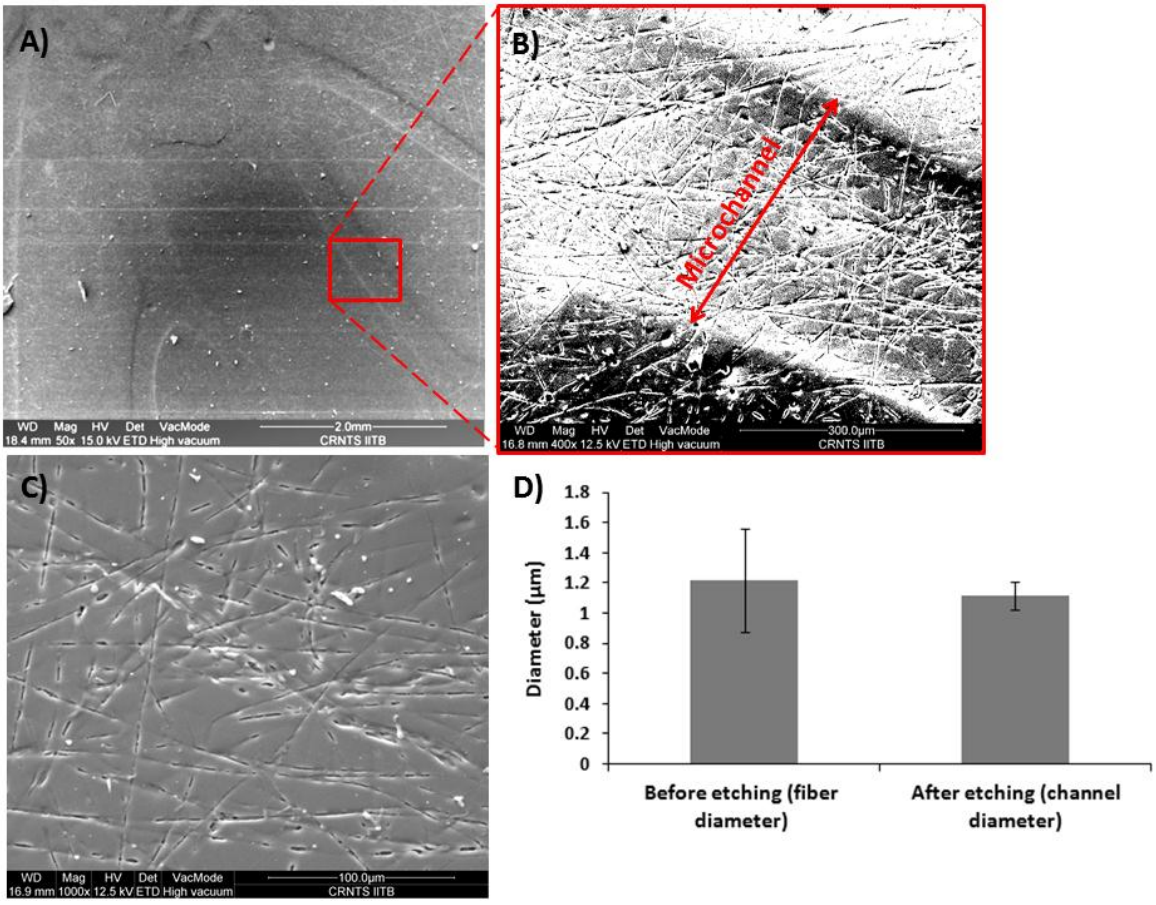

Figure 5.6 A) Scanning electron micrograph of fractal-shaped microchannels with micro-nanochannels network on PDMS surface a) at low magnification showing fractal-shaped microchannels only B) at high magnification showing single microchannel with micro-nanochannels C) at higher magnification showing micro-nanochannel networks only D)

Graph showing the variation of diameter of nanochannels formed after etching with diameter of micro-nanofibers used as sacrificial material.

The images are shown in Figure 5.7 (A and B) demonstrate the presence of red dye in bio-inspired, multi-scale vascularized PDMS matrix. It also illustrates the connectivity and continuity between the fractal-shaped microchannels with the random network of micro/-nanochannels. This reaffirmed the previous observation through SEM imaging about the successful etching of the sacrificial structures from PDMS matrix. Further, microscope imaging at an interface of connection between fractal-shaped microchannel and micro-/nanochannel network in the polymer matrix as shown in Figure 5.7B, demonstrated connectivity between fractal-shaped microchannel and micro/-nanochannel networks and continuity among micro/-nanochannel networks. The connectivity between two types of channel network enabled the dye to reach random micro/-nanochannel network from the rectangular trough via fractal-shaped microchannels by capillary action. Thus, we successfully fabricated nature inspired, multi-scale micro/nanochannel network in PDMS matrices and demonstrated its effectiveness in enabling fluid flow through micro/-nanochannel network via fractal-shaped microchannels.

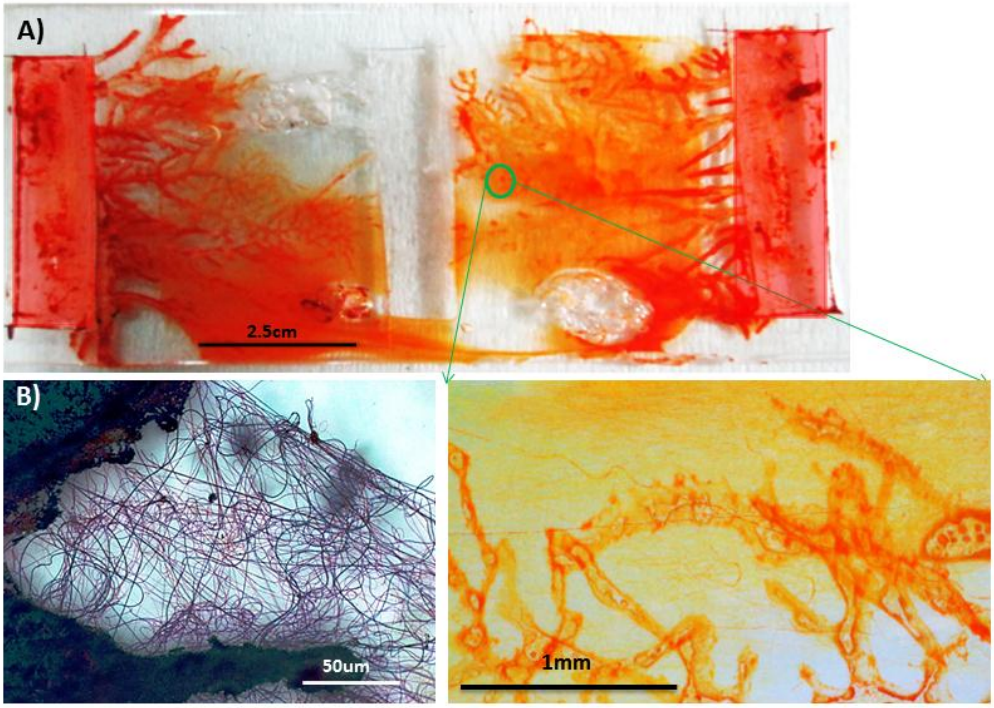

Figure 5.7 Image of PDMS device having integrated fractal microchannel and micro-nanochannel networks A) with dye solution showing connectivity of fractal-shaped microchannels and random micro-nanochannel networks, after dye flow experiment and B) Microscope image fractal-shaped microchannels connected to micro-nanochannels network having dye solution

5.4.4. Study of mass transfer in the fabricated devices

Figure 5.8 shows results of urea diffusion through the proposed fractal connected fiber mesh in comparison with other cases. It can be clearly inferred from the figure that the proposed nature inspired fractal connected channel network is superior in performance for diffusion driven mass transfer. Such increased mass transfer performance in the proposed network is attributed to the participation of the random network of micro/-nanochannels in the diffusion process. Although the presence of micro/nanochannel mesh is seen to enhance the performance because of increase of surface area to volume ratio, the fractal geometry interface to this mesh in the proposed network exhibited nearly 1.7 times better mass transport. Moreover, PDMS matrices having fractal-shaped microchannel net could not demonstrate better diffusion as compared to multi-scale vascularized PDMS matrices

because they suffer from the problem of a large surface area due to micron and meso size of fractal-shaped channel net. Thus, such fabricated nature inspired, multiscale, 3D micro/nanofluidic devices will be useful where heat and mass transfer operations are of primary concern. The process of manufacturing is also apt for micro/nanofluidic devices used in cell culture studies as it can overcome the limitations of small molecule diffusion[145].

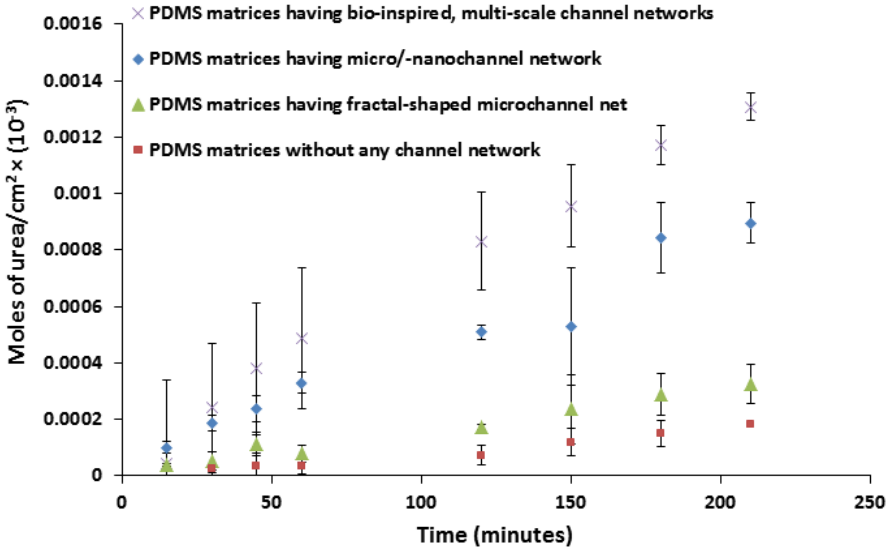

Figure 5.8 Graph showing the concentration of solute (urea) diffusion across different types of vascularised PDMS matrices with time

5.5. Conclusion

The fabrication of nature inspired, 3D micro/nanofluidic devices with multi-scale channel network has immense utility in diverse fields like tissue engineering, biomedical devices, self-healing and self-cooling devices, separation technologies and so on. The conventional lithography-based fabrication techniques are not suitable for fabrication of 3D micro/nanofluidic devices. They suffer from heavy cost of installation and operation, demand for skill full operator, substrate dependence, non-scalability and inability to form multi-scale, 3D morphologies. Our work proposes a novel lithography-less technique to fabricate bio-inspired, multi-scale, 3D channels network in polymer matrices. The method utilizes the principle of removal of sacrificial structures embedded in host polymeric materials using solvents. The sacrificial structures are bio-inspired, fractal-shaped, micro-nanostructures formed by an integration of two scalable, ultrafast, inexpensive micro/nanotechnologies;

electrospinning and controlled lifted Hele-Shaw cells. The above-fabricated 3D micro/nanofluidic devices demonstrated fluidic conductivity under capillary flow and enhanced mass transfer (urea diffusion) capabilities. Thus, the process being amicable for the fabrication of multi-scale morphologies with any material platforms provided the host material remain immune to solvents and the sacrificial material can be transformed to a viscous solution with yield stress property through melt or dissolution in solvents. Further, efforts have to be done to optimize and standardize the fabrication process to develop 3D, micro/nanofluidic device intended for any particular application. Although, capillary filling of fluid was observed in the proposed device, further enhancement and control in volumetric flow can be achieved through a microfluidic component named ‘miropumps’. Therefore, following chapter deals with design and fabrication of bio-inspired passive micropump

6. Chapter 6 Leaf-inspired Micro-pump

6.1. Introduction

The 3D micro/nanofluidics proposed in the previous chapters demonstrated the fluid flow by capillary pumping. However, the driving force and direction of capillary filling are dependent on the interaction between the material constituting the devices and the fluid used during an application. As a result, a small volume of fluid is pumped in devices with limited control over the flow rate is achieved. The precise control over the volume of fluid at a given flow rate is advantageous in a number of applications like advanced drug delivery, cooling circuits in electronic devices, a chromatographic column in chemistry and much more[144]. Therefore, additional components such as micropumps are integrated into microfluidic devices to drive fluid through them. The several engineering principles have been employed to develop micropumps which categorized them under two heads: i) active micropumps and ii) passive micropumps

(i) Active pumps: Active pumps are those that require an external source of energy to operate. These micropumps are amenable for control of pumping rate and temporal behavior of the pumps. These micropumps can be further classified into two classes based on actuation mechanism; a) mechanical micropumps where there is a need of physical actuators or a pumping mechanism to drive fluid in micro/nanochannels b) non-mechanical micropumps that transform non-mechanical energy into kinetic momentum to drive fluid in the microchannels. The incorporation of an external power system to drive fluid increases the complexity of device design and its operation. This increase in control considerably augments the allowable complexity of lab-on-chip fluidic operations. They also suffer from either usage of substantial power requirements or deliver oscillating or pulsating flows that are not desirable under certain conditions. Moreover, the volume of fluid delivered and its rate is significantly dependent on the power source. Some examples of active micropumps are like electrostatic, magnetic, piezoelectric, thermo-pneumatic, electrochemical, electrohydrodynamic, electrokinetic, electroosmotic and magneto-hydrodynamic[146, 147].

(ii) Passive micro pumps: Passive micropumps are those that do not require an external source of energy for pumping of fluid. They are the micro devices that derive their fluid pumping capabilities by the interaction between the microstructural surface and surface

tension of the fluid. The topography of the microstructures and its chemical composition interacts with a small volume of fluid to enable spontaneous movement of fluid in a direction which minimizes the free energy at the interface of a solid substrate, liquid fluid, and air. Such pumping of fluid can be observed during spontaneous filling of fluid in capillaries[120] or wicking of fluid in a porous media[148]. Few attempts at developing artificial passive micropumps were made by Emmanuel Delamarche's group at IBM Zurich and David Beebe's group from the University of Wisconsin at Madison[146]. However, they could not achieve pumping of fluid as observed in trees. In trees, the continuous rise of a large volume of water from roots to the leaves through xylem takes place by virtue of nanocapillary assisted by transpiration. The major advantages offered by these passive micropumps are their low cost of fabrication and operation, a simplicity of design and straightforward implementation, friendly for resource-poor settings. They can also ameliorate the peristaltic/ periodic pumping behavior of active micropumps that is desirable in certain applications. However, the pump is not amenable to the computerized control as the pumping rate changes with time.

Therefore, the passive pump of fluid available in trees can be emulated to design and develop passive micropumps that can overcome the limitation of available active and passive micropumps. The capillary flow based pumps allow 5000-10000 L/day water pumping to above 100 meters in height can be observed in trees. This remarkable feat is achieved majorly by transpiration assisted capillary pumping. During this process, water vapor diffuses under the wake of vapor pressure gradient from interstitial spaces of spongy cells in a leaf to the outside atmosphere via stomatal openings. Consequently, in order to replenish the volume of water lost from the leaves, water is continuously transported towards the leaves by capillary action via xylem tissue of the tree's trunk[149, 150] (Figure 2.3). Therefore, attempts have been made to design and develop pumps that can drive volume of fluid comparable to plants in a controlled fashion; eventually, leading to an increased attention towards transpiration-assisted pumping.

Several attempts have been made to design and develop a synthetic tree to harvest the micro pumping capacity of natural trees, however none of them could either demonstrate the pumping of water to such a height or even attain flow rate close to the natural system. One of the best passive pumping heights achieved by engineered mechanical system was up to

17m[151-154]. Therefore, passive micropumps based on micro/nanofluidics mimicking trees to harness better pumping capabilities have been pursued by recent researchers. The pioneering work on hydrogel-based artificial tree proposed by Wheedle et al. was able to pump fluid at the rate of 0.014 mg/sec. Their artificial tree comprises of two hydrogel representing root and leaves, connected by microchannels that acted as a tree trunk. Their study was primarily directed towards the formation and effect of cavitation on the negative pressure that prevented further pumping of fluid in trees. Thus, their efforts could be indirectly related to the development of tree inspired passive micropumps[39]. The microporous membranes explored by Jingmin Li et al. could be considered as a much direct approach towards the development of transpiration-assisted capillary pump for microfluidic applications. They achieved the controlled flow rate within 0.13–3.74ul/min through changes in parameters such as size and number of micropores in silicon membranes participating in transpiration, temperature, and humidity. Their experimental findings illustrated the role of above factors on fluid pumping rate within a limited range of parameters. Further, they fabricated micropumps functionally and structurally mimicking leaves of plants using agarose gel (resembling mesophyll cells of leaves) and silicon membrane having slit-like micropores (mimic of leaf's stomata) along with other components. These micropumps could exhibit embolism effect of the xylem while performing fluid pumping (xul/min) activities under extreme conditions. They also demonstrated water potential in their micropump to be 72.5KPa which is substantial to lift water to a height of 7m[43, 155]. The above efforts indeed laid the foundation of leaf-inspired micropumps but they were directed towards tailoring the design of microporous substrate to achieve pumping capabilities of micropump. The channel density irrigating the real and artificial leaves also has a profound impact on transpiration-assisted fluid pumping rate as suggested by Xnoblin et al. They highlighted an important observation of optimal channel density, however, their leaf-based device was having arrays of parallel rectangular channels in PDMS (non-porous substrate) which resulted in much lower flow rate as compared to previous researchers[38]. Further, Robert Crawford group delved into the length and diameter of channel irrigating the leaf and area of the leaf participating in fluid pumping as design criteria for leaf inspired micropumps. They could neither observe any appreciable change in fluid pumping rate nor any changes in the attained suction head due to changes in diameter of microchannel irrigating the microporous

membrane. However, the area of porous membrane and pore size had an impact on the pumping rate[147]. The above work demonstrated the dependence of the performance of bio-inspired leaf micropumps on different geometric and ambient parameters, but their studies did not comment on the relationship between volumetric flow rate and above parameters that can be used as a tool for optimizing the fluid pumping capabilities. Further, the designs of micropumps need incorporation of essential geometric parameters. Moreover, improvement in the factors affecting fabrication process will facilitate the development of micropumps with better fluid pumping capabilities. Therefore, the issue of achieving better fluid pumping rate through better design of leaf inspired micropump and understanding its relationship with various geometric and ambient factors was aimed in this thesis.

Therefore, in the current work, we have designed and fabricated leaf-inspired micropumps (LIM) taking into consideration the structural features of leaves (Figure 2.3) to achieve greater pumping rate and obtain high suction head. The method of fabrication proposed here is a simple, inexpensive and scalable process where branch-shaped microchannels in PDMS (representing venation) were integrated into a microporous substrate (resembling stomata) to form biomimetic leaf-like structure. Further, a theoretical and experimental investigation into factors affecting the pumping rate led to formation of mathematical expressions that can be used as guide for the design and fabrication of LIM during an application. Thus, our work will enable the fabrication of efficient leaf-inspired micropumps with tailored geometric properties suited for any fluid pumping applications.

6.2. Materials and Methods

6.2.1. Materials

Microporous cellulose filter paper (Whatman, 90mm Diameter) and Polydimethylsiloxane (PDMS) (Sylgard® 184 silicone *elastomer* kit - *Dow* Corning) were used for fabrication of artificial leaf device. The fluid is a photo-resist ceramic suspension prepared from a monomer HDDA (1, 6 Hexanediol diacrylate) (Sigma-Aldrich). Benzoin ethyl ether (BEE) was added as photoinitiator and phosphate ester (PE) as a surfactant. The ceramic suspension of alumina was prepared as described by Tanveer et al.[156] for preparing fractals-shaped

microstructure on glass substrate. Ethanol and DI water as a working fluid, PTFE tube for tubing and connections.

6.2.2. Methods

6.2.2.1. Fabrication process of leaf inspired micropumps

The fabrication of a leaf inspired micropump is shown in the Figure 6.1

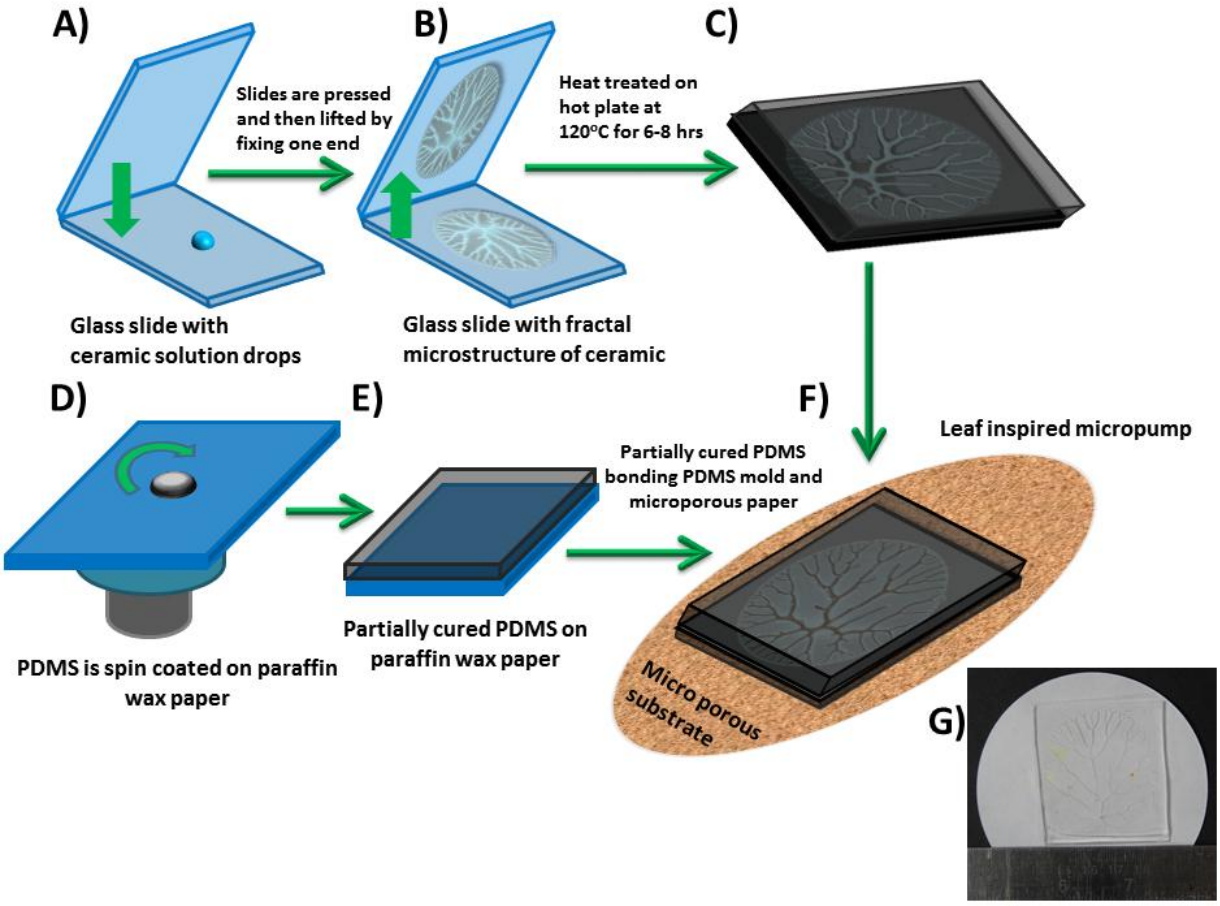

Figure 6.1 showing the schematic of the fabrication process of artificial leaf in a series of steps. The steps are A) placement of a drop of ceramic suspension on a clean glass slide and sandwiching the drop to form a thin film B) angular lifting of the upper slide keeping the bottom slide fixed to form a fractal-shaped microstructure and heating it over hot plate at 120^{o}C C) casting and curing of PDMS over the fractal-shaped ceramic mold D) spin coating of PDMS over the paraffin wax paper E) partial curing of PDMS film on paraffin paper by leaving at room temperature for 24hrs F) bonding of PDMS mold having fractal-shaped

microchannel net with microporous filter paper by sandwiching a partially cured PDMS film G) Camera image of leaf-inspired micropump.

The branching microstructures were fabricated with thoroughly mixed ceramic suspensions [157]. A drop of ceramic suspension was placed on a glass slide inserted in controlled Hele-Shaw apparatus, based on Saffman-Taylor instabilities indigenously developed in the lab[158]. The branching microstructures obtained were heated over a hot plate at 120^{o}C for a period of 24 hours to cure and form a stable mold ready for casting. Further, PDMS solution was prepared by thorough mixing of base and curing agent in 10:1 ratio and degassed before being poured over ceramic mold prepared previously. Thereafter, PDMS was cured over a hot plate at 70^{o}C for 6-8 hours. Then, it was cooled to room temperature and carefully peeled off from the mold to form open branch- shaped microchannel network in PDMS block. In parallel, PDMS was spin- coated at 800rpm for 2-3 minutes on paraffin wax paper. It was left at room temperature for 24 hours to get it partially cured. Thereafter, sticky PDMS film on paraffin wax paper was placed onto microporous filter paper and pressed to allow adherence of PDMS with microporous filter paper. Thereafter, the paraffin wax paper was carefully removed and open branch- shaped microchannels in PDMS block were sealed with PDMS film adhered to the microporous filter paper. The leaf- inspired micropump device as shown in Figure 6.1 (F) was heated at 60 ^{o}C for 1-2 hours to strengthen the bonding between PDMS block with fractal-shaped microchannels and microporous filter paper by an intermediate PDMS film. The control device was fabricated by bonding a PDMS block without any microchannel net with a microporous substrate.

6.2.2.2. Characterization of proposed micropump

The mold of fractal-shaped microstructures was produced by controlled Hele-Shaw apparatus, and fractal-shaped microchannels in PDMS block were taken for structural characterization by camera (sony) imaging. The structural parameters of the samples were analyzed and reported by image processing in MATLAB® 2009a. Further, cross-sections of the micropump's structures and microporous support were characterized morphologically by scanning electron microscopy (SEM). The samples were mounted onto copper stubs and prepared with a gold/platinum coating using a sputter coater for scanning electron

microscopy (SEM) (FEI QUANTA 200, FEI, USA,), operated at 20 kV and 10 kV, respectively. The images were taken at different magnifications for a complete morphological analysis. Further, white light interferometry module of Polytec MSA 500 (Micro System analyzer) was used for surface profilometry to estimate the third-dimensional features of fractal-shaped microstructures. The microporous substrate was evaluated for volume of water absorbed when saturated to determine its absorption capacity. Further, the porosity of microporous substrate was evaluated by gravimetric method[159] and given by the formula

$$\%\, porosity = \left(1 - \frac{\rho_s}{\rho_m}\right) \times 100 \tag{6.1}$$

where ρ_s is the density of microporous substrate and ρ_m is the density of the material of the microporous substrate.

6.2.2.3. Study of fluid pumping rate and pressure head by the micropumps

The leaf- inspired micropump fabricated above were connected at one end of a PTFE tube (length 79cm and internal diameter 2mm) to the entrance of parent channel while the another end of the tube was connected to a reservoir as shown in Figure 6.2.

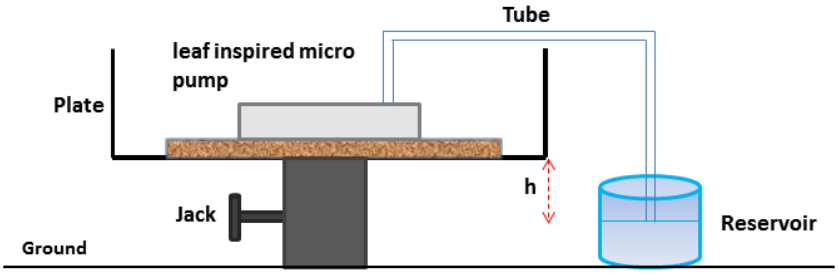

Figure 6.2 Schematic of the set-up to study capillary pumping by leaf inspired micropump.

Initially, the reservoir and micropump were placed at the same level from the ground and thereafter, slowly reservoir level was raised above the micropump by 2 mm to enable water to flow through the pump. The flow of water from the reservoir was continued till the entire microporous paper part of micropump is well irrigated up to saturation level. Thereafter, the reservoir was steadily lowered until the level of micropump reaches the reservoir and thereafter, an air bubble was introduced at the entrance of the tube where an end of the tube

was dipped in the reservoir. This triggers the flow of water from the reservoir to the pump via the connecting tube. The leaf inspired micropump was left in the open air in a clean room environment at 25^{o}C and relative humidity of 50%. Then, the fluid pumping velocity was measured by tracking the movement of the air bubble in the tube when reservoir and micropump were placed at the same height. Thereafter, the platform on which micropump was placed was continuously and slowly raised in steps with the help of jack. At each step, the meniscus of introduced air bubble was followed to track the flow of water in the tube from the reservoir to the micropump for a period of 15 minutes. The process of raising the micropump was ceased when there was no appreciable change in the position of air bubble observed in the tube. Control experiments were carried out with microporous substrate connected to the reservoir via a tube without any intermediate fractal-shaped microchannel networks between porous support and tube. The volumetric flow rate under different pressure head was calculated from the above-recorded data.

6.2.2.4. Study of factors affecting pumping rate by the micropumps

The area of the microporous paper experiencing evaporation is essential for the performance of micropump. Therefore, the spread of fluid in a radial direction in a microporous paper was estimated with the variation of the temperature of the paper and volumetric flow rate of the fluid delivered at the center of the paper through an experimental set-up shown in the figure 6.2. The microporous paper was placed over a hot plate and connected at its center with a PTFE tube. The controlled dye solution in water was delivered by a syringe pump through PTFE tube. The flow rate at which fluid is delivered to microporous paper was varied using a syringe pump from 1ml/hr to 4.5ml/hr at a given temperature at an interval of 1ml/hr. The area of spread of fluid in a porous paper was estimated by measuring the distance between maximum fluid front achieved by radial capillary flow through microporous paper and point of delivery of fluid on the microporous paper when no further increase in the fluid front was observed in the microporous paper. The data of radial distance was estimated at temperature (40, 60, 80, 115, and 150) degree Celsius. Further, the wicking of radial diameter with variation in temperature and flow rate was plotted from the above-recorded data to understand the role of temperature and volumetric flow of fluid on pumping capacity of microporous paper, provided the permeability of the microporous paper remains constant.

The permeability constant of the microporous paper was estimated from maximum height achieved obtained by capillary flow through such paper under 95% humidity.

6.3. Theoretical model of capillary flow through leaf-inspired micropumps

The leaf inspired micropump can be represented by a simplistic model as shown in Figure 6.3A. The microchannel delivers fluid to irrigate the microporous substrate. The fluid drop coming out of microchannel touches the porous support and then spreads in a radial direction by capillary action. Simultaneously, there is evaporation of water from the wetted surface of the microporous support to the outside environment. Under steady state condition, when the volumetric flow rate through the system is constant, the evaporative flux of water from the wetted surface is equal to the volumetric flow rate of water through porous support. The flow rate through the porous substrate is in turn dependent on the volume of fluid delivered by microchannel per unit time, assuming the time of the spread of drop of water coming from microchannel is negligible when compared to the time of flow of water through the porous substrate. This lead to continuous pumping of water from the microchannel connected to the reservoir via an intermediate tube. Other assumptions taken in the model are rate of evaporation from the surface of the microporous paper is uniform, the capillary flow process in the microporous paper is equilibrated with the evaporation from the entire surface such microporous paper is always in saturated state all over its surface and the flow resistance offered by the microporous paper is modelled based on Hagen–Poiseuille flow resistance in a radial flow in a porous media.

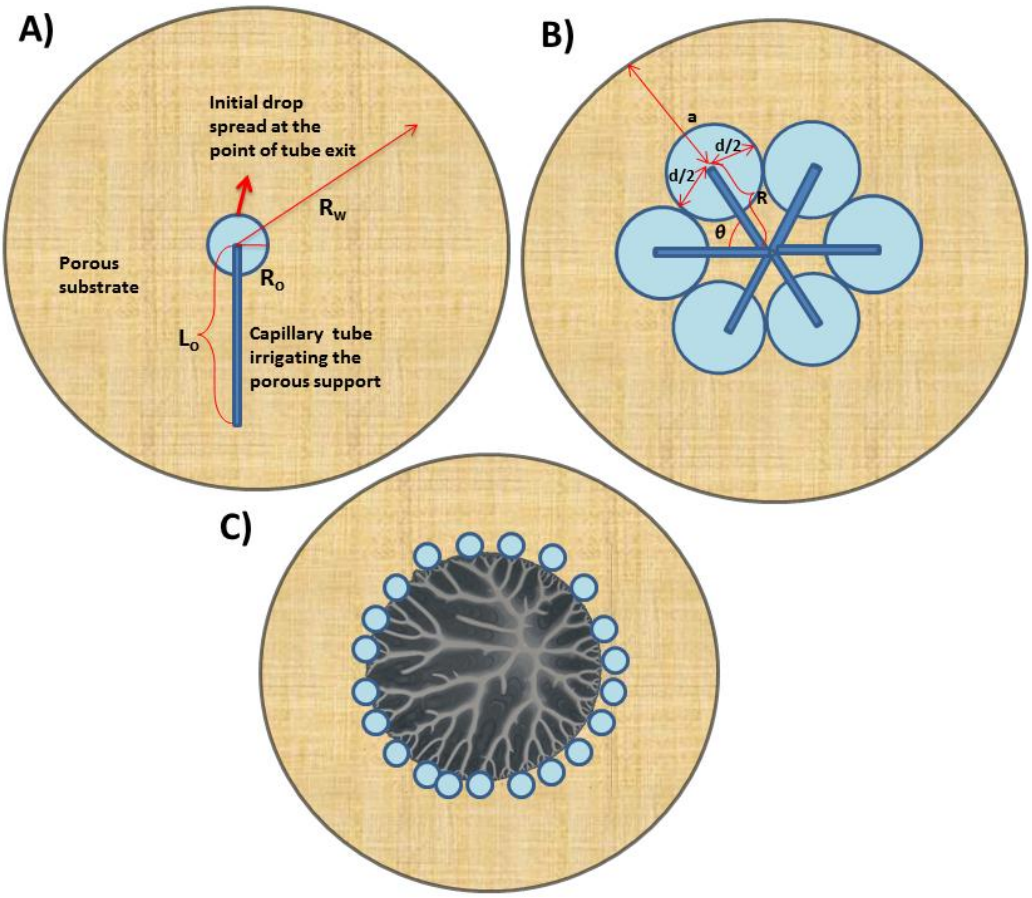

Figure 6.3 Schematic of the leaf inspired micropump where circular microporous paper is irrigated by A) single capillary tube (microchannel) B) a radial array of capillary tube and C) radial array of fractal shaped microchannel net

6.3.1. Maximum wetting radius of the porous substrate of leaf inspired micropumps

Thus, at a steady state, loss of volume of water per unit time by evaporation (Q_e) is equal to the volume of water absorbed by microporous substrate (Q_p)

$$Q_e = Q_p \tag{6.2}$$

The evaporative volume loss per unit time is given by Langmuir equation of evaporative flux[160]

$$Q_e = (P_1 - P_2)\frac{A}{\rho}\sqrt{\frac{m}{2\pi kT}} \tag{6.3}$$

where Q_e is volumetric loss of water from evaporative surface per unit time, A is the effective wetted surface area on the porous substrate participating in evaporation, ρ is the density of water vapour, m is the molar mass, T is the temperature, k is the Boltzmann constant, $(P_1\text{-}P_2)$ is the difference of partial pressure of water vapor on evaporative surface and outside environment.

The volume of water absorbed by microporous substrate can be given by Darcy flow through radial porous substrate

$$Q_p = (P_{atm} - P_c)\frac{2\pi KH}{\mu \ln(\frac{R_w}{R_o})} \tag{6.4}$$

where Q_p is the volumetric flow rate through porous substrate in radial direction, $(P_{atm}\text{-}P_c)$ is the pressure difference driving the flow in porous substrate, H is the thickness of porous support, K is the permeability constant, μ is the viscosity, R_w is the maximum radial coverage length by fluid in porous support while R_o is the initial radius of drop touching the porous support after leaving the microchannel. The capillary pressure exerted by microporous substrate is given by equation [161]

$$P_c = \frac{180^{0.5}\,\sigma\cos(\delta)(1-\varepsilon)}{d\varepsilon} \tag{6.5}$$

where σ is the surface tension of water, δ is the contact angle, ε is the porosity and d is the average particle diameter forming the porous substrate.

Thus, equating equation (6.3) and (6.4) in (6.2) and rearranging the terms, we can get an expression for R_w

$$\ln\left(\frac{R_w}{R_o}\right) = \frac{(P_{atm}-P_c)}{(P_1-P_2)}\frac{2\pi KH\rho}{\mu A}\sqrt{\frac{2\pi kT}{m}} \tag{6.6}$$

As A is the wetted area of the porous support participating in evaporation, it can be expressed in terms of area of porous substrate in radial direction (A_p) and surface roughness $\emptyset_p$ by the expression

$$A = \frac{A_p}{\emptyset_p} \tag{6.7}$$

where

$$A_p = \pi((R_w^2 - R_o^2)$$

Replacing A from equation 6.7 in equation 6.6 and rearranging the terms, yielded an expression

$$\ln\left(\frac{R_w}{R_o}\right) = \frac{(P_{atm}-P_c)}{(P_1-P_2)} \frac{2KH\rho\emptyset_p}{(R_w^2-R_o^2)\mu} \sqrt{\frac{2\pi kT}{m}} \tag{6.8}$$

Now, taking

$$r = \frac{R_w}{R_o} \tag{6.9}$$

and putting in equation 6.8 and rearranging, the expression becomes

$$\ln(r) = \frac{(P_{atm}-P_c)}{(P_1-P_2)} \frac{2KH\rho\emptyset_p}{(R_w^2-R_o^2)\mu} \sqrt{\frac{2\pi kT}{m}} \tag{6.10}$$

Moreover, in the equation (6.10), *(P_1 -P_2)* is the partial pressure difference of water vapor, which can be expressed in terms of ideal gas law by

$$P_1 - P_2 = (C_1 - C_2)RT \tag{6.11}$$

where $C_1 - C_2$ is the concentration of vapor, R is gas constant, (M_1-M_2) is the molar difference and T is the temperature.

$$P_1 - P_2 = \frac{(M_1-M_2)RT}{\pi(R_w^2-R_o^2)h} \tag{6.12}$$

Putting equation (6.12) in equation (6.10), we get

$$\ln(r) = \frac{-(-P_{atm}+P_c)}{(M_1-M_2)R}\frac{2K\pi H\rho\emptyset_p}{\mu}\sqrt{\frac{2\pi k}{Tm}} \tag{6.13}$$

Thus, we can get an expression for the ratio (r) in terms of permeability (K) and Temperature (T) and another parameter which can be twigged to determine the wetted area of the microporous substrate in leaf inspired micropump.

6.3.2. Optimal microchannel density irrigating the microporous substrate

The number of microchannels irrigating the microporous support will determine the amount of volume of fluid delivered to the microporous support. This will determine an initial R_o Value. A radial array of microchannels delivering the fluid to microporous support as shown in Figure 6.3B can be considered as a simple model to determine the optimal channel density.

The volume of fluid delivered by single microchannel is given by

$$dQ_p = \frac{dp}{r}\frac{KH}{\mu}ad\theta \tag{6.14}$$

$$dQ_p = \frac{dp}{\sqrt{x^2+(a-r)^2}}\frac{KH}{\mu}a\frac{dx}{\sqrt{x^2+(a-r)^2}} \tag{6.15}$$

Integrating the above equation

$$\int_0^{Q_{tp}} dQ_p = dp\frac{KH}{\mu}a\int_{-d/2}^{d/2}\frac{dx}{x^2+(a-r)^2} \tag{6.16}$$

solving the above equation, we get

$$Q_{tp}= \frac{dpKHa}{\mu\,(1-\frac{r}{a})}\{\tan^{-1}\frac{d}{2a(1-\frac{r}{a})} - \tan^{-1}\frac{-d}{2a(1-\frac{r}{a})}\} \tag{6.17}$$

rearranging the terms, we get

$$Q_{tp}= \frac{dpKHa}{\mu\,(1-\frac{r}{a})}\tan^{-1}(\frac{2d}{1-4a^2(1-\frac{r}{a})^2}) \tag{6.18}$$

Now , d can be expressed in terms of

$$d = \frac{2\pi r}{n} \tag{6.19}$$

where R is the length of the capillary tube irrigating the microporous substrate and n is the number of such capillary tube. Thus, the equation for the total volume of fluid (Q_p) delivered to the microporous substrate is given by substituting d from equation 6.19 in equation 6.18

$$Q_{tp} = \frac{dpKHa}{\mu\,(1-\frac{r}{a})}\tan^{-1}\left(\frac{4r\pi/n}{1-4a^2(1-\frac{r}{a})^2}\right) \tag{6.20}$$

when (Q_{tp}) is plotted against n, we can obtain optimal value of n

6.3.3. Volumetric pumping rate of the leaf inspired micropump

Further, we can define the volumetric pumping rate by leaf-inspired pump under steady condition by replacing evaporative surface area obtained from equation (6.4). The evaporative surface area can be given by

$$A_p = \pi R_w^2 = \pi R_o^2 e^{(P_{atm}-P_c)\frac{4\pi KH}{\mu Q_p}} \tag{6.21}$$

Then, using the equation (6.21) and equation (6.7) and substituting A in equation (6.3), we get an expression for volumetric pumping rate

$$Q_e = (P_1 - P_2)\sqrt{\frac{\pi m}{2kT}}\frac{R_o^2 e^{(P_{atm}-P_c)\frac{4\pi KH}{\mu Q_p}}}{\rho\emptyset} \tag{6.21}$$

Further, the Q_p is equal to the volume of fluid delivered by the microchannel at steady state condition which is given by

$$P_f = \frac{256\mu L_o}{\pi d_o^4}Q_m \tag{6.22}$$

where $\frac{256\mu L_o}{\pi d_o^4}$ is the resistance (Rf) offered by the channel under Darcy flow through the microchannel. Thus, $Q_p = Q_m$, we can plug equation (6.22) in equation (6.21) to obtain the pumping rate by leaf inspired micropump and given by expression as

$$Q_e = (C_1 - C_2)R\sqrt{\frac{T\pi m}{2k}}\frac{R_o^2 e^{-(-P_{atm}+P_c)\frac{4\pi KHRf}{\mu P_f}}}{\rho\emptyset} \tag{6.23}$$

The pumping rate is directly proportional to square root of temperature; it increases with an increase in temperature and vice-versa. Similarly, the pumping rate follows an exponential decay with the permeability of the porous substrate and resistance offered by microchannel. Therefore, the volume of fluid delivery can be increased while reducing the resistance of microchannel net by application of fractal-shaped microchannel net as shown in Figure 6.3C. The resistance in the fractal channel net is given by expression below[126].

$$R_f = \frac{256\mu L_o}{\pi d_o^4} \sum_{k=0}^{k=n} \frac{\gamma^k}{\beta^{4k} 2^k} \tag{6.24}$$

where μ is the viscosity of the fluid, L_o is the length of parent branch in fractal channel net, d_o is the diameter of the parent branch of fractal channel network, γ is the fractal dimension of length in fractal channel net, β is the fractal dimension of diameter in fractal channel net, *n* is the total number of generations and *k* is the free variable used in summation

As the capillary pressure is inversely proportional to the diameter of the microchannel network and resistance to flow is also inversely proportional to the 4th power of the diameter, therefore in a single microchannel, there has to be a balance between the capillary force and resistance to flow by an optimal channel diameter. However, in the fractal channel net, resistance to flow can be tailored by changes in the summation parameter in equation (6.24) like the fractal dimensions (γ, β) and degree of branching in the network (k)

This might be the reason for the presence of fractal channel networks in natural leaf/leaves in large trees.

6.3.4. Pressure head obtained by leaf-inspired micropumps

At a steady state, when the volumetric flow rate through the system is constant, capillary pressure in the microporous structure (Pc) balances the pressure losses in the fractal channel net (Pf) and tube connecting the leaf and the reservoir (Pt), and suction head (Ps) created by lifting a certain length of water column.

$$P_c = P_f + P_t + P_s \tag{6.25}$$

The pressure drop in the fractal-channel net is given by expression below [126].

$$P_f = \frac{256\mu m L_o}{\pi \rho d_o^4} \sum_{k=0}^{k=n} \frac{\gamma^k}{\beta^{4k} 2^k} \quad (6.26)$$

The pressure drop in a tube connecting reservoir and an leaf-inspired micropump is given by

$$P_t = \frac{f \rho g L v^2}{2D} \quad (6.27)$$

where f is the friction factor, ρ is the density of the fluid, g is the acceleration due to gravity, L is the length of the tube, D is the diameter of the tube and v is the velocity of fluid in the tube

The suction pressure is the pressure exerted by leaf to lift a column of water in the tube and given by the equation

$$P_s = \rho\, g\, h \quad (6.28)$$

where ρ is the density of water, g is the acceleration due to gravity and h is the suction height.

$$h = \frac{180^{0.5}\, \sigma \cos(\delta)(1-\varepsilon)}{\rho g d \varepsilon} - \frac{256\mu m L_o}{\pi \rho \rho g d_o^4} \sum_{k=0}^{k=n} \frac{\gamma^k}{\beta^{4k} 2^k} - \frac{f L v^2}{2D} \quad (6.29)$$

The suction height is obtained by plugging equation (6.5), (6.26), (6.27), (6.28) in equation (6.25) and solving for h. The results obtained were compared with the experimental value while all the values for parameters were experimentally obtained for using them in theoretical analysis.

6.3.5. Dimensionless parameter defining the leaf-inspired micropump

In the micropumps, the pumping rate is dependent on two competing phenomena; 1) the flow of fluid through the microporous and microchannel network guided by geometric and material properties and 2) the evaporation rate of the vapor from the surface of a microporous substrate by virtue of diffusion under steady state condition. Therefore, a dimensionless number can be defined as

$$D_e = \cos\alpha \left(\frac{K/\vartheta}{A_e/D_t}\right) \frac{\sigma A}{k_e} \quad (6.29)$$

where K is the total permeability of the channel net, ϑ is the kinematic viscosity, D_t is the total diffusivity constant of the fluid through porous media, and A_e is the area participating in evaporation. The α is the angle made by fluid meniscus with the substrate. σ is the surface tension, A is the area normal to the flow and k_e is the kinetic energy of the fluid molecule. If the dimensionless number is having a value very much greater than 1, then wetting of porous substrate and flow dominates while the value being less than 1, then evaporation phenomena dominate. Therefore, the above dimensionless parameter can be used to design leaf inspired micropumps suitable for pumping a certain type of fluid. It clearly highlights the properties of porous material and fluid are critical for the design of micropumps.

After plugging the appropriate values of the constants and the variables in different equations shown in Table 6.1, we have estimated the optimal channel density, temperature effect on wetting radii, suction head and volumetric flow rate by leaf-inspired micropump

Table 6.1 Parameters and their value used in theoretical analysis

Parameters	**Values**	**Unit**
Capillary pressure in microporous substrate (P_c)	1642.6	N/m^2
Permeability of microporous substrate (K)	7.175×10^{-10}	m^2
Thickness of microporous substrate (H)	300×10^{-6}	m
Density of water (ρ)	1000	kg/m^3
Porosity of microporous substrate (ϕ)	0.67	Dimensionless
Moles of water on surface of microporous substrate (M_1)	1.25×10^{-07}	Moles
Kinematic viscosity of water (μ)	10^{-3}	m^2/s
Boltzmann Constant (k)	1.38×10^{-23}	$m^2\ kg\ s^{-2}\ K^{-1}$
Molar mass of water in gram (m)	18×10^{-3}	Kg
Avagadro's Number (A)	6.023×10^{23}	Dimensionless
Gas constant (R)	8.314	$J\ K^{-1}\ mol^{-1}$
Number of terminal channels of fractal network (N)	8	Dimensionless
Contact angle water with microporous substrate(C_1)	60	Degree
Contact angle water with PDMS(C_2)	89.7	Degree
Surface tension of water (σ)	72.8×10^{-3}	$N\ m^{-1}$
Number of generations (Gen)	4	Dimensionless
The length of the tube (L_o)	79.8×10^{-2}	m
Diameter of terminal branch of fractal channel net (r)	50×10^{-6}	m
Diameter of the tube (d_t)	2×10^{-3}	m
Fractal dimension of length (γ)	0.69	Dimensionless
Fractal dimension of width (β)	0.754	Dimensionless

Diameter of parent branch of fractal channel net (d_o)	342×10^{-6}	m

6.4. Results and Discussion

6.4.1. Design, fabrication and Characterization of leaf-inspired micropumps

The current paper elucidated a process of design and fabrication of leaf inspired micropumps. These micropumps emulated the structural design of natural leaves at a different length scale to achieve fluid pumping capabilities. It comprised of fractal-shaped microchannel networks in PDMS, mimicking venation system of leaves, to irrigate microporous paper (resembling mesophyll spongy cells having stomata) with fluid. However, the transpiration-assisted micropumps described in literature[39, 43, 147, 155] were primarily microporous membranes or gels irrigated by a single microchannel. The use of single microchannel posed the limitation on the volume of fluid delivered to microporous membranes or gels. Therefore, proposed micropump comprises a fractal-shaped microchannel network to irrigate the microporous paper. These microchannel networks in a PDMS block integrated with a microporous paper also provided structural support to the microporous paper to prevent its collapse under its own weight during fluid flow. Such architecture structurally supported the free standing microporous paper while the micropump in operation was unavailable in previously described pumps. Their pumps needed an extra planner substrate onto which entire micropump assembly was mounted[43, 147]. Thus, this restrains the applicability of these pumps in applications demanding any three-dimensional configurations. Further, the PDMS support had a graded thickness from the point of entry of fluid to the tip of terminal fingers to facilitate its easy integration with an external fluidic port or reservoir. Moreover, the PDMS material being hydrophobic in nature prevented the rapid evaporation of water from its surface analogs to the waxy cuticle present in natural leaves (Figure 2.3). The PDMS material on one surface of microporous paper enabled our leaf-like pump to be amiable for evaporation control via changes in the thickness of PDMS support[38]. Such control over evaporation was only available in previously reported micropumps by changing the size of micropores of a membrane which is a cumbersome process. Eventually, structural design of micropump permitted a unidirectional flow of fluid from the reservoir to the tip of the terminal veins through the assembly of fractal-shaped microchannels.

The method of fabrication of micropumps presented here is a quite simple, scalable and inexpensive process, involving readily available materials. The microfabrication technique, indigenously developed in our lab, enabled the formation of fractal-shaped micro-mold on the glass substrate. In this technique, the phenomena of Saffman-Taylor instability in Helle-Shaw cell were controlled to form a stable, repeatable fractal-shaped mold of ceramic suspension (Figure 6.4A) on a glass slab after heat curing. The parameters for the fabrication of mold of ceramic suspension were optimized for fractal-shaped microstructure. Further, PDMS cast over the mold resulted in fractal-shaped microchannels in PDMS. PDMS material offers several advantages like the ability to bond with a substrate in partially baked state and nearly impermeable to water. Thereafter, image processing of the fractal-shaped structures revealed the structural parameters of fractal shaped microchannels. The depth of the microchannels showed variation across different fractal generations (Figure 6.4A). The graph shows the variation of length and width of microchannels at different generations in a fractal network (Figure 6.4B). The fractal dimensions for length and width of the fractal channel's network are 0.668 and 0.754 respectively.

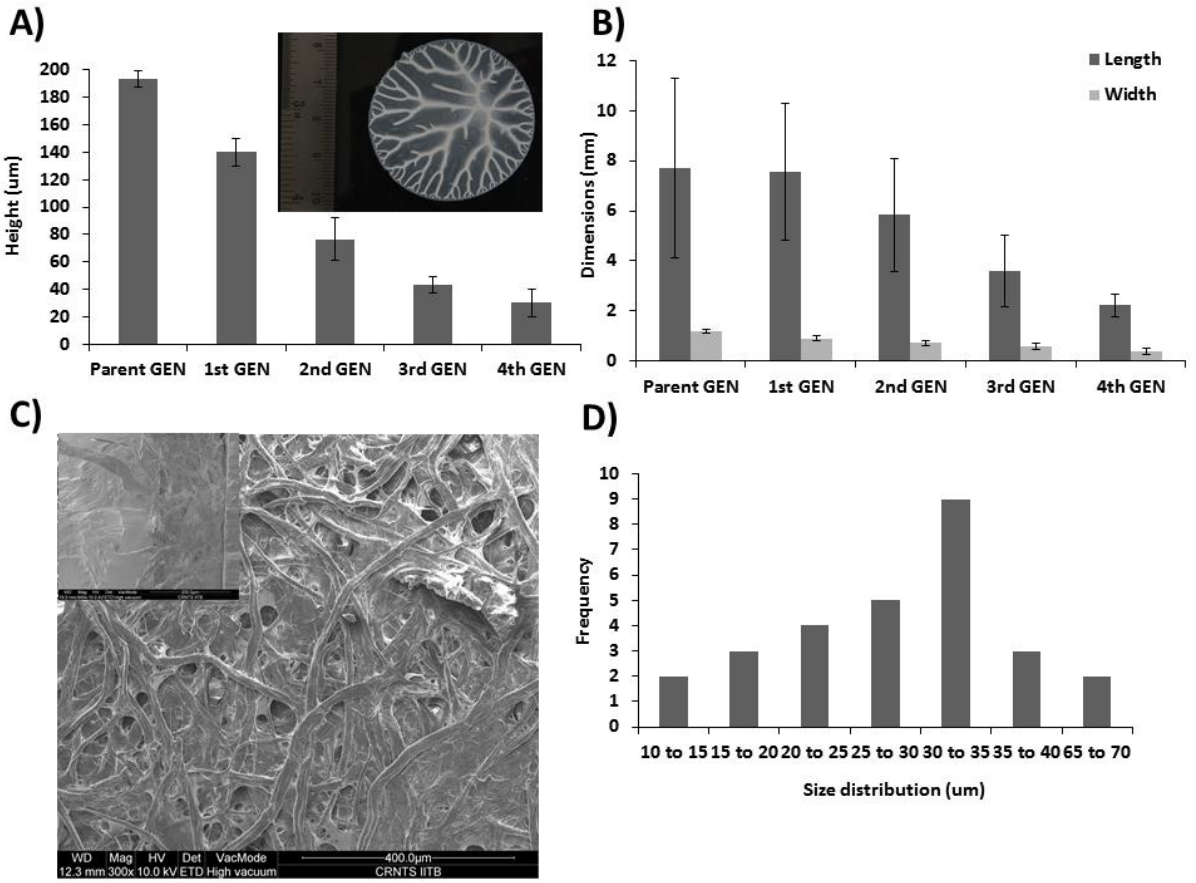

Figure 6.4 A) Graph showing the variation of the height of fractal-shaped ceramic mold with different generations (Inset image shows fractal-shaped microstructure mold of ceramic suspension on glass slide) B) Graph showing the variation of width and length of the fractal-shaped mold with different generations. C) SEM of microporous structure of filter paper (inset image shows the cross-section of the filter paper D) Graph showing the frequency distribution of pore size in a microporous filter paper

The open ends of the fractal shaped microchannels were closed by bonding with PDMS membrane already adhered to the microporous filter paper. The microporous substrate used in the current work is microporous filter paper as compared to microporous membranes or gels used by previous researchers. The microporous filter paper is a free standing porous substrate as compared to the microporous membrane which needs a base support substrate[43, 147]. The differences in the swelling behavior of hydrogels and bonded PDMS might produce strain at their interface, causing delamination during micropump operation. Therefore, the microporous filter paper was adopted for our pump fabrication. In addition,

the microporous filter paper is made up of cellulose material which has a high affinity for water. This will support better wicking by capillary action. Further, SEM of microporous filter paper shown in the Figure 6.4C demonstrated its morphology. The thickness of microporous paper was calculated from the inset image of the Figure 6.4C was ~170µm. Thereafter, the pore-size distribution of the microporous substrate was estimated from their SEM and shown in the Figure 6.4D. The porosity estimated by gravimetry test for the microporous support was 0.66. Further, the absorption capacity of microporous paper was evaluated by absorption studies in which it was observed that 1.082g of microporous substrate absorbed 0.965g of water in 40 seconds. The functional performance of leaf-inspired micrpump was gauged by fluid pumping studies.

6.4.2. Fluid pumping behavior of leaf-inspired micropumps

The fluid pumping experiments with leaf-inspired micropumps demonstrated high fluid pumping capabilities in addition to maintaining the pressure head. The experimental recordings of fluid pumping rates were carried out after the porous support of micropumps was completely irrigated to a saturated condition. This preconditioning was carried out to negate any possibility of the contribution of pumping by absorption through the dry microporous substrate and to bring the system to a steady state condition. At a steady state, volumetric flow through microporous substrate is equal to the evaporative flux of water from the exposed surface area of the substrate. Therefore, the volumetric flow rate can directly qualify to be a measurement of the fluid pumping capacity of micropump. Figure 6.5 represents the steady state pumping rate by micropump at a given pressure head.

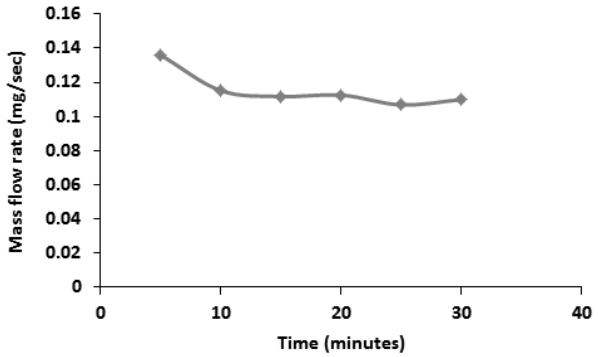

Figure 6.5 Graph showing the variation of mass flow rate during fluid pumping by LIM after steady state

Further, in a horizontal setup, when a micro pump and a reservoir were placed at the same height, the average fluid pumping rate was recorded to be 0.108mg/sec. However, when the experiments were carried out with a stand-alone microporous substrate as a control, it was observed that average pumping rate was only 0.018mg/sec as shown in the Figure 6.6a.

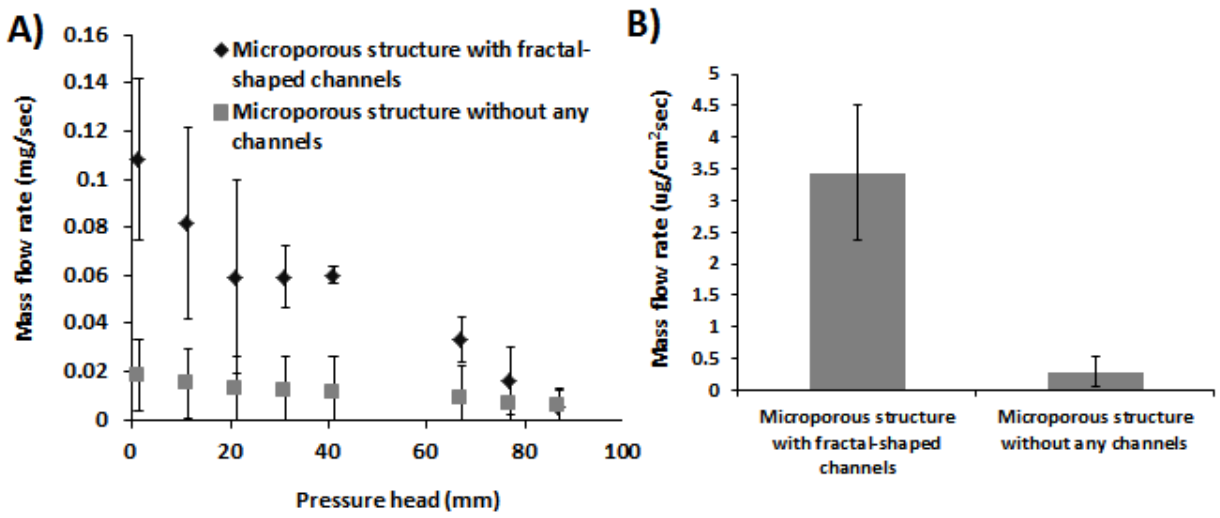

Figure 6.6 A) showing the variation of mass flow rate at different suction head in microporous substrate connected with and without fractal-shaped microchannel net B) showing the comparison of mass flow rate achieved by microporous substrate connected with and without fractal-shaped microchannel net

Although, in either cases, the area and the nature of microporous substrate participating in an evaporative pumping were same, however, an appreciable difference in pumping was recorded. This might be due to additional fractal-shaped microchannel net which irrigates the microporous substrate at multiple locations at the same time as opposed to the single microchannel irrigation system adopted by previous researchers. The micropumps connected to the reservoir were slowly raised with respect to the reservoir to quantify the pressure head it could sustain before the cavitation occurs. It was observed that the fluid pumping rates of LIM were declining 10 times faster than the rate of decline of the fluid pumping rate of the control microporous substrate (Figure 6.6B).

The ability of LIM to sustain pressure head upto 8.8cm is due to delayed caviation introduced by fractal-shaped microchannels. In the absence of smooth transition from the diameter of terminal microchannels to micropores of the microporous substrate, the slightest perturbation during lifting of micropump may have routed air bubble in the fractal-shaped microchannels at the junction of the microporous substrate and fractal-shaped channels. When there was the continuous increase of the LIM height with respect to the reservoir, it was observed that tiny air bubbles migrate continuously towards the tube connecting micropump and the reservoir. During this process, air bubbles continuously nucleate to form a large air bubble till they further prevent entry of fluid from the reservoir to the leaf and thereby, release the suction pressure developed by the micropump. This loss in pressure increases with an increase in the height of the micropump. Nevertheless, as the diameter of the terminal branch of fractal-shaped microchannel net is approximately 30 micron, the volume of fluid dispensed by fractal-shaped microchannels is instantaneously absorbed by microporous substrate surfaces experiencing continuous evaporation of water. The small diameter of terminal branches of fractal-shaped microchannel net interfacing with microporous substrate and larger length of the fractal-shaped channel network arrangement delays the entry and nucleation of air-bubbles. Thus, only after the pressure head of 8.8cm, the fractal-shaped microchannel has no role in sustaining the head and the onus of sustaining the pressure head rests majorly on the microporous substrate of the micropump. This is evident from the nearly similar pumping flow rate at 8.8cm pressure head (Figure 6.6A). The rate of decline in pumping rate of LIM is increased entry of air-bubble and its nucleation with increasing heigh. The above problem is due to the limitation in the fabrication process

which can be overcome by the reduction in the size of terminal microchannels and making its transition nearly continuous with the pore of the microporous substrate. Thus, there is a distinctive role of fractal-shaped microchannel net and microporous support on the performance of leaf inspired micropumps.

The Figure 6.7A summarizes the comparative fluid pumping capabilities reported by previous researchers [39, 43, 147, 154, 155] with the leaf inspired micropumps proposed here.

A)

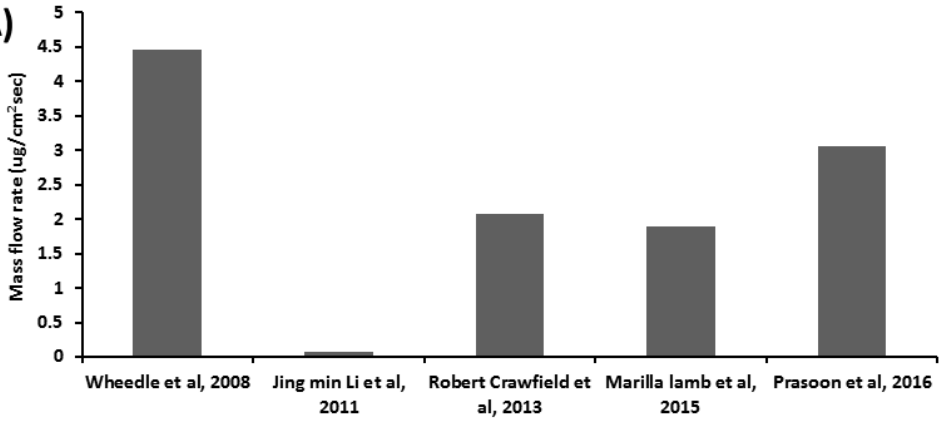

B)

	Type of set-up	Material	Surface area (cm^2)	Temperature (K)	Pore-size(um)
Wheedle et al, 2008	Vertical setup	PMMA hydrogel	3.14	298	10
Jing min Li et al, 2011	Horizontal setup	Microporous M	0.78	298	27
Robert Crawfield et al, 2013	Horizontal setup	Glass fibers	176.7	296.5	7
Marilla lamb et al, 2015	Vertical setup	Ceramic	5.48	298	6
Prasoon et al, 2016	Vertical setup	cellulose	35.34	298	32

Figure 6.7 A) Graph showing the comparison of mass flow per unit area achieved by leaf inspired micropumps developed by previous researchers with the micropump developed in the current work B) Table showing the differences in parameters adopted by previous researchers and current work while evaluating the pumping capacity of the micropump

The comparison over the range of parameters shown in the Figure 6.6B clearly illustrates the nature of the microporous substrate chosen for micro pump fabrication was different from each other. The nature of microporous substrate comprises the size of

micropores present in a substrate, the permeability of the substrate and degree of wettability due to the hydrophobicity of the material. These factors are responsible for volumetric flow rate through these microporous substrates while the micropump in operation at a steady state condition. However, it was found that average pore size of the substrate used for micropumps recorded in literature was found to be around 10um with variation from 7um to 32um. In addition, the degree of hydrophobicity of materials varied from each other but primarily all the materials were hydrophilic only. Thus, the capillary pressure responsible for driving fluid through porous substrate, being the function of pore size and material property, was comparable. Further, the ambient temperature and humidity were also similar which govern the evaporative flux of water from the surface of a porous substrate. Hence, we envisage that the differences in the pumping capacity may be due to differences in participation of surface area for evaporation. Such variances over the participation of surface area for evaporation may be due to the differences in the porosity of the substrate. The hydrogels used by Wheeler et al. were highly porous, hydrophilic material which accounted for their highest pumping capacity per unit area[39]. Although hydrogels demonstrate high affinity for water and permeability, nevertheless a micropump with better performance can be designed and fabricated with other substrates by an inclusion of methods which can allow complete utilization of available surface on a porous substrate. Here, an introduction of fractal-shaped microchannel net leads to the simultaneous delivery of water at multiple sites on the substrate. This ensures an increase wetted surface area of the substrate participating in evaporation, hence the high performance of the leaf inspired micropump. Moreover, the cellulose fibers of the microporous substrate, being hydrophilic, allow continuous absorption of fluid as soon as it exists at the microchannel net also contributes towards the micropump's performance.

6.4.3. Factors affecting fluid pumping behavior in leaf-inspired micropumps

The previous reported bio-inspired micropumps were dependent on the single capillary microchannel delivering the fluid to the microporous substrate. Thus, the volume of fluid to sustain saturated wetting condition of the porous substrate is dependent on the diameter of the irrigating channel and the ambient condition (temperature and humidity). Therefore, the

area of the wetted surface follows a logarithmic relation with an increased volume of fluid delivered to the substrate as shown in the Figure 6.8A at a given temperatures. This indicates that area of wettability does not increase indiscriminately with an increase in the volume of fluid delivered to a porous substrate. Thus, the increase in the volume of fluid delivered to a substrate can be brought about by an increase in the diameter of single capillary but will lead to a decrease in capillary pressure for capillary pumping of fluid. This will also affect the pressure head sustained by the micropump as increased weight of fluid in the channel would lead to early cavitation, resulting in early cessation of the micropump. However, when the diameter is decreased, the capillary pressure will rise along with the hydraulic resistance but the volume of fluid delivered to the substrate would be less. Thus, there has to be a trade-off between the dimensions of capillary channel irrigating the microporous substrate for maximization of fluid delivery and sustaining the pressure head. Therefore, the fractal-shaped microchannel network to irrigate the microporous substrate have channel diameter enough to have greater capillary pressure while minimizing pressure loss due to hydraulic resistance. Further, channel net also delivers increased cumulative volume of fluid to multiple locations on the porous substrate, enough to maintain wettability of surface while functioning.

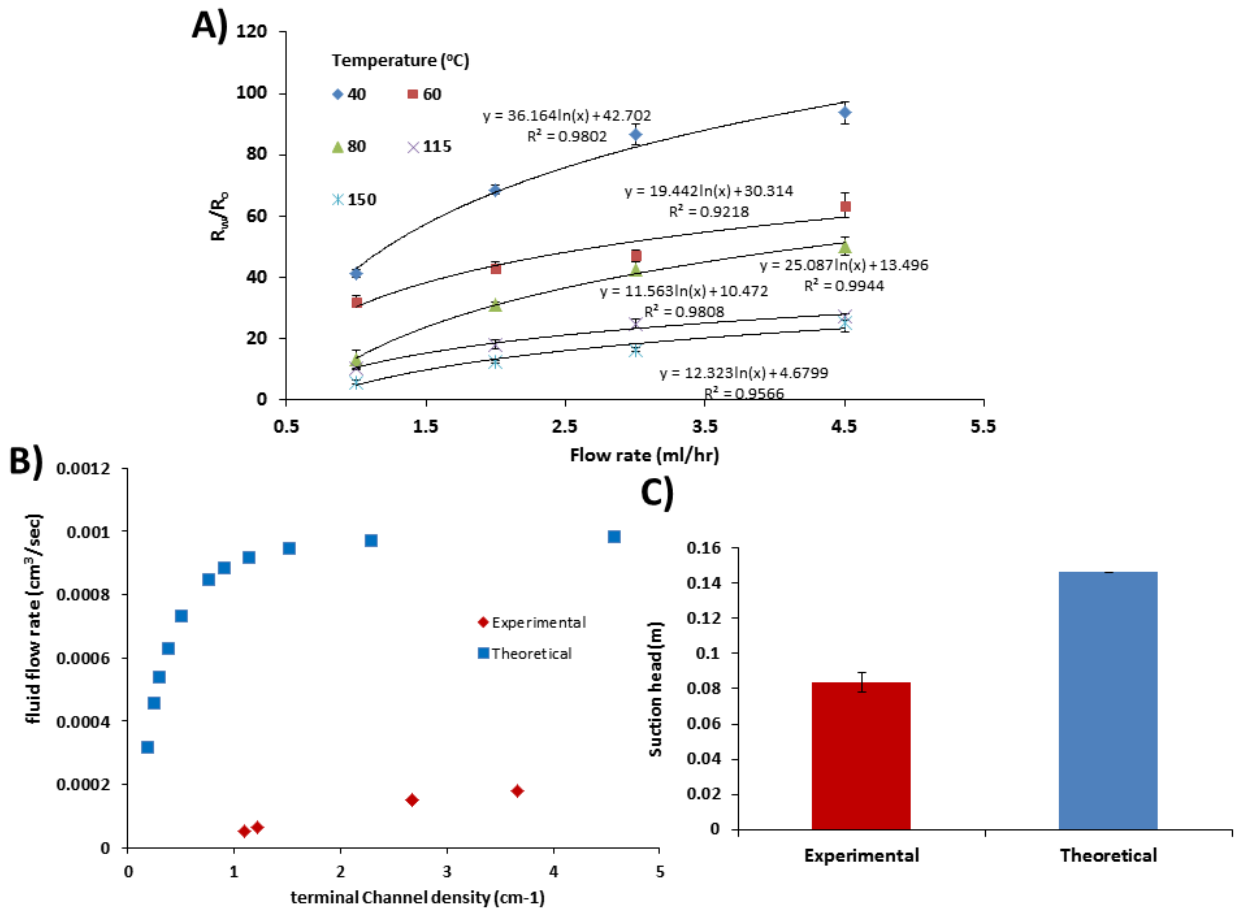

Figure 6.8 Graph showing A) variation of wetting radii of the microporous support when irrigated by the channel at the different flow rate at different temperature conditions B) the experimental and theoretical comparison of volumetric fluid pumping rate at different channel density C) the experimental and theoretical comparison of suction head achieved by leaf inspired micropumps.

It was observed that increase in terminal channel density of fractal-shaped microchannel net leads to an increase in fluid pumping but after a certain threshold channel density, there is a very slow increase in pumping of fluid with the increase in channel density (Figure 6.8B). This observation was in congruence with the limitation on channel density in real and artificial leaf observed by Xnoblin et al.[38]. Thus, the rate of pumping of fluid through microchannel network could not go indiscriminately higher by the mere increase in a number of microchannels irrigating the microporous substrate as shown by the theoretical analysis in the Figure 6.8B. Although, there has been the difference in the values of optimal

channel density for given flow rate as reported by experimental and theoretical findings, the trend of both the graphs appear to be similar.

The role of fractal-shaped microchannel net on sustaining pressure head was calculated to be 8.8cm. The experimental data was compared with the pressure head predicted by the theoretical model and they were found to be similar in order of magnitude as shown in the Figure 6.8C. The experimental result showed less that theoretical prediction due to the discontinuity at the interface of terminal branches of fractal channel net and the microporous substrate. There might be a formation of a liquid bridge under steady state condition which may get perturbed due to slight mechanical vibration during pumping experiments. Such perturbation may allow the air bubble entry in the channels. Thus, continuous entry of micro air bubble will eventually lead to coalescence of these bubbles forming a large air bubble, enough to bring cavitation in the picture. This resulted in cavitation which further prevented pumping of fluid by micropump, leading to low-pressure head sustenance. Thus, for an artificial leaf to be able to pump fluid to a greater height, it should have microporous support 1) with small pore diameter 2) fast absorption kinetics 3) large surface area for quick evaporation and 4) fractal-shaped microchannels with smaller diameter which are bonded with porous support well enough to lower the pressure loss.

The temperatures of the ambiance which guide the diffusion of the water from the micropores of the substrate also play a vital role in the performance of the micropump. The observations of Robert Crawfield et al[147] dismissed the role of channel dimensions irrigating the microporous substrate on evaporative pumping capabilities. Perhaps, this might be because the volume of fluid delivered by any dimension of the microchannel to microporous membrane led to wettability of small portion of the membrane under steady state condition. The wetted portions of the microporous membranes decrease radially from the center, leading to a nearly small surface area of wetted surface participating in evaporation. The evaporation being responsible for pumping of fluid in Robert Crawfield's micropump limits the pumping rate due to underutilization of total surface area of the porous membrane. Therefore, the role of temperature on defining the wetted area of the substrate was studied and it was observed (Figure 6.9A) that wetted area decreases exponentially with an increase in the temperature of micropump operation, provided the permeability of

substrate and volume of fluid delivered remain constant. Such exponential decay in the wetted surface poses a restriction over the operating temperature range for leaf inspired micropumps unless the permeability and material of substrate provide enough window of the temperature range for the pump to be operated. The theoretical model also predicted exponential decay of wetted surface of the substrate with temperature. The Figure 6.9B shows the comparison of experimental and theoretical model and they were found to be in good agreement with each other. The slight differences might be due to assumptions taken in a theoretical model. Eventually, the mass flow rate computed from theoretical model was compared to that of experimental findings (Figure 6.9C) and it was observed that model prediction corroborates well with experiments as mass flow rate was under similar order of magnitude. The difference might be due to the ideal condition assumed in the theoretical model.

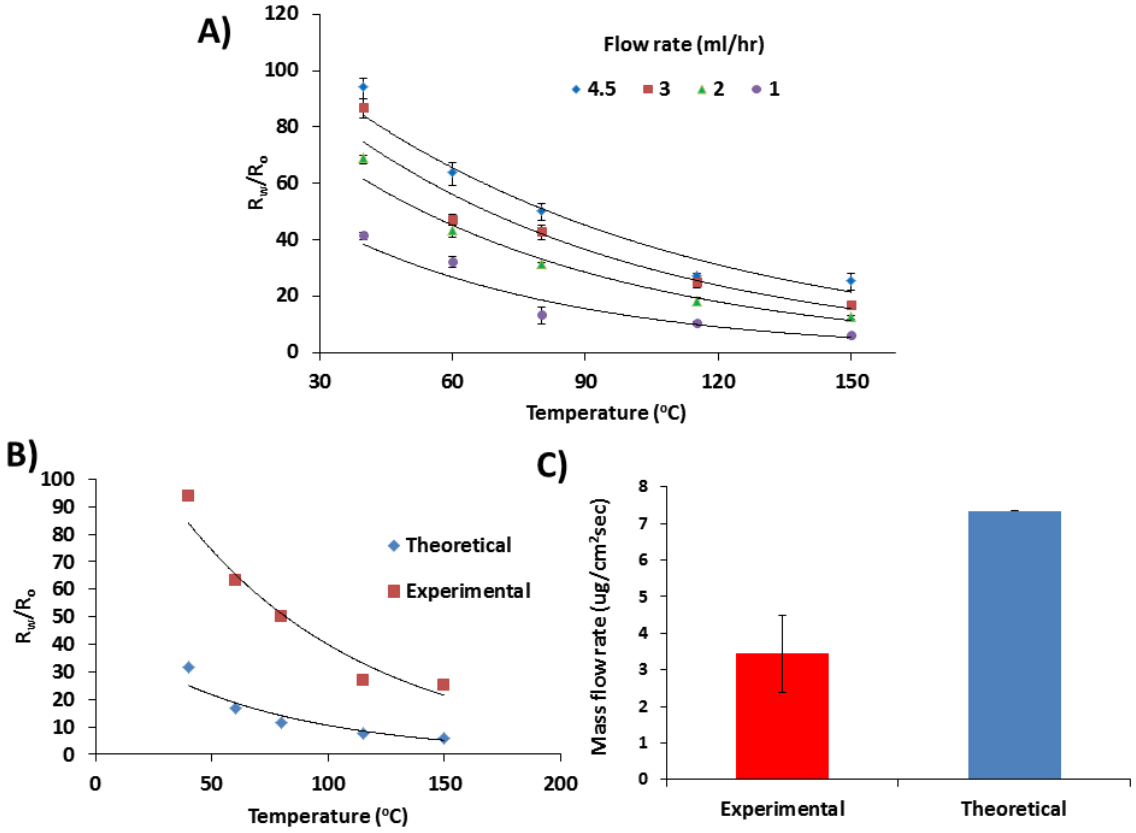

Figure 6.9 Graph showing the A) variation of wetting radii of microporous substrate with temperature at different flow rate B) experimental and theoretical comparison of wetting radii

with different temperature at a particular flow rate C) experimental and theoretical comparison of mass flow rate per unit area in a leaf inspired micropump

Finally, our method demonstrated an easy, scalable fabrication of leaf inspired micropump whose performance is dependent on its design, intrinsic and ambient parameters. Although, above pumping and pressure head sustenance capabilities were demonstrated but still there is a scope for improvement. Thus, the method of enhanced pumping will find application in a number of fields from electronics to bioengineering.

6.5. Conclusion

The capillary pumping of fluid for micro/nanofluidic applications is one of most coveted areas of research. Our approach to achieving meaningful pumping rates rest on the principle of bio-inspiration from leaves of plants. We have designed and fabricated leaf inspired micropumps by a simple, scalable and inexpensive method of fabrication. Our single leaf inspired micropump was capable of pumping fluid at the rate of 388.8mg/hr and could pump the fluid to the height of 8.8 cm before the occurrence of cavitations. Such pumping capabilities are better than or comparable to ones reported in the literature. We demonstrated that fractal-shaped microchannel network is responsible for high pumping rate and microporous substrate for sustaining the suction head. Further, our proposed theoretical model could explain the factors affecting the fluid pumping behavior of micropumps. The dependence of pumping behavior on ambient temperature, the number of channels irrigating the porous substrate, flow rate, and design inspired by leaf for attaining suction head, predicted by the theoretical model, corroborated well with the experimental findings. Thus elucidated few design parameters which need to be considered while developing leaf inspired micropumps. Such pumping rate and suction head are demanded in micro/nanofluidic devices like energy applications, cooling in microelectronic circuits, flow through a chromatographic column and others. This study will enable the development of micropumps with enhanced pumping rate without consumption of energy.

7. Chapter 7 Conclusion and Future Work

7.1. Conclusion

The bio-inspired designs have always guided engineers to develop efficient and effective solutions to various engineering problems. Two of the major problems which consistently appear in a biomedical and chemical field are the controlled energy-efficient flow of fluid and separation of gas/solute from one fluid medium to another. On close observation, the underline physical phenomenon that needs taming is convection and diffusion-based transport phenomenon, which ubiquitous. One of the remarkable gas/solute exchange organs is fish gills. Our study of fish gills at a different length scale enabled us to understand the dimensionless parameters (parametric ratios) and structural features conserved throughout the evolution of fishes. These dimensionless parameters and structural features appeared responsible for enhanced gas/solute exchange in fishes irrespective of their habitat; from fresh water to high muddy water where oxygen partial pressure is abysmally low. Our computational modeling and simulation on the two-dimensional model of the secondary lamella also revealed these parametric ratios from its structural features. The results of finite element simulation were found consistent with theoretical calculations. These parametric ratios and structural dimensions which are critical for gas exchange capabilities of fish gills are few parametric ratios, the thickness of the lamella, the inter lamellar distance, the velocity of water and blood stream, density of vascularisation, length of secondary lamella and arrangement of the secondary lamella. Thus, design and development of any micro-systems by emulating the parametric ratios and structural features of the secondary lamella would possibly lead to developing a highly efficient gas/solute exchange devices.

Fabrication of 3D micro/nanofluidic devices with multi-scale micro/nanochannel network has immense utility in diverse fields like tissue engineering, biomedical devices, self-healing and self-cooling devices, separation technologies and so on. However, the conventional lithography-based fabrication techniques are not amiable to 3D micro/nanofluidic devices. They suffer from heavy cost of installation and operation, demand for skill full operator, substrate dependence, non-scalability and inability to form multi-scale morphologies. Further, recent techniques like solvent or thermal removal of sacrificial micro/nanostructures from a host polymer system described in the literature also experience certain challenges like an ability to form multiscale, bio-inspired, 3D morphologies in

polymer systems. Therefore, we fabricated thin vascularised polymer matrices mimicking secondary lamella. The propose method employs the principle of removal of sacrificial structures embedded in host polymeric materials by solvents. The sacrificial structure is a bio-inspired fractal-shaped micro/nanostructures formed by the integration of two scalable, ultrafast, inexpensive micro/nanotechnologies; electrospinning and controlled lifted heel-Shaw cells. The above-fabricated 3D micro/nanofluidic devices were having nature-inspired, multiscale, 3D vascular network in thin PDMS matrices. These matrices demonstrated fluidic conductivity under capillary flow and enhanced mass transfer (urea diffusion) capabilities through our preliminary experiments. Thus, the process being amicable for fabrication with any material platform provided the host material remain immune to the solvent of sacrificial materials and the sacrificial materials can get easily transformed into a viscous solution through melt or dissolution. Further, the vascularised polymer matrices fabricated by above process will find utility in separating small molecules like urea from two liquid systems.

Further, the performance of 3D micro/nanofluidic devices based on above vascularised polymer matrices during an application depends on the volumetric fluid flow rate through random networks of microchannels. This feature is critical in an application where convection-diffusion-reaction phenomenon governs the application process. Therefore, we fabricated simple vascularized polymer systems by removal of sacrificial, random, electrospun fiber meshes embedded in thin PDMS matrices through solvent etching. Therefore, our investigation of these thin vascularized polymer systems identified few factors affecting the volumetric fluid flow apart from the channel dimension that has already been well researched. These factors are the geometry of the channel network or reservoir interfacing with the random national network and density of nanochannel network, which participates in mass or heat transfer during an application. The theoretical analysis suggested that the branched-shaped geometry of reservoir interfaces well with nanochannel network in comparison to the other regular geometry of reservoirs. This geometry also minimizes the active area occupied by a reservoir on micro/nanofluidic chips while maintaining a high level of nanochannel interfacing. Further, through time-lapse dye flow experiments, we observed an enhanced volumetric flow in micro/nanofluidic networks when connected to the branched - shaped reservoir as compared to a regular rectangular reservoir. This experiment clearly demonstrated the importance of interfacing length of the reservoir on the volumetric fluid

flow rate in micro/nanochannel net. Further, the density of nanochannel network and the degree of tortuosity of the path traced by fluid in a network were found to have an effect on the volumetric fluid flow rate. The empirical relation between the volumetric fluid flow rate and above features corroborated with the theoretical model available in the literature. The relation suggests that the volumetric flow rate is inversely related to the square of tortuosity and directly related to the number density of channel network. Further, the mass transfer was also showed dependence on the density of the channel network to a certain degree, thereafter, the effect of density of channel network on mass transfer become unimportant. Thus, these features need manipulation for better volumetric flow rate in 3D micro/nanofluidic devices, provided the diameter of the nanochannel remains constant.

The fluid flow driven by capillary action in the above 3D micro/nanofluidic devices is well demonstrated in preceding sections. However, capillary driven flow is hardly suitable for certain applications demanding high flow rate. In such case, devices use micropumps to drive fluid through a fluidic circuit with or without using external power supply. The micropump described in the current work is a passive micropump developed by mimicking leaves of plants. They were found to pump fluid at the rate comparable with leaf inspired micropumps reported in the literature. The major advantages of the manufacturing processes of our leaf inspired micropumps are its simplicity, scalability, and amalgamation of two inexpensive processes; spin coating technology and controlled lifted Hele-Shaw cell. Moreover, material and manufacturing expenses are substantially less than micropumps manufacturing processes offered by other researchers. These micropumps were not only able to emulate the structural features of leaves and but also could pump fluid at a high rate while sustaining pressure head before cavitation. The pumping mechanism proposed is a coupled phenomenon of capillary filling and evaporation. Further, the experimental and theoretical investigation suggested that the temperature of the ambient, density and pattern of the vascular network and flow rate as the factors responsible for volumetric pumping of fluid by experimental and theoretical methods. A dimensionless parameter proposed will act as a guide for the design and fabrication of scalable leaf-inspired micropumps. Thus, tailoring the parameters of micropump will further escalate its pumping capabilities. Such micropumps will have applications, enhancing the fluid flow through 3D micro/nanofluidic devices. The

proposed method of fabrication offers several advantages as compared to the fabrication of devices through conventional lithography, as summarized in the Table 7.1.

Table 7.1 Comparative analysis between our method and lithography-based techniques

	Lithography[162-164]	**Proposed method**
3D structuring	Difficult and possible only with stacking of 2D/2.5D layers, monolithic 3D fluidic network not possible	Monolithic 3D fluidic network possible with ease
Speed of manufacturing	Medium to low	Medium, limited only by speed of etching of sacrificial structures
Materials	glass/silicon/polymers	Polymers/ceramics
Expertise needed	Highly skilled personals needed	Moderate
Bio-inspired channel networks	Quite challenging, possible with huge investment of time and labour, generally produce rectangular cross-sectioned channels	Very easy
Product scalability (volume and size)	less scalable, restriction over the size of the device	Highly scalable, possible to fabricate large size fluidic devices in high volume
Channel size resolution and variation	Few nm to microns; fabrication allow only channels with dimension over a limited range in a single device	Multi-scale channel network possible, dimensions ranging from 100nm to few mm in a single device
Cost of manufacturing	High due to heavy capital and consumable cost, generally greater than $1million	Very less due to low capital and consumable cost, less than $3 thousand

In summary, the work focused on the design and fabrication of bio-inspired micro/nanofluidic devices through scalable micro/nanotechnologies for enhanced fluid flow and study of factors affecting the fluid flow through such devices to exploit them for mass transfer operations. Thus, the work will enable design, fabrication and development of 3D micro/nanofluidic at large-scale for applications in biomedical and chemical industries demanding heat and mass transfer.

7.2. Future work

In future, biomimetic, scaled-up fish gill device is a possibility of incorporating the structural parameters laid down by computational and theoretical studies in the design of micro/nanofluidic devices. Further, it is possible in future to stack thin, bio-inspired, multi-scale, vascularized polymer matrices mimicking the stacking pattern of the secondary lamella in fish gills while incorporating the parametric ratios to design and develop better, scalable gas/solute exchange microdevices. Such devices can act as an extracorporeal membrane device in artificial lungs, a site for oxygenation of blood or as act as a dialysis chamber of kidney dialyzers, a site for blood filtration. They have other applications like filtration, separation employed in chemical industries.

One can improve the efficiency of leaf-inspired micropumps developed in the current work by changing the size of micropores in microporous material, using a hydrophilic material for developing fractal-shaped vascular networks and increasing the bonding between the microporous material and polymer block having fractal-shaped microchannel net. These micropumps have potential to drive fluid in a microelectronic circuit for effective cooling without an aid of external power source. They can also be used in solar distillation plant for water desalination and purification mimicking the hydrological cycle, developing inexpensive water purification systems.

Appendix

Appendix- A

(Conference Paper)

The conference paper titled ` Multiscale fabrication of scalable biomimetic 3-D, integrated micro-nanochannels network in PDMS for solute exchange' was presented at the 11th International Conference on Micro Manufacturing (ICOMM) Irvine, Orange country, USA from 29th to 31th March 2016.

Multiscale fabrication of scalable biomimetic 3-D, integrated micro-nanochannels network in PDMS for solute exchange

Prasoon Kumar[123], Prasanna S Gandhi[2], Mainak Majumdar[3]
1 IITB-Monash Research Academy, Powai, Mumbai, Maharashtra-400076, India
2 Suman Mashruwala Advanced Microengineering Laboratory, Department of Mechanical Engineering, Indian Institute of Technology Bombay, Powai, Mumbai, Maharashtra 400076, India
3 Nanoscale Science and Engineering Laboratory (NSEL), Department of Mechanical and Aerospace Engineering, Monash University, Clayton, Melbourne, Australia

Abstract

Integrated micro-nanochannel networks in fluidic devices are desirable in a number of applications ranging from self-healing/cooling materials to bioengineering. The conventional micro-manufacturing techniques are capable of either producing microchannel or nanochannel networks for a fluidic application but lack proficiency in the production of integrated micro-nanochannel network with a smooth transition from micro-to-nano scale dimension. In addition, these techniques possess limitations such as heavy initial investment, sophistication in operation and scale-up capabilities. Therefore, the current paper demonstrates the combination of micro/nanotechnologies to design and develop a biomimetic 3-D integrated micro-nanochannel network in PDMS device for solute exchange. We have used a 3-D printer, a scalable technology, to design and manufacture micro-mold having fractal-shaped features. Further, electrospinning was used to deposit nanofibrous network on the fractal mold. Subsequent micro-molding with PDMS was used to obtain fractal-shaped microchannels integrated with embedded nanofibers. Henceforth, solvent etching of nanofibers followed by bonding of thin PDMS membrane generated by spin coating to open end of channels leads to the formation of functional microdevices. These PDMS devices mimic the natural vasculature of a living system, where fractal-shaped microchannels will assist in efficient fluid flow and the site of nanovascular network participates in heat/mass transport operations. Further, dye flow propounds the functionality of such devices. Our study hence proposes a simple and scalable hybrid microtechnology to fabricate fluidic devices having multiscale architecture. This will also facilitate the rapid fabrication of microfluidic devices for biomedical, diagnostics, sensors and micro-TAS applications.

Keywords: 3-D printing, electrospinning, solvent-etching, nanovascularization, micro-molding.

1. Introduction

Integrated three-dimensional micro-nanochannel networks in a polymer matrix have become significant owing to their potential applications in filtration, self-healing and cooling materials, tissue engineering and regenerative medicine [1]. However, technologies are available to fabricate such polymer system with either nanoscale or microscale dimensions [2]. With the advent of additive micromanufacturing techniques, it has become possible to generate microstructures with resolution up to 1µm [3-4]. Moreover, challenges associated with successful integration of different micro/nanomanufacturing techniques are their different operating conditions, compatibility with substrate materials and capabilities to form structures with a smooth transition from a meso-to-micro-to-nano domain. Further, even if such criteria are met under certain conditions, it does not compile a method to produce integrated micro-nanostructures in a polymeric substrate on a large scale [5]. In addition, these fabrication techniques require huge investment for the installation and supporting infrastructure. Further, being highly sophisticated techniques; they require high technical expertise, time and resources; therefore their tailor ability to suit any hybrid micro manufacturing is quite challenging [2]. Although other recently explored techniques like direct self-assembly of fugitive inks, electrical discharge, have demonstrated the formation of vascularization in polymer matrixes with much ease, their control over the dimensions of vascular channels and scalability remain an intrinsic limitation [6-8] [76, 135] [76, 135] [76, 134] [76, 133] [76, 133] (Huang, Kim et al. 2009, Esser-Kahn, Thakre et al. 2011). Therefore, recent researchers have demonstrated the application of two scalable additive technologies; 3-D printing and electrospinning to generate integrated micro-nanostructure to be used as a scaffold for tissue regeneration [9-10]. However, no such attempt has been made to the best of our knowledge to integrate 3-D printing and electrospinning to generate micro/nanofluidic devices for lab-on-a-chip or organ-on-a-chip applications. Hence, in the current study, we have integrated scalable micro-manufacturing technologies: electrospinning, 3-D printing, micro-molding and solvent etching of sacrificial structures in an innovative way to design and develop a PDMS based micro-devices having integrated micro-nanochannel networks and a thin membrane for convection-diffusion studies. These devices mimics natural vasculature of living beings where fractal-shaped microchannel network assist in efficient fluid flow, the site corresponding to nanovascular network participates in heat/mass transport operations and thin membrane assists in heat/mass transfer operations.

2. Materials and method

2.1. Materials

Polydimethylsiloxane (PDMS) (Sylgard® 184 silicone *elastomer* kit - *Dow* Corning) was used for fabrication of micro/nanofluidic devices. Polystyrene (PS) 192 kDa (Sigma-Aldrich Pvt. Ltd., India) was used for the fabrication of electrospun micro/nanofibrous mesh. N, N, Dimethylformamide (DMF) (Ajayx PVT. Ltd, Australia) was used as solvent for PS solution and sacrificial etching of micro/nanofibrous structures, Polycarbonate (PC) (Stratasys, Eden Prairie, MN, USA) was used to fabricate 3-D molds with 3-D printer, Fluorescein Dye (Sigma-Aldrich Pvt. Ltd., India) was used as dye in dye flow experiments. Ethanol

(Changshu Yangyuan Chemicals, China) was the fluid driven from fractal-shaped microchannels to micro/nanochannel networks during dye flow experiments.

2.2. Methods

Electrospinning (designed and assembled in the lab) was used to fabricate polystyrene nanofibrous mesh [11]. For electrospinning, a 15% w/v of polystyrene solution was prepared in DMF. The solution was stirred overnight to form a homogeneous solution before electrospinning. The process parameters were optimized to generate fibres with 1µm diameter: voltage – 10KV, the distance between collector and spinneret – 12cm, the flow rate of the solution by syringe pump – 0.5ml/hr, deposition time 1–2 minutes, and needle gauge of 24G. The micro/nanofibrous meshes of polystyrene were obtained on aluminum foil. A part of the sample was taken for imaging and characterization by scanning electron microscope (SEM) while other parts were used in the further fabrication process. In parallel, mechanical designs of the device mold with fractal-shaped microstructures were developed in Pro/ENGINEER Wildfire 4.2 and subsequently, they were used as an input to 3-D printer to generate structures in polycarbonate (Objet. Eden260V™, Strategy's, Eden Prairie, MN, USA) (Figure 2). The mold was carefully cleaned with ethanol and water in a water bath sonicator. Further, electrospun nanofibrous mesh deposited on aluminum foil was carefully transferred to the mold.

In order to avoid displacement of fibrous mesh during the micro-moulding process by PDMS, few drops of ethanol was added to the fibrous mesh placed in a mold to enable stiction of fibrous mesh upon evaporation to the mold structure (Figure 1). Thereafter, PDMS (10:1) was poured into the mold and cured over a hot plate at 70^{o}C for 6-8 hours. After cooling of the mold, PDMS devices having embedded nanofibrous mesh were placed in a DMF bath and stirred slowly to enable etching of fibrous structures for several days. After an etching process, an inverse replica of porous non-woven electrospun mesh integrated with fractal-shaped microchannels was created in a cured PDMS block of 5mm thickness.

Further, PDMS solution with base and curing agent in 10:1 was prepared and spin coated over paraffin wax paper with a spin coater (Spin 150-v3, SPS, Europe, Inc) with rpm varying from 1000 rpm to 5000 rpm. The coated films were cured at room temperature (25^{o}C-30^{o}C) for 48 hrs. The thickness of PDMS membrane was estimated by a screw-gauge. Thereafter, the open end of the PDMS device having integrated micro-nanochannel networks was plasma bonded to PDMS membrane generated previously on paraffin wax paper in a plasma cleaner (Basic Plasma Cleaner PDC-32G, Harrick Plasma, USA) at 1mbar for 20second. The device was heated at 70^{o}C on a hot plate for 20-30 minutes to further strengthen the plasma bonding. Thereafter, few samples were taken for SEM and optical imaging to characterize the dimensions of different channel features in the device. The dimensions of the different channel features were estimated by image processing in MATLAB 7.4. Further, holes were punched, the tubing was connected to the above PDMS device to be used for fluid flow by capillary action.

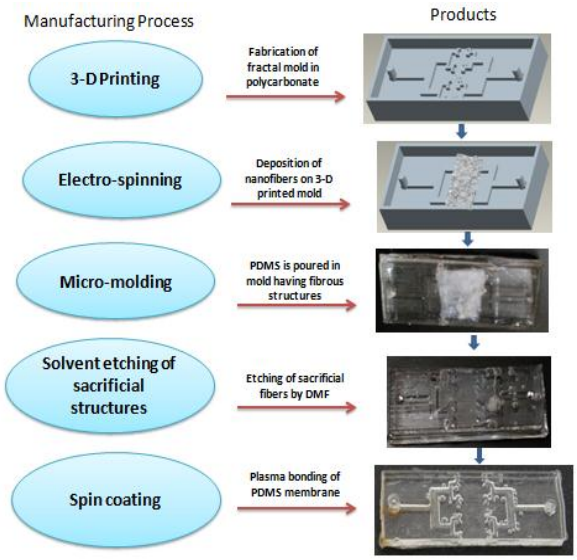

Figure 1 Schematic of process of device manufacturing

3. Results and discussion

The computer aided design (CAD) models of the fractal-shaped microstructure (Figure 2A) were created till second generation branches. The model assumes the width of the fractal structures from parent to 2nd generation varies from 1mm to 0.447mm following the $W = W_oN^{-0.733}$ while length varies from 5mm to 0.921mm following the $L = L_oN^{-1.54}$. However, when the final mold was fabricated with 3-D printer in polycarbonate, it was observed that the dimensions of the structures were nearly same for parent and 1st generation fingers (Figure 2B) while the morphology of 2nd generation fingers tampered. This might be due to resolution limitation of the 3-D printer. Further, the height of the fractal structure came around 270 µm (Figure 2B) after fabrication while CAD model input was given the height of 250 µm.

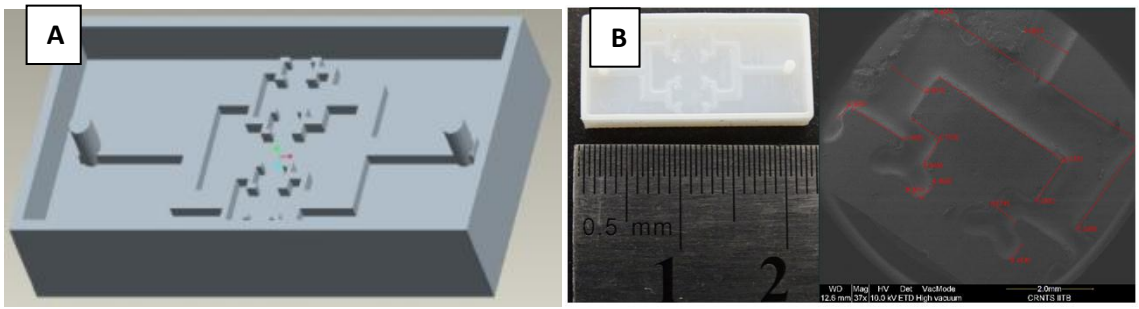

Figure 2 A) ProE design of mold B) 3-D printed mold in polycarbonate (Top left) and SEM image of mold with feature dimensions in millimeter (right)

Further, the SEM of nanofibrous meshes revealed the dimension of fibers to be 1.304±0.318µm (Figure 3A) while SEM of PDMS devices showed successful solvent etching of polystyrene nanofibrous mesh to generate nanochannel network (Figure 3B). The dimensions of channel network were in corroboration with the dimensions of micro-nanostructures used in creating an inverse replica in PDMS. This suggested the non-swelling

activity of DMF on PDMS. The PDMS device having open-ended fractal-shaped microchannel with open-ended integrated nanochannels were covered by PDMS membranes. The SEM of a cross-section of PDMS device bonded with the thin membrane was taken at two different positions. The thickness of membrane bonded to device come around 38µm and figure 3C suggest the continuous integration of membrane with PDMS by plasma bonding. Further, SEM of cross-sectioned PDMS device at nanochannel networks suggested that nanochannel layer spanned around 166µm (Figure 3D). However, the thickness of membrane estimated came around 51µm. This might be because of difficulty in demarcating the point of joining of PDMS membrane and PDMS device.

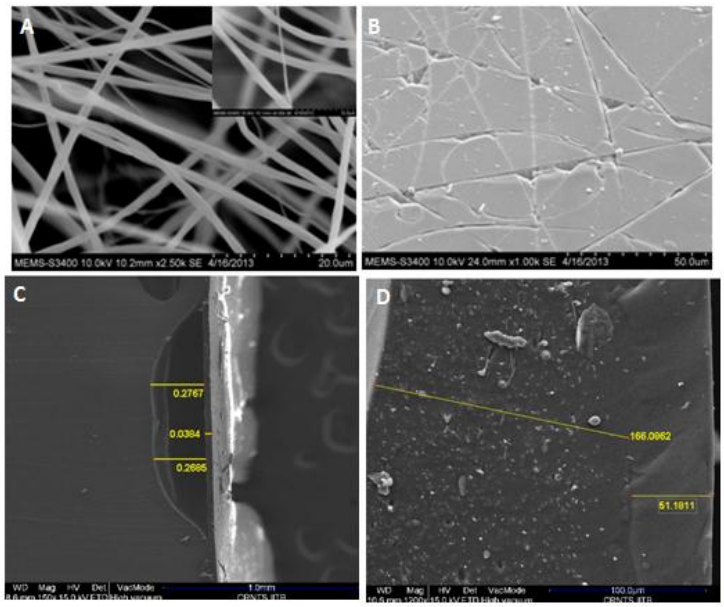

Figure 3 SEM image A) electrospun nanofibrous mesh B) nanochannel network in PDMS C) cross-section of fractal channel with membrane D) cross-section of nanochannel network with membrane

These membranes were spin coated with PDMS solution on a paraffin wax paper and cured at room temperature before being plasma bonded with PDMS devices (Figure 5). The presence of paraffin wax enabled easy transfer of membrane to PDMS device. The graph in figure 4A suggests the further lowering of membrane thickness by increasing the speed of rotation during spin coating. However, very thin membranes may be difficult to transfer from paraffin wax to PDMS device. This process enabled fabrication of membranes with a thickness as low as 15µm. Further, spin coating over paraffin film may assist in the generation of large-sized thin membranes and easy integration with PDMS devices during scale up device fabrication.

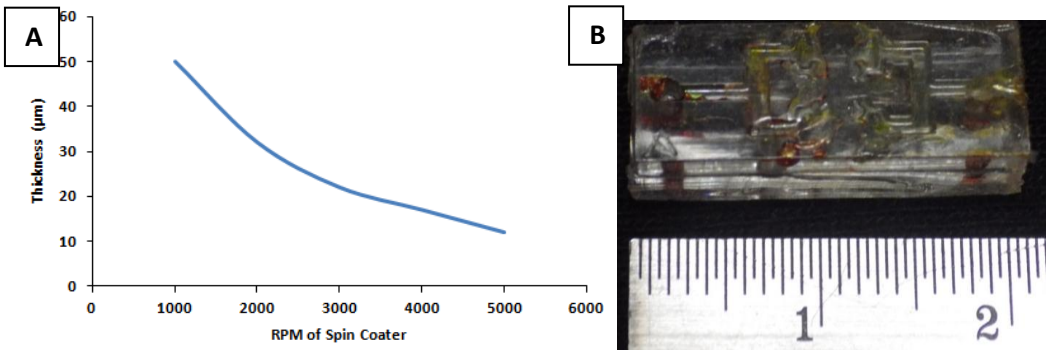

Figure 4 A) Graph showing the variation of thickness of membrane with speed of rotation of spin coater B) Image of Dye presence in channels of PDMS device

Further, Fluorescein dye in ethanol was used as a fluid and flow experiments were carried out by capillary action. It was observed that the dye could easily flow in the fractal fingers as shown in figure 4B but we could not observe the dye solution in nanochannel networks. Thus, further experimentation with dye flow through these devices and solute exchange by convection-diffusion will establish the design and fabrication of micro/nanofluidic devices by the method proposed in the paper for various applications.

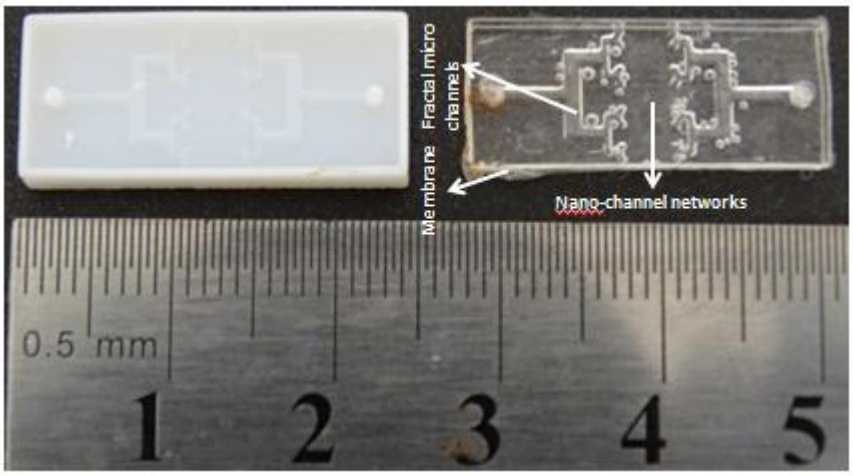

Figure 5 Image of PDMS device with fractal-shaped microchannels integrated with nanochannel network

4. Conclusions

The hybrid additive micromanufacturing techniques are capable of producing integrated micro-nano structures with wide span in their dimensional variability. Therefore, stand-alone technologies are currently being replaced by a combination of microtechnologies for complex applications. We have demonstrated the combination of additive micro/nanotechnologies to design and develop a biomimetic 3-D integrated micro-nanochannel network in PDMS device for solute exchange. We have used the 3-D printer and electrospinning, scalable technologies, to design and manufacture micro-mold having fractal-shaped features and nanoscale structures respectively in a device. Our unique way to combine the above scalable technologies with micro-molding and sacrificial etching lead to

the generation of 3-D integrated micro-nanochannel network in PDMS device, a good substitute for conventional lithography techniques. We are currently working towards the fluid flow and solute exchange through such devices. These PDMS devices are a natural mimic of vasculature system of living beings, where fractal-shaped microchannels enable efficient fluid flow whereas nanovascular network serves as the site for heat/mass transport operations. Thus, our study suggests a simple and scalable hybrid microtechnology fabricate fluidic devices having multiscale architecture. This will also facilitate the rapid fabrication of microfluidic devices for biomedical, self-healing/cooling materials, filtration, diagnostics, sensors, and micro-TAS applications.

Acknowledgements

Authors would like to acknowledge the IITB-Monash Academy for financial support. Authors would also like to thank SAIF (IIT Bombay) for SEM characterization and Materials Science and Engineering Department for use of 3-D printer

References

[1] S. C. Olugebefola, et al., Polymer Microvascular Network Composites. Journal of Composite Material, 2010. 44(22): p. 2587-2603.
[2] Duan C et al., Review article: Fabrication of nanofluidic devices Biomicrofluidics 2013 **7** p. 026- 50.
[3] M Vaezi et al., A review on 3D micro-additive manufacturing technologies, Int J Adv Manuf Technol (2013) 67:1721–1754
[4] F. P.W. Melchels et al., Additive manufacturing of tissues and organs, Progress in Polymer Science 37 (2012) 1079 – 1104
[5] C Mota et al., Additive manufacturing techniques for the production of tissue engineering constructs Journal of Tissue Engineering and Regenerative Medicine 2015; 9: 174–190
[6] Esser-Kahn, A.P., et al., Three-Dimensional Microvascular Fiber-Reinforced Composites. Advanced Materials, 2011. 23(32): p. 3654- 3658.
[7] Huang, J.H., et al., Rapid Fabrication of Bio-inspired 3D Microfluidic Vascular Networks. Advanced Materials, 2009. 21(35): p. 3567-3571.
[8] Therriault, D., et al., Fugitive Inks for Direct- Write Assembly of Three-Dimensional Microvascular Networks. Advanced Materials, 2005. 17(4): p.395-399
[9] C Mota et al., Multiscale fabrication of biomimetic scaffolds for tympanic membrane tissue engineering, Biofabrication, 2015 7 025005
[10] C. M. Rogers et al., A novel technique for the production of electrospun scaffolds with tailor three- dimensional micro-patterns employing additive manufacturing, Biofabrication**6** (2014) 035003 (11pp)
[11] Rizvi M S et al., 2012 Mathematical model of mechanical behavior of micro/nanofibrous materials designed for extracellular matrix substitutes *Acta Biomaterialia* (2012) **8** 4111-22

Appendix B

Study of diffusion of ammonia through PDMS membrane

1. Fabrication and characterization of polydimethylsiloxane (PDMS) membrane

The PDMS base and curing agent (10:1 ratio) was taken in a glass beaker and thoroughly mixed for 10 minutes with a glass rod until a milky broth like a mixture is obtained. Thereafter, degassing was carried out in a vacuum chamber. When no air bubble was observed in PDMS and clear transparent PDMS appeared, the degassing was terminated. Then a few drops of the PDMS was poured on a substrate (square shaped glass slide) kept on a chuck of spin coater as shown in figure 1. The spin coating was done at varying speed to generate different thickness of a film of PDMS. The experiments were carried out at speed ranging from 900 rpm to 5000 rpm to obtain a different thickness of PDMS membrane. The thin films so obtained were cured at 60^0C for 20 minutes on a hot plate. The samples were prepared and the thicknesses of the films were characterized by white light interferometry and screw gauge.

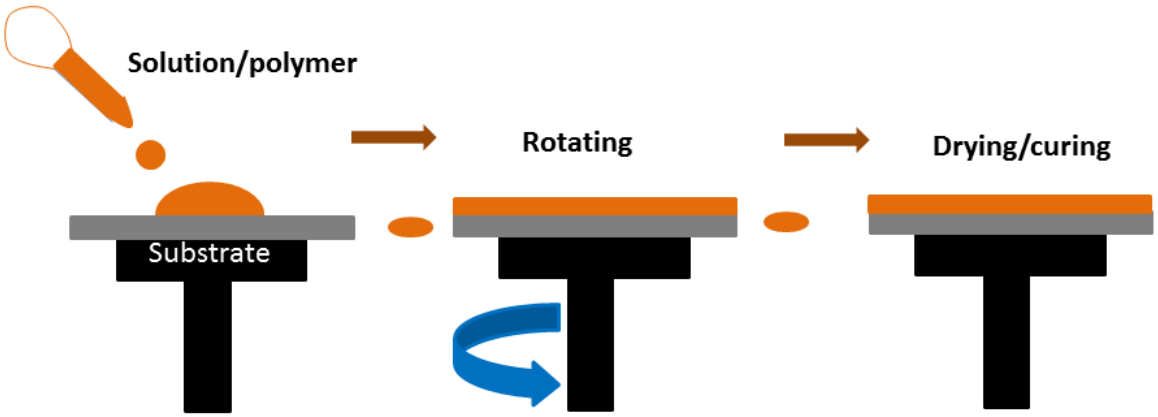

Figure 1 Spin coating of PDMS on glass substrate to form thin membranes

It was observed that the thickness of film remains nearly unaffected after the speed of 4000 rpm. The results of the thickness measured by white light interferometry corroborate well with the measurement carried out by screw gauge. These thin films were further removed from glass slide for further application. The graph in figure 2 shows the variation of thickness with varying speed of chuck of the spin coater.

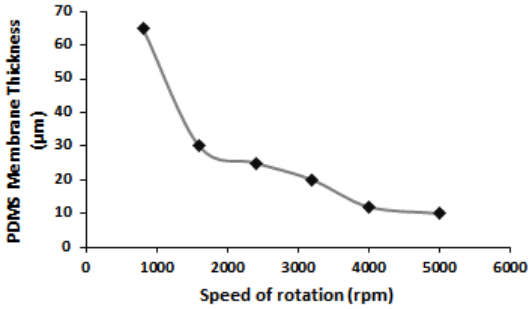

Figure 2 graph showing the variation of PDMS membrane thickness due speed of rotation of spin coater.

2. Design and fabrication of set-up for study of ammonia diffusion in PDMS membranes

2.1. Design and fabrication of samples of PDMS membranes:

The films produced by a spin coating were taken for diffusion study. A hollow metallic cylinder (stainless steel) having small rim thickness and diameter to be 1-1.5cm was taken and placed on the glass slide on which thin film was fabricated. Thereafter some weight was applied on the metallic cylinder before pouring the PDMS solution surrounding the cylinder up to an appreciable thickness. Then the entire setup was heated over a hot plate at 60^0C for 20 minutes for curing the surrounding PDMS. Then a thick PDMS block surrounding the metallic cylinder and thin membrane region inside the metallic cylinder was obtained. The system was carefully peeled off to get membrane of desired thickness surrounded by thick PDMS block as shown in figure 3. Thus PDMS membrane of any cross section area can be obtained by using suitable hollow metallic cylinder which needs to have further experimented. These membranes were further used for diffusion experiments.

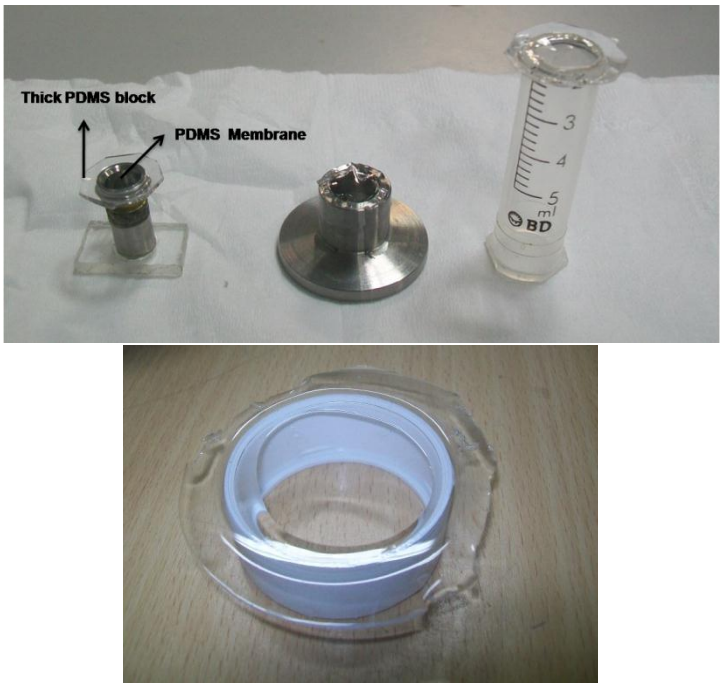

Figure 3 PDMS membrane on different hollow cylinders having different area

2.2 Experimental setup and study of ammonia diffusion through PDMS membranes:

The experimental setup was designed as shown in the figure (4A) for measuring diffusivity of ammonia in PDMS membrane. The PH meter probe was kept inside a cylinder with one end capped with 270µm thick membrane of PDMS. Then 3ml of DI water was added to the chamber containing PH probe. The PH probe was 2mm above the PDMS membrane. Then entire assembly was dipped in ammonia solution of 10 ml in a beaker as shown in figure (4B).

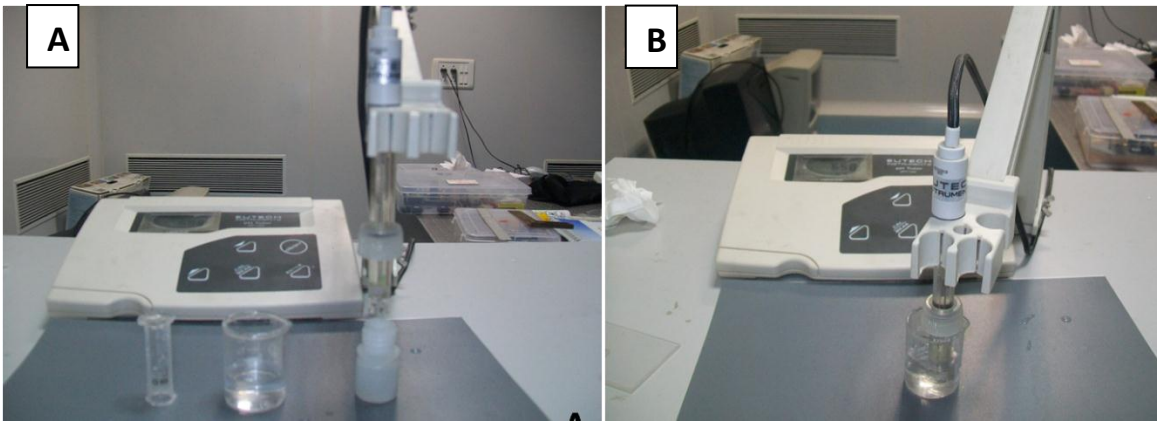

Figure 4 A) The setup for measuring the diffusion coefficient of ammonia in PDMS membrane B) The process of measuring ammonia diffusion

The pH was recorded as soon as the assembly was dipped in ammonia solution. Thereafter, pH was recorded at a regular interval of time. It was observed that there was no increase in pH of DI water for initial few minutes. Then there was an increase in pH of the solution with

an increase in time. The slope of concentration vs. time graph increased in the beginning and then becomes constant; indicating the steady state condition and then started decreasing with time. Initially, the ammonia from the ammonia solution may have diffused inside the PDMS membrane and then, it diffuses from the PDMS membrane to DI water in which pH probe was placed. The diffusion of ammonia continues in PDMS membrane as long as saturation of ammonia in PDMS membrane hasn't reached to equilibrium, marked by no increase in pH of the DI water. Once the saturation point has been reached, the ammonia diffuses from the membrane to DI water having a pH probe. Thereafter, pH readings were recorded. The distance between pH probe and membrane is 2mm and diffusivity constant of ammonia being higher in water than solid PDMS, it was confirmed that ammonia concentration measured on DI water side indicate the concentration of ammonia which has diffused through the membrane. Thus, the graph obtained from the concentration and time data was used to estimate the diffusivity constant of ammonia in PDMS membrane by the time lag method [1]. In this method, the amount of diffusant which passes through the membrane is given by equation

$$\frac{Q_t}{lC_1} = \frac{Dt}{l^2} - \frac{1}{6} - \frac{2}{\pi^2}\sum_{1}^{\infty}\frac{(-1)^n}{n^2} exp\left(\frac{-Dn^2\pi^2 t}{l^2}\right)$$

Where Q_t is the amount of diffusant which passes through the membrane in time t across the membrane of thickness l unit. if the steady state is assumed at t $\rightarrow \infty$, the above equation can be rewritten by discarding the exponential term as

$$Q_t = \frac{DC_1}{l}\left(t - \frac{l^2}{6D}\right)$$

The graph is plotted between the amounts of diffusant and time as shown in figure 5. The intercept on the time axis will be equal to $L^2/6D$. From this relation, D the diffusion coefficient of ammonia in PDMS can be determined from the linear portion of the graph after the lag period.

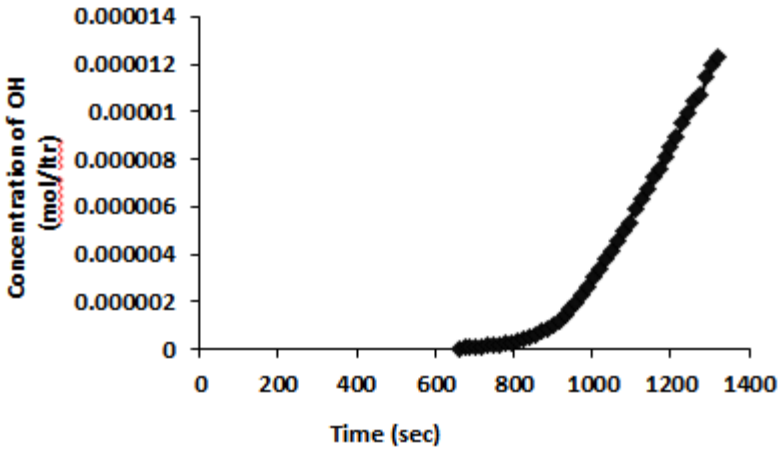

Figure 5 The graph showing the change in OH concentration in DI water with time

3. Solubility and Diffusivity Characterization of PDMS

3.1. Solubility test of ammonia in PDMS

To determine the solubility coefficient of the ammonia (NH_3) gas in PDMS solid block, a gravimetric method was employed. The small pieces of PDMS were taken and their individual weight on the weighing balance was measured. Then these PDMS pieces were dipped in glass vials having ammonium hydroxide solution for a certain fixed period of time. Then after a regular interval of time, PDMS pieces were taken out and its weight was measured again. The difference in weight suggested the weight of ammonia absorbed in the PDMS block. The weight of the ammonia absorbed was converted into a number of moles of ammonia. At Standard Temperature Pressure, using the ideal gas equation PV = nRT, the volume of the gas absorbed was estimated and expressed as the volume (ml) of gas absorbed per gram of PDMS. After the dipping the PDMS in ammonia, neither swelling of PDMS solid pieces nor change in the solid nature of PDMS was observed. Figure 6 shows the absorption curve of ammonia in PDMS solid. During measuring the weight of PDMS block with ammonia absorbed, the weight of the block was continuously decreasing. This is due to diffusion of ammonia from the block to the outer atmosphere of the weighing balance chamber.

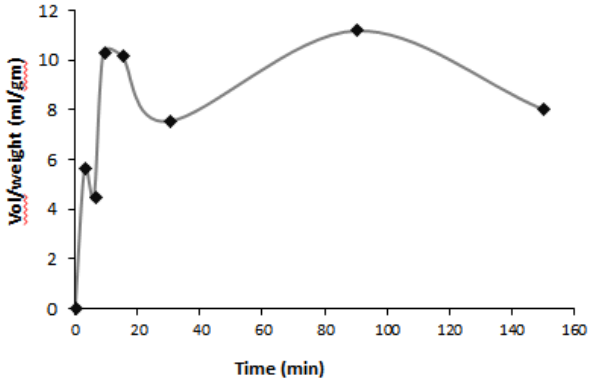

Figure 6 Volume of ammonia absorbed at STP per gram of PDMS in given time in minutes

3.2. Diffusivity of ammonia in PDMS by gravimetric method

The PDMS solid blocks were prepared by the above-described method. Then samples with certain size were excised with thickness (2.34mm). These samples were weighed using the weighing balance having the least count of 0.01mg. The weights of the samples were recorded. Thereafter samples were dipped in concentrated ammonia solution and left for more than 1 hour. After an hour, the samples were taken out of the solution and reweighed on the weighing balance. The weight of the sample was recorded after a certain interval of time. The experiments were repeated on two samples and data was recorded. It was observed that the weight of PDMS sample was continuously decreasing with time. The rate of decrease of weight of PDMS sample was higher in the beginning which slowed down with the passage of time. Later on the weight of sample became nearly constant. When the sample was weighed just after its transfer from ammonia solution to weighing balance chamber, they showed the highest weight. As the amount of ammonia in weighing balance chamber was negligible as compared to the amount of ammonia absorbed in PDMS, so ammonia diffusion from bulk PDMS solid to nearby surrounding was higher. Initially, the gradient of ammonia concentration was high between the bulk and surrounding, so there was rapid diffusion of ammonia from PDMS to surrounding air, marked by a rapid decrease in weight of PDMS. Then with the passage of time, the concentration gradient decreased which was observed by a very slow decrease in mass of PDMS block. Thereafter the system reached the point where the mass of ammonia in the PDMS block was nearly constant. The graph plotted between the decrease in mass of PDMS block and time, it shows an exponential decay of mass as seen in the figure 7A.

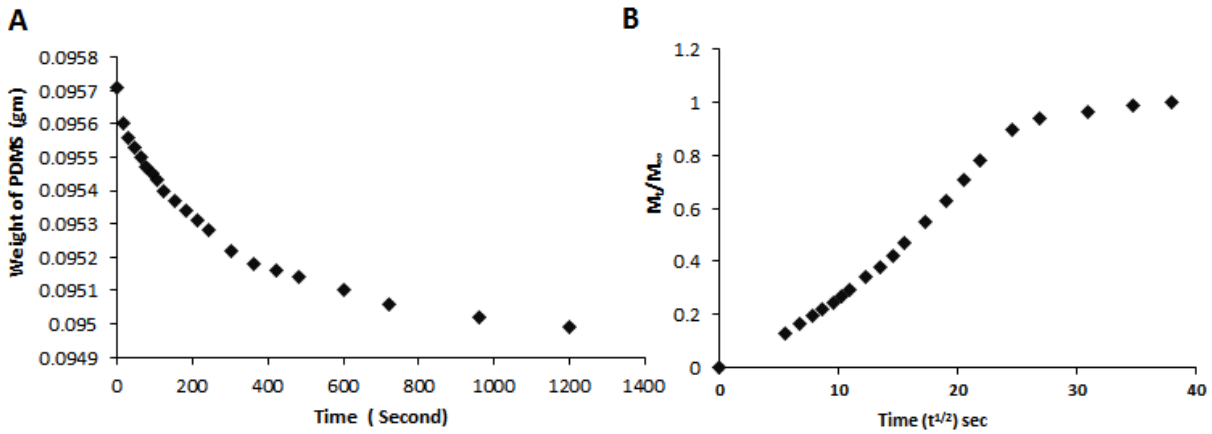

Figure 6 A) The desorption of ammonia from PDMS block with time B) The graph showing the relative decrease in mass of sample with square root of time

The graph shows the rate of gas desorption kinetics in a rubbery polymer like PDMS which can be used to estimate the diffusion coefficient of gas in the polymer. The sorption and desorption kinetics can also be used to study the relative mobility rate of penetrant and polymer chain. The Fickian sorption occurs when the relative rate of mobility of polymer chain is higher than the penetrant molecule, the rate of diffusion of the molecule is proportional to square root of the time. Crank in his seminal work proposed a Fickian diffusion model of desorption kinetics for predicting the diffusion coefficient of the penetrant which is independent of penetrant concentration by correlating mass of diffusant (m), time (t) and thickness of block (l). The empirical equation enables us to calculate the diffusion coefficient of ammonia in PDMS block.

$$\frac{M_t}{M_\infty} = t^{1/2}\left(\frac{16D}{\pi l^2}\right)^{1/2}$$

Where Mt is the amount of ammonia lost by the PDMS block at the time t and M_∞ is the final amount of ammonia lost from PDMS until equilibrium is reached. The diffusion coefficient can be graphically determined by the initial gradient of the graph between Mt/M∞ and $t^{1/2}$. The graph is shown in the figure 7B shows how the desorption of ammonia from PDMS block reaches equilibrium.

The curve demonstrates the way equilibrium is created during desorption of ammonia from PDMS block. The initial linear portion of the figure 7B was used to estimate the slope of the curve. The slope of the line from the figure 7B is equal to the $(16D/3.142\ L^2)^{1/2}$. Thus from the aforementioned relation diffusion coefficient of the ammonia in PDMS block is calculated. The experimented was repeated for 3 times and the diffusion coefficient of ammonia in PDMS blocks comes around 1.346e-9 m^2/sec.

Table 1 The diffusion coefficient of ammonia in PDMS calculated by two different methods and compared with literature

	Time Lag Method		Gravimetric Method		
S. No	Thickness of PDMS Membrane (µm)	Diffusivity coefficient (m^2/sec)	Thickness of PDMS block (mm)	Diffusivity coefficient (m^2/sec)	Diffusivity coefficient (m^2/sec)(Reported in literature[2])
1	50	0.0624e-10	2.34	15.5e-10	2.1e-10
2	100	0.0952e-10	2.34	11.7e-10	
3	270	0.135e-10	2.34	13.2e-10	

It can be observed that diffusivity of ammonia calculated by time lag method and gravimetric method differs from one reported in the literature. However, the values lie in the similar order of magnitude. Therefore, with the use of much sensitive Ph meter and weighing balance, it is possible to determine the diffusivity of ammonia in PDMS.

4. Study the factors affecting the diffusion in PDMS membranes

Further, the flux of ammonia is dependent on the thickness of PDMS membrane as shown in figure 8. It can be observed that ammonia flux increases with the decrease in thickness of PDMS membrane. The flux of ammonia follows an exponential decay with the thickness of the membrane. Therefore, the microfluidic devices using PDMS membrane for gas/solute separation should have thinnest membrane possible to maximize its separation efficiency.

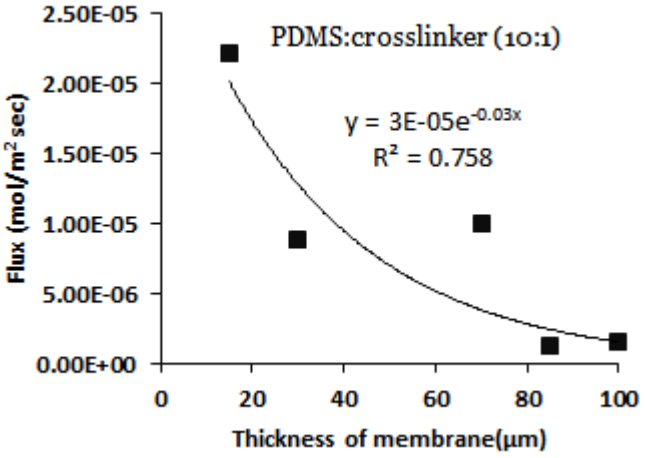

Figure 8 Flux of ammonia vs. the thickness of PDMS membrane

References:

[1] Nicolas Morliere, J.P.C., Eric Favre, Denis Roizard, *Characterization of film transport properties for organic vapors using time lag method- interest and limitation*, Desalination, 2002. 144: p. 109-113

[2] Petr Levinský, Ladislav Kalvoda, Jan Aubrecht, Jaroslava Fojtíková, *Diffusion of ammonia gas in PDMS characterized by ATR spectroscopy* Photonics, Devices, and Systems VI,Proc. of SPIE, 2015, Vol. 9450, 94500D

Appendix C

Estimation of randomness in electrospun fiber meshes

The SEM of electrospun fibrous meshes was processed by an image processing algorithm written in MATLAB®7.4. The Fast Fourier Transform analysis of images was carried out for samples with random and aligned fiber meshes in SEM images. The figure 1 (A & B) shows the SEM image of random and aligned fiber meshes while the figure1 (C & D) are representing their corresponding FFT images.

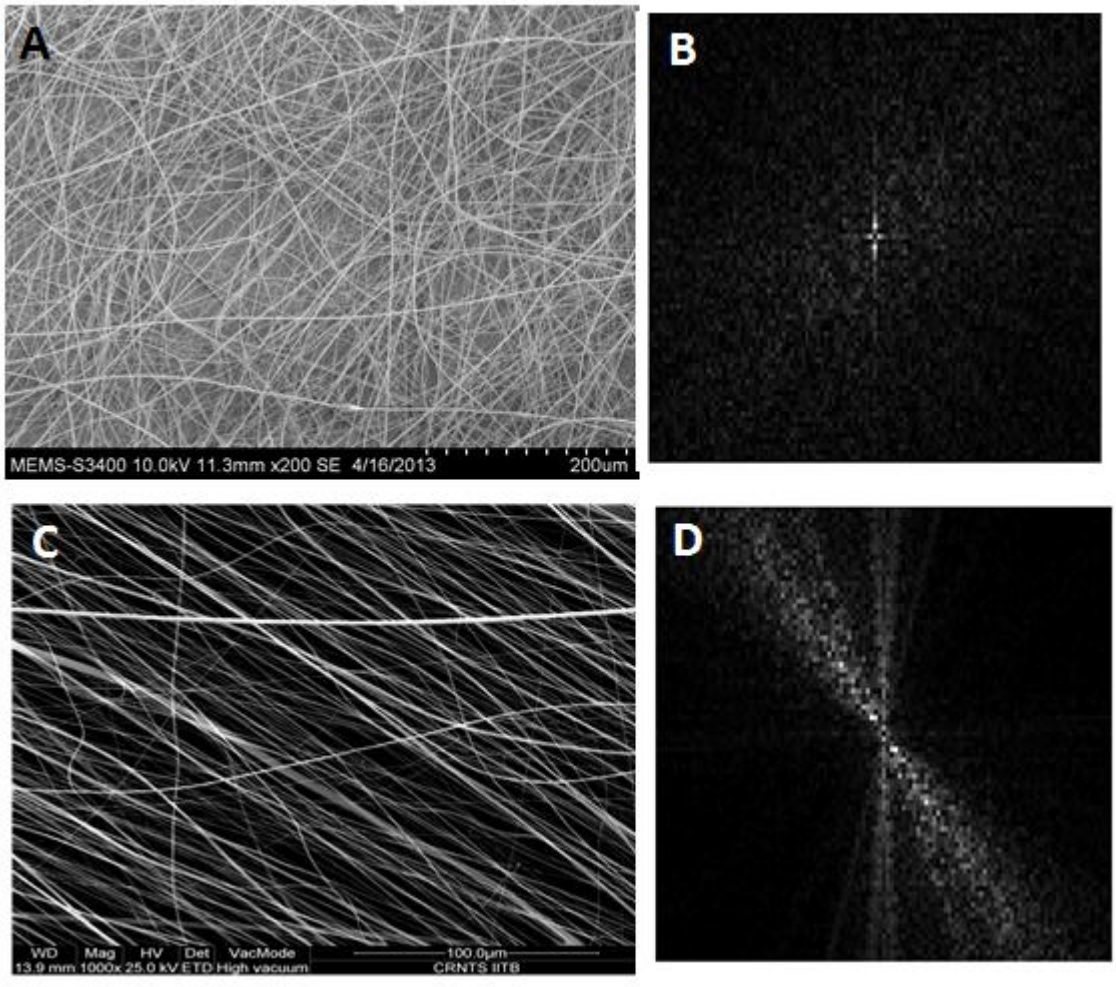

Figure 1 SEM images of Random Fiber meshes B) FFT image of the random fiber mesh C) SEM image of the aligned fiber meshes D) FFT image of the aligned fiber meshes.

Thereafter, as Fourier image being symmetrical about the center, we have plotted a graph between Fourier coefficients and radial angular span from 0 to 180^{o}. The alignment parameter (angle of spread) is given as angular span in which 50 % of Fourier coefficients laid.

Further, the fourth central moment of statistics is kurtosis and is given by the formula

$$k = \frac{\frac{1}{N}\sum x_i^4}{\left(\frac{1}{N}\sum x_i^2\right)^2} - 3$$

The completely random distribution represented by normal distribution has the kurtosis value equal to 0. Therefore, larger the deviation from 0, lesser is the degree of randomness and vice versa. The kurtosis value calculated from above SEM images was 0.803 and 1.791 for random and aligned fiber meshes respectively. These values can be used to quantify the degree of randomness in a fiber meshes.

References

1. Richardson, J.F., *Separation processes.* Gas Separation & Purification, 1990. **4**(1): p. 2-7.
2. Bruschke, H., *Industrial application of membrane separation processes.* Pure &App/. Chem, 1995. **67**(6): p. 993-1002.
3. Drioli, E. and M. Romano, *Progress and New Perspectives on Integrated Membrane Operations for Sustainable Industrial Growth.* Industrial & Engineering Chemistry Research, 2001. **40**(5): p. 1277-1300.
4. Shirke, A.S.R.A., *Recent developments in membranebased separations in biotechnology processes: review.* Preparative Biochemistry and Biotechnology, 2011. **41**(4): p. 398-421.
5. Chen, X. and J. Shen, *Review of membranes in microfluidics.* Journal of Chemical Technology & Biotechnology, 2016: p. n/a-n/a.
6. de Jong, J., R.G.H. Lammertink, and M. Wessling, *Membranes and microfluidics: a review.* Lab on a Chip, 2006. **6**(9): p. 1125-1139.
7. Davies, S.J., *Peritoneal dialysis - current status and future challenges.* Nat Rev Nephrol, 2013. **9**(7): p. 399-408.
8. Mosier, J.M., et al., *Extracorporeal membrane oxygenation (ECMO) for critically ill adults in the emergency department: history, current applications, and future directions.* Critical Care, 2015. **19**(1): p. 431.
9. [cited 2016 10th Nov]; Available from: www.worldkidneyday.org/faqs/chronic-kidney-disease/.
10. Bloom, D.E., Cafiero, E.T., Jané-Llopis, E., Abrahams-Gessel, S., Bloom, L.R., Fathima, S., Feigl, A.B., Gaziano, T., Mowafi, M., Pandya, A., Prettner, K., Rosenberg, L., Seligman, B., Stein, A.Z., & Weinstein, C, *The Global Economic Burden of Non-communicable Diseases*. 2011, The World Economic Forum and the Harvard School of Public Health: Geneva.
11. [cited 2016 18 Nov]; Available from: https://www.kidney.org/news/newsroom/factsheets/FastFacts.
12. Siegel RL, M.K., Jemal A., *Cancer Statistics, 2016.* A Cancer Journal for Clinicians, 2016. **66**: p. 7-30.
13. Potkay, J.A., *The promise of microfluidic artificial lungs.* Lab on a Chip, 2014. **14**(21): p. 4122-4138.
14. Potkay, J.A., et al., *Bio-inspired, efficient, artificial lung employing air as the ventilating gas.* Lab on a Chip, 2011. **11**(17): p. 2901-2909.
15. Kniazeva, T., et al., *A microfluidic respiratory assist device with high gas permeance for artificial lung applications.* Biomedical Microdevices, 2011. **13**(2): p. 315-323.
16. Rochow, N., et al. *Integrated microfluidic oxygenator bundles for blood gas exchange in premature infants*. in *Micro Electro Mechanical Systems (MEMS), 2012 IEEE 25th International Conference on*. 2012.
17. Steven Kim, B.F., Rishi Kant, Benjamin Chui, Ken Goldman, Jaehyun Park, Willieford Moses, Charles Blaha, Zohora Iqbal, Clarence Chow, Nathan Wright,

William H. Fissell, Andrew Zydney, Shuvo Roy, *Diffusive Silicon Nanopore Membranes for Hemodialysis Applications.* PLoS ONE 2016. **11**(7): p. e0159526.
18. Johnson, D.G., et al., *Ultrathin Silicon Membranes for Wearable Dialysis.* Advances in Chronic Kidney Disease. **20**(6): p. 508-515.
19. Sébastien Clerc, B.R., *Microfluidic Applications in the Pharmaceutical, Life Sciences, In-Vitro Diagnostic, and Medical Device Markets*. 2015. p. 32-42.
20. Mukherjee, A., ed. *Biomimetics, Learning from Nature*. 2010, In-Tech: India.
21. Williams, H.R., et al., *Biomimetic reliability strategies for self-healing vascular networks in engineering materials.* Journal of The Royal Society Interface, 2008. **5**(24): p. 735.
22. Jianming Li, S.C.a.R.S., *Biomimetic Architectures for Tissue Engineering*, in *Biomimetics, Learning from Nature*, A. Mukherjee, Editor. 2010, InTech: India. p. 487-506.
23. Wu, W., et al., *Direct-write assembly of biomimetic microvascular networks for efficient fluid transport.* Soft Matter, 2010. **6**(4): p. 739-742.
24. Escher, W., B. Michel, and D. Poulikakos, *Efficiency of optimized bifurcating tree-like and parallel microchannel networks in the cooling of electronics.* International Journal of Heat and Mass Transfer, 2009. **52**(5–6): p. 1421-1430.
25. Janakiraman, V., K. Mathur, and H. Baskaran, *Optimal Planar Flow Network Designs for Tissue Engineered Constructs with Built-in Vasculature.* Annals of biomedical engineering, 2007. **35**(3): p. 337-347.
26. Nathan F Lepora, P.V.a.T.J.P., *The state of the art in biomimetics.* Bioinspiration & Biomimetics, 2013. **8**: p. 013001 (11pp).
27. Reebs, S.G. *Oxygen and fish behavior*. 2009 [cited 2016 2nd Nov]; Available from: www.howfishbehave.ca.
28. JJ Cech Jr., C.B., *Gas exchange: Respiration: An Introduction*, in *Encyclopedia-of-Fish-Physiology*. 2011. p. 791-795.
29. Evans, D.H., P.M. Piermarini, and K.P. Choe, *The Multifunctional Fish Gill: Dominant Site of Gas Exchange, Osmoregulation, Acid-Base Regulation, and Excretion of Nitrogenous Waste.* Physiological Reviews, 2004. **85**(1): p. 97.
30. Hughes, G.M. and M. Morgan, *THE STRUCTURE OF FISH GILLS IN RELATION TO THEIR RESPIRATORY FUNCTION.* Biological Reviews, 1973. **48**(3): p. 419-475.
31. Jane B. Reece, M.R.T., Eric J. Simon, Jean L. Dickey, Kelly A. Hogan, *Campbell Biology: Concepts & Connections*. Vol. 8. 2015: Pearson Education.
32. Hughes, G.M., *The Dimensions of Fish Gills in Relation to Their Function.* Journal of Experimental Biology, 1966. **45**(1): p. 177.
33. Wilson JM, L.P., *Fish gill morphology: inside out.* JOURNAL OF EXPERIMENTAL ZOOLOGY 2002. **293**(3): p. 192-213.
34. Hughes, G.M., *Measurement of gill area in fishes: practices and problems.* Journal of the Marine Biological Association of the United Kingdom, 1984. **64**(3): p. 637-655.
35. DE JAGER, S. and W.J. Dekkers, *Relations Between Gill Structure and Activity in Fish.* Netherlands Journal of Zoology, 1974. **25**(3): p. 276-308.
36. McElrone, A.J., Choat, B., Gambetta, G. A. & Brodersen, C. R., *Water Uptake and Transport in Vascular Plants.* Nature Education Knowledge, 2013. **4**(5).

37. Roth-Nebelsick, A., et al., *Evolution and Function of Leaf Venation Architecture: A Review.* Annals of Botany, 2001. **87**(5): p. 553-566.
38. Noblin, X., et al., *Optimal vein density in artificial and real leaves.* Proceedings of the National Academy of Sciences, 2008. **105**(27): p. 9140-9144.
39. Wheeler, T.D. and A.D. Stroock, *The transpiration of water at negative pressures in a synthetic tree.* Nature, 2008. **455**(7210): p. 208-212.
40. Nguyen, D.T., Y.T. Leho, and A.P. Esser-Kahn, *A three-dimensional microvascular gas exchange unit for carbon dioxide capture.* Lab on a Chip, 2012. **12**(7): p. 1246-1250.
41. Kim, S., et al., *Preliminary Diffusive Clearance of Silicon Nanopore Membranes in a Parallel Plate Configuration for Renal Replacement Therapy.* ASAIO Journal, 2016. **62**(2): p. 169-175.
42. Fissell WH, Z.A., Roy S. , *Diffusive Silicon Nanopore Membranes for Hemodialysis Applications.* PLoS One, 2016. **11**(7): p. e0159526.
43. Li, J.-m., et al., *A bio-inspired micropump based on stomatal transpiration in plants.* Lab on a Chip, 2011. **11**(16): p. 2785-2789.
44. Jingmin L, C.L., Zheng X, Kaiping Z, Xue K, Liding W *A Microfluidic Pump/Valve Inspired by Xylem Embolism and Transpiration in Plants.* PLoS ONE 2012. **7**(11): p. e50320.
45. Lamb M, K.G., Morgan ER, Shafer MW. , *A synthetic leaf: The biomimetic potential of graphene oxide.* , in *SPIE, Bioinspiration, Biomimetics, and Bioreplication.* 2015, The International Society for Optical Engineering.: San Diego, United States America.
46. Cas Smith, A.B., Erika Hanson,Chris Garvin, *TAPPING INTO NATURE: THE FUTURE OF ENERGY, INNOVATION, AND BUSINESS*. 2010.
47. Razali, A.R. and Y. Qin, *A Review on Micro-manufacturing, Micro-forming and their Key Issues.* Procedia Engineering, 2013. **53**: p. 665-672.
48. Abgrall, P. and N.T. Nguyen, *Nanofluidic Devices and Their Applications.* Analytical Chemistry, 2008. **80**(7): p. 2326-2341.
49. Biswas, A., et al., *Advances in top–down and bottom–up surface nanofabrication: Techniques, applications & future prospects.* Advances in Colloid and Interface Science, 2012. **170**(1–2): p. 2-27.
50. S. C. Terry, J.H.J., and J. B. Angell, *A gas chromatographic air analyzer fabricated on a silicon wafer.* IEEE Transactions on Electron Devices, 1979. **26**(12): p. 1880–1886.
51. McDonald, J.C., et al., *Fabrication of microfluidic systems in poly(dimethylsiloxane).* ELECTROPHORESIS, 2000. **21**(1): p. 27-40.
52. Abgrall, P. and A.M. Gué, *Lab-on-chip technologies: making a microfluidic network and coupling it into a complete microsystem—a review.* Journal of Micromechanics and Microengineering, 2007. **17**(5): p. R15.
53. LaFratta, C.N., L. Li, and J.T. Fourkas, *Soft-lithographic replication of 3D microstructures with closed loops.* Proceedings of the National Academy of Sciences, 2006. **103**(23): p. 8589-8594.
54. Xu, B.-Y., et al., *Large scale lithography-free nano channel array on polystyrene.* Lab on a Chip, 2010. **10**(21): p. 2894-2901.

55. Lai, K.L., M.H. Hon, and I.C. Leu, *Pattern formation on polymer resist by solvent-assisted nanoimprinting with PDMS mold as a solvent transport medium.* Journal of Micromechanics and Microengineering, 2011. **21**(7): p. 075013.
56. Zhang, M., et al., *A simple method for fabricating multi-layer PDMS structures for 3D microfluidic chips.* Lab on a Chip, 2010. **10**(9): p. 1199-1203.
57. Guo You, H., et al., *Microfluidic hydrogels for tissue engineering.* Biofabrication, 2011. **3**(1): p. 012001.
58. Lee, K.-S., et al., *Advances in 3D nano/microfabrication using two-photon initiated polymerization.* Progress in Polymer Science, 2008. **33**(6): p. 631-681.
59. Zhang, X., X.N. Jiang, and C. Sun, *Micro-stereolithography of polymeric and ceramic microstructures.* Sensors and Actuators A: Physical, 1999. **77**(2): p. 149-156.
60. Hamsapriya, S., T. Bo, and K. Venkatakrishnan, *Maskless direct micro-structuring of PDMS by femtosecond laser localized rapid curing.* Journal of Micromechanics and Microengineering, 2011. **21**(7): p. 075018.
61. Xu, S. and Y. Zhao, *Monolithic fabrication of nanochannels using core–sheath nanofibers as sacrificial mold.* Microfluidics and Nanofluidics, 2011. **11**(3): p. 359-365.
62. Bellan, L.M., E.A. Strychalski, and H.G. Craighead, *Nanochannels fabricated in polydimethylsiloxane using sacrificial electrospun polyethylene oxide nanofibers.* Journal of Vacuum Science & Technology B, 2008. **26**(5): p. 1728-1731.
63. Lamberti, A., S.L. Marasso, and M. Cocuzza, *PDMS membranes with tunable gas permeability for microfluidic applications.* RSC Advances, 2014. **4**(106): p. 61415-61419.
64. K. C. Khulbe, C.Y.F., Takeshi Matsuura, *Synthetic Membranes for Membrane Processes*, in *Synthetic Polymeric Membranes*. 2008, Springer Berlin Heidelberg. p. 5-18.
65. Bell, C.M., F.J. Gerner, and H. Strathmann, *Selection of polymers for pervaporation membranes.* Journal of Membrane Science, 1988. **36**: p. 315-329.
66. Nijhuis, H.H., M.H.V. Mulder, and C.A. Smolders, *Removal of trace organics from aqueous solutions. Effect of membrane thickness.* Journal of Membrane Science, 1991. **61**: p. 99-111.
67. Bhattacharya, S. and S.-T. Hwang, *Concentration polarization, separation factor, and Peclet number in membrane processes.* Journal of Membrane Science, 1997. **132**(1): p. 73-90.
68. Agrahari, G.K., et al., *Model prediction and experimental studies on the removal of dissolved NH3 from water applying hollow fiber membrane contactor.* Journal of Membrane Science, 2012. **390–391**: p. 164-174.
69. Kjeang, E., N. Djilali, and D. Sinton, *Microfluidic fuel cells: A review.* Journal of Power Sources, 2009. **186**(2): p. 353-369.
70. Andersson, H. and A.v.d. Berg, *Microfabrication and microfluidics for tissue engineering: state of the art and future opportunities.* Lab on a Chip, 2004. **4**(2): p. 98-103.
71. Stamatialis, D.F., et al., *Medical applications of membranes: Drug delivery, artificial organs and tissue engineering.* Journal of Membrane Science, 2008. **308**(1–2): p. 1-34.

72. Moorthy, J. and D.J. Beebe, *In situ fabricated porous filters for microsystems.* Lab on a Chip, 2003. **3**(2): p. 62-66.
73. Hisamoto H, S.Y., Uchiyama K, Tokeshi M, Kikutani Y, Hibara A, Kitamori T., *Chemicofunctional membrane for integrated chemical processes on a microchip.* Analytical Chemistry, 2003. **75(**2): p. 350-4.
74. Jeje, A.A., *Rates of spontaneous movement of water in capillary tubes.* Journal of Colloid and Interface Science, 1979. **69**(3): p. 420-429.
75. Bellan, L.M., et al., *Fabrication of an artificial 3-dimensional vascular network using sacrificial sugar structures.* Soft Matter, 2009. **5**(7): p. 1354-1357.
76. Esser-Kahn, A.P., et al., *Three-Dimensional Microvascular Fiber-Reinforced Composites.* Advanced Materials, 2011. **23**(32): p. 3654-3658.
77. Li, J.-L. and B.-H. Chen, *Review of CO2 absorption using chemical solvents in hollow fiber membrane contactors.* Separation and Purification Technology, 2005. **41**(2): p. 109-122.
78. Gabelman, A. and S.-T. Hwang, *Hollow fiber membrane contactors.* Journal of Membrane Science, 1999. **159(**1–2): p. 61-106.
79. Randall, D.J., *7 Gas Exchange in Fish*, in *Fish Physiology*, W.S. Hoar and D.J. Randall, Editors. 1970, Academic Press. p. 253-292.
80. Wilson, J.M. and P. Laurent, *Fish gill morphology: inside out.* JOURNAL OF EXPERIMENTAL ZOOLOGY, 2002. **293**(3): p. 192-213.
81. Hughes, G.M., *Morphometrics of fish gills.* Respiration Physiology, 1972. **14(**1): p. 1-25.
82. HUGHES, G.M., *The dimensions of fish gills in relation to their function.* Experimental Biology, 1966. **45**: p. 177-195.
83. HUGHES, G.M., *Morphometrics of fish gills.* Respiration Physiology, 1972. **14**: p. 1-25.
84. G. M. HUGHES, M.M., *The structure of fish gills in relation to their respiratory function.* Biological Reviews, 1973. **48(**3): p. 419-475.
85. JOHANNES PIIPER, P.S., *Gas transport efficacy of gills, lungs and skin: theory and experimental data.* Respiration Physiology, 1975. **23**: p. 209-221.
86. JOHANNES PIIPER, P.S., *Maximum gas transfer efficacy of models for fish gills, avian lungs and mammalian lungs.* Respiration Physiology, 1972. **14**: p. 115-124.
87. Park, K., W. Kim, and H.-Y. Kim, *Optimal lamellar arrangement in fish gills.* Proceedings of the National Academy of Sciences, 2014. **111**(22): p. 8067-8070.
88. Dawson, T.H., *Modeling of vascular networks.* Journal of Experimental Biology, 2004. **208**: p. 1687-1694.
89. Truslow, J.G. and J. Tien, *Perfusion systems that minimize vascular volume fraction in engineered tissues.* Biomicrofluidics, 2011. **5**(2): p. 022201.
90. Goldstick, T.K., V.T. Ciuryla, and L. Zuckerman, *Diffusion of Oxygen in Plasma and Blood*, in *Oxygen Transport to Tissue — II*, J. Grote, D. Reneau, and G. Thews, Editors. 1976, Springer US: Boston, MA. p. 183-190.
91. Golding, H.M., *Hierarchical structures and transport processes in "fish gill" systems.* Final Year Report, Monash University, 2010.
92. Sidebotham, D., et al., *Venovenous Extracorporeal Membrane Oxygenation in Adults: Practical Aspects of Circuits, Cannulae, and Procedures.* Journal of Cardiothoracic and Vascular Anesthesia, 2012. **26**(5): p. 893-909.

93. Lim, M.W., *The history of extracorporeal oxygenators.* Anaesthesia, 2006. **61**: p. 984-995.
94. Report, W.H.O.; Available from: www.worldlifeexpectancy.com/world-rankings-total-deaths
95. UCSF, *www.ucsf.edu/news/2014/05/114181/ucsf-adult-lung-transplant-program-ranked-highest-nationally-patient-survival*.
96. Bloom, D.E., Cafiero, E.T., Jané-Llopis, E., Abrahams-Gessel, S., Bloom, L.R., Fathima, S., Feigl, A.B., Gaziano, T., Mowafi, M., Pandya, A., Prettner, K., Rosenberg, L., Seligman, B., Stein, A.Z., & Weinstein, C., *The Global Economic Burden of Noncommunicable Diseases. Geneva: World Economic Forum.* 2011.
97. Lee, K.G., et al., *3D printed modules for integrated microfluidic devices.* RSC Advances, 2014. **4**(62): p. 32876-32880.
98. McKim, R.J.E.a.J.M., *A model for exchange of organic chemicals at fish gills: flow and diffusion limitations.* Aquatic Toxicology,, 1990. **18**: p. 175-198.
99. Leon M. Bellan, E.A.S., and Harold G. Craighead, *Nanochannels fabricated in polydimethylsiloxane using sacrificial electrospun polyethylene oxide nanofibers.* Journal of Vacuum Science & Technology B, 2008. **26**(5).
100. Gualandi, C., et al., *Nanovascularization of Polymer Matrix: Generation of Nanochannels and Nanotubes by Sacrificial Electrospun fibers.* Nano Letters, 2013. **13**(11): p. 5385-5390.
101. Bellan, L.M., et al., *A 3D interconnected microchannel network formed in gelatin by sacrificial shellac microfibers.* Advanced materials (Deerfield Beach, Fla.), 2012. **24**(38): p. 5187-5191.
102. Squires, T.M., R.J. Messinger, and S.R. Manalis, *Making it stick: convection, reaction and diffusion in surface-based biosensors.* Nat Biotech, 2008. **26**(4): p. 417-426.
103. Cai, J., et al., *Generalized Modeling of Spontaneous Imbibition Based on Hagen–Poiseuille Flow in Tortuous Capillaries with Variably Shaped Apertures.* Langmuir, 2014. **30**(18): p. 5142-5151.
104. Rizvi, M.S., et al., *Mathematical model of mechanical behavior of micro/nanofibrous materials designed for extracellular matrix substitutes.* Acta Biomaterialia, 2012. **8**(11): p. 4111-4122.
105. Ali Y. Alharbi, D.V.P., Rebecca N. Cullion *Fluid Flow Through Microscale Fractal-Like Branching Channel Networks*. in *1st International Conference on Microchannels and Minichannels*. 2003. Rochester, New York, USA: American Society of Mechancial Engineers.
106. Beachley, V. and X. Wen, *Effect of electrospinning parameters on the nanofiber diameter and length.* Materials science & engineering. C, Materials for biological applications, 2009. **29**(3): p. 663-668.
107. Frenot, A. and I.S. Chronakis, *Polymer nanofibers assembled by electrospinning.* Current Opinion in Colloid & Interface Science, 2003. **8**(1): p. 64-75.
108. Bhardwaj, N. and S.C. Kundu, *Electrospinning: A fascinating fiber fabrication technique.* Biotechnology Advances, 2010. **28**(3): p. 325-347.
109. Teo, W.E. and S. Ramakrishna, *A review on electrospinning design and nanofibre assemblies.* Nanotechnology, 2006. **17**(14): p. R89.

110. Ding, P.L.a.B., *Applications of Electrospun Fibers.* Recent Patents on Nanotechnology, 2008. **2**(3): p. 169 - 182.
111. Liu, Y., et al., *Electrospun Fiber Template for Replica Molding of Microtopographical Neural Growth Guidance.* Small, 2012. **8**(5): p. 676-681.
112. Mailly, D. and C. Vieu, *Lithography and Etching Processes,* in *Nanoscience: Nanotechnologies and Nanophysics*, C. Dupas, P. Houdy, and M. Lahmani, Editors. 2007, Springer Berlin Heidelberg: Berlin, Heidelberg. p. 3-40.
113. Krishnan, S., *On the Manufacture of Very Thin Elastomeric Films by Spin-Coating*, in *Department of Mechanical Engineering*. 2007, MASSACHUSETTS INSTITUTE OF TECHNOLOGY. p. 157.
114. Chae, S.-K., J.-H. Ryoo, and S.-H. Lee, *Thin and large free-standing PDMS membrane by using polystyrene Petri dish.* BioChip Journal, 2012. **6**(2): p. 184-190.
115. Zbigniew Filutowicz, K.L., Krzysztof Pieszynski, *Remarks on spectro-photometeric monitoring of urea in Dialysate.* Journal of Medical Informatics and Technologies, 2004. **8**.
116. Ayres, C., et al., *Modulation of anisotropy in electrospun tissue-engineering scaffolds: Analysis of fiber alignment by the fast Fourier transform.* Biomaterials, 2006. **27**(32): p. 5524-5534.
117. J. Sung, Y.B.K., M.H. Lee, *Transient phenomena of dynamic contact angle in micro capillary flow.* 15th International Symposium on Flow Visualization, 2012. **June 25-28, 2012**(Minsk, Belarus).
118. Hamblin, M.N., et al., *Capillary flow in sacrificially etched nanochannels.* Biomicrofluidics, 2011. **5**(2): p. 021103.
119. Paterson, L., *Radial fingering in a Hele Shaw cell.* Journal of Fluid Mechanics, 1981. **113**: p. 513-529.
120. Guo, W., J. Hansson, and W. van der Wijngaart, *Capillary Pumping Independent of Liquid Sample Viscosity.* Langmuir, 2016.
121. CAI Jian-Chao, Y.B.-M., MEI Mao-Fei, LUO Liang, *Capillary Rise in a Single Tortuous Capillary.* Chinese Physics Letters, 2010. **27**(5): p. 054701-4.
122. Reich, P.B., *Body size, geometry, longevity and metabolism: do plant leaves behave like animal bodies?* Trends in Ecology & Evolution, 2001. **16**(12): p. 674-680.
123. West, G.B., J.H. Brown, and B.J. Enquist, *The Fourth Dimension of Life: Fractal Geometry and Allometric Scaling of Organisms.* Science, 1999. **284**(5420): p. 1677.
124. Losa, G.A., Merlini, D., Nonnenmacher, T.F., Weibel, E.R., *Fractals in Biology and Medicine*. Vol. 4. 2005: Birkhäuser Basel.
125. Díaz Lantada, A., et al., *Fractals in tissue engineering: toward biomimetic cell-culture matrices, microsystems and microstructured implants.* Expert Review of Medical Devices, 2013. **10**(5): p. 629-648.
126. Liu, S., Y. Zhang, and P. Liu, *Heat transfer and pressure drop in fractal microchannel heat sink for cooling of electronic chips.* Heat and Mass Transfer, 2007. **44**(2): p. 221-227.
127. Calamas, D. and J. Baker, *Performance of a Biologically Inspired Heat Exchanger with Hierarchical Bifurcating Flow Passages.* Journal of Thermophysics and Heat Transfer, 2013. **27**(1): p. 80-90.
128. Pence, D., *The simplicity of fractal-like flow networks for effective heat and mass transport.* Experimental Thermal and Fluid Science, 2010. **34**(4): p. 474-486.

129. Emerson, R.W.B.a.D.R., *Biomimetic Design of Artificial Micro-vasculatures for Tissue Engineering.* Alternatives to laboratory animals, 2010. **38**(1): p. 67–79.
130. Hoganson, D.M., H.I. Pryor, and J.P. Vacanti, *Tissue Engineering and Organ Structure: A Vascularized Approach to Liver and Lung.* Pediatr Res, 2008. **63**(5): p. 520-526.
131. Nakano, T., et al., *Multiscale fabrication of a transparent circulation type blood vessel simulator.* Biomicrofluidics, 2010. **4**(4): p. 046505.
132. Isobe, G., et al., *Perfusable multi-scale channels fabricated by integration of nanoimprint lighography (NIL) and UV lithography (UVL).* Microelectronic Engineering, 2012. **98**: p. 58-63.
133. Bellan, L.M., et al., *A 3D Interconnected Microchannel Network Formed in Gelatin by Sacrificial Shellac Microfibers.* Advanced Materials, 2012. **24**(38): p. 5187-5191.
134. Hasan, A., et al., *Microfluidic techniques for development of 3D vascularized tissue.* Biomaterials, 2014. **35**(26): p. 7308-7325.
135. Huang, J.-H., et al., *Rapid Fabrication of Bio-inspired 3D Microfluidic Vascular Networks.* Advanced Materials, 2009. **21**(35): p. 3567-3571.
136. Wu, W., A. DeConinck, and J.A. Lewis, *Omnidirectional Printing of 3D Microvascular Networks.* Advanced Materials, 2011. **23**(24): p. H178-H183.
137. Gergely, R.C.R., et al., *Multidimensional Vascularized Polymers using Degradable Sacrificial Templates.* Advanced Functional Materials, 2015. **25**(7): p. 1043-1052.
138. Sinha, S., T. Dutta, and S. Tarafdar, *Adhesion and fingering in the lifting Hele-Shaw cell: Role of the substrate.* The European Physical Journal E, 2008. **25**(3): p. 267-275.
139. Kabiraj, S.K. and S. Tarafdar, *Finger velocities in the lifting Hele–Shaw cell.* Physica A: Statistical Mechanics and its Applications, 2003. **328**(3–4): p. 305-314.
140. Jarusuwannapoom, T., et al., *Effect of solvents on electro-spinnability of polystyrene solutions and morphological appearance of resulting electrospun polystyrene fibers.* European Polymer Journal, 2005. **41**(3): p. 409-421.
141. Kumar P, G.P.S., Majumder M *Interfacing 3D micro/nanochannels with branch-shaped reservoir enhances fluid and mass transport* Journal of Micromechanics and Microengineering, 2016. **(accepted)**.
142. Kumar, P., Gandhi, Prasanna S, Majumder, Mainak. *Design and fabrication of thin microvascularised polymer matrices inspired from secondary lamellae of fish gills*. in *Proc. SPIE Bioinspiration, Biomimetics, and Bioreplication*. 2016. Las Vegas, Nevada, USA: SPIE.
143. Zbigniew Filutowicz K L, K.P., *Remarks on spectro-photometeric monitoring of urea in Dialysate* Journal of Medical Informatics and Technologies 2004 **8**: p. 105-110.
144. Haussener, S. and A. Steinfeld, *Effective Heat and Mass Transport Properties of Anisotropic Porous Ceria for Solar Thermochemical Fuel Generation.* Materials, 2012. **5**(1): p. 192.
145. Toepke, M.W. and D.J. Beebe, *PDMS absorption of small molecules and consequences in microfluidic applications.* Lab on a Chip, 2006. **6**(12): p. 1484-1486.
146. Farideh Abhari , H.J.a.N.A.M.Y., *A Comprehensive Study of Micropumps Technologies.* International Journal of Electrochemical Science, 2012. **7**: p. 9765 - 9780.

147. Crawford, R., et al., *Experimental characterization of the effects of geometric parameters on evaporative pumping.* Experimental Thermal and Fluid Science, 2013. **51**: p. 183-188.
148. Lebon, J.B.a.G., *Capillary Ascension in Porous Media: A Scaling Law.* Transport in porous media, 1994. **16**: p. 253-261.
149. Zwieniecki, N.M.H.a.M.A., *Transporting water to the tops of trees.* Physics Today, 2008. **61**: p. 76-77.
150. McElrone, A.J., Choat, B., Gambetta, G. A. & Brodersen, C. R., *Water Uptake and Transport in Vascular Plants.* Nature Education Knowledge, 2013. **4**(5): p. 6.
151. Hayward, A.T.J., *Mechanical Pump with a Suction Lift of 17 Metres.* Nature, 1970. **225**(5230): p. 376-377.
152. Effenhauser, C.S., H. Harttig, and P. Krämer, *An Evaporation-Based Disposable Micropump Concept for Continuous Monitoring Applications.* Biomedical Microdevices, 2002. **4**(1): p. 27-32.
153. Goedecke, N., J. Eijkel, and A. Manz, *Evaporation driven pumping for chromatography application.* Lab on a Chip, 2002. **2**(4): p. 219-223.
154. Lamb M, K.G., Morgan ER, Shafer MW. *A synthetic leaf: The biomimetic potential of graphene oxide.* . in *SPIE, Bioinspiration, Biomimetics, and Bioreplication*. 2015. San Diego, United States, .
155. Jingmin, L., et al., *A Microfluidic Pump/Valve Inspired by Xylem Embolism and Transpiration in Plants.* PLoS ONE, 2012. **7**(11): p. e50320.
156. Tanveer ul Islam, P.S.G. *Spontaneous Fabrication of Three Dimensional Multi-Scale Fractal Structures Using Hele Shaw Cell*. in *ASME 2016 11th International Manufacturing Science and Engineering Conference*. 2016. Blacksburg, Virginia, USA.
157. Adake, C.V., P. Gandhi, and P. Bhargava, *Fabrication of Ceramic Component Using Constrained Surface Microstereolithography.* Procedia Materials Science, 2014. **5**: p. 355-361.
158. Saffman, P.G., *Viscous fingering in Hele-Shaw cells.* Journal of Fluid Mechanics, 1986. **173**: p. 73-94.
159. Loh, Q.L., and Cleo Choong, *Three-Dimensional Scaffolds for Tissue Engineering Applications: Role of Porosity and Pore Size.* Tissue Engineering Part B: Reviews., 2013. **19**(6): p. 485–502.
160. Payam Rahimi, C.A.W., *Kinetics of evaporation: Statistical rate theory approach.* International Journal of Thermodynamics, 2005. **8**(1): p. 1-14.
161. Shou, D., L. Ye, and J. Fan, *The fastest capillary flow under gravity.* Applied Physics Letters, 2014. **104**(23): p. 231602.
162. Piljek, P., Keran, Z., Math, M., *Micromachining – Review of Literature from 1980 to 2010.* . Interdisciplinary Description of Complex Systems : INDECS, 2010. **12**(1).
163. Engstrom, D.S., et al., *Additive nanomanufacturing – A review.* Journal of Materials Research, 2014. **29**(17): p. 1792-1816.
164. Pimpin, A. and W. Srituravanich, *Review on Micro- and Nanolithography Techniques and Their Applications.* Engineering Journal; Vol 16, No 1 (2012): Regular IssueDO - 10.4186/ej.2012.16.1.37, 2011.

List of publications and achievements

Conferences and Journal publication (published or under preparation)

- **Kumar P**, P S Gandhi, M Majumder, *Design and fabrication of thin microvascularised polymer matrices inspired from secondary lamellae of fish gills*," "Bioinspiration, Biomimetics, and Bioreplication VI", International conference, SPIE/NDE, (Las Vegas, USA), 9797-40, 2016 [Conference proceeding: ERA –'A']
- **Kumar P**, P S Gandhi, M Majumder, *Multiscale fabrication of scalable biomimetic 3-D, integrated micro-nanochannels network in PDMS for solute exchange*, 11th International Conference on Micromanufacturing, 2016 (UC Irvine, USA) [Conference proceeding]
- **Kumar P,** Gandhi P.S, Majumder M, *Interfacing 3D micro/-nanochannel networks with branch shaped reservoir enhances fluid flow and mass transfer*, Journal of Microengineering and Micromechanics (IOP) 2017, 27, 015026 (11pp)
- **Kumar P,** U L Tanveer, Majumder M, Gandhi P.S, *A scalable, lithography-less fabrication process to generate bio-inspired, multi-scale, channel network in polymers,* Biomedical Physics and Engineering Express (IOP), 3 (2017) 045007
- **Kumar P,** Gandhi P.S, Majumder M, *Fabrication of leaf-inspired micropump for pumping of fluid,* (Under preparation)

Patents

- **Kumar P**, Gandhi P.S, Majumder M, *Scalable fabrication of bio-inspired 3D micro/nanofluidic devices*, App. number –TEMP/E-1/15499/2017-MUM, India (filed)

Poster and oral presentations

- Presented a Poster on *Design and fabrication of thin microvascularised polymer matrices inspired from secondary lamellae of fish gills* in an International conference, SPIE Smart structures/NDE 2016, (Las Vegas, USA)
- Presented a Poster and Oral presentation on *Multiscale fabrication of scalable biomimetic 3-D, integrated micro-nanochannels network in PDMS for solute exchange* in an 11th International Conference on Micromanufacturing, 2016 (UC Irvine, USA)
- Presented a Poster on *Design and fabrication of thin PDMS matrices having bio-mimetic vascular channel network* at an International conference on Biomaterial, Biodiagnostics, Tissue Engineering, Drug Delivery and Regenerative medicine (BiTERM 2016), New Delhi, India
- Presented an Oral presentation on *Enhanced capillary pumping through Leaf-inspired micropumps in biomedical microdevices* in National conference on Convergence on Pharmaceutical Sciences and Biomedical Technologies, Ahmadabad, India, 2018

Others achievements

- Top 30 finalist for grant proposal on *artificial lung device* under Scheme for Young Scientists and Technologist 2016, DST, Govt of India

- Awarded best innovator award in NanoSparX competition in 8th International conference of Bangalore India Nano, 2016 for work on *leaf-inspired micropump*
- Selected for Technical Evaluation Presentation in BIG BIRAC, 2017 for the *biomimetic artificial kidney dialyzer* project
- Awarded 1st prize in the oral presentation in a national conference on Convergence on Pharmaceutical Sciences and Biomedical technologies, Ahmadabad, India, 2018